



## Politecnico di Torino

Master of Science Course in Materials Engineering  
A.Y. 2021/2022  
Graduation session March 2022

# Characterization methodology to assess the mechanical properties of delignified birch/PMMA transparent wood biocomposites

Supervisors:

Prof. Federico Carosio  
Dr. Marcus Vinícius Tavares da Costa

Candidate:

Nicolò Arcieri  
S277833



## **Abstract**

Transparent wood (TW) biocomposites are a new attractive class of materials. They are based on a delignified wood template impregnated by a refractive index-matching polymer. TWs can be tailored in order to show a wide range of functional, optical, and mechanical properties. Moreover, being biobased, they are seen as a possible key material to replace more environmentally impactful materials in various sectors including the construction industry. However, unlike the functional properties, the mechanical behaviour of this class of materials has been poorly investigated. Therefore, in this thesis, the aim was to extend the current knowledge about the mechanical response of these materials by using a two-step mechanical characterization on TW and native wood as reference material.

The analysed TW biocomposite was prepared by impregnation of delignified birch veneers by PMMA. The mechanical characterization was carried out using different techniques. The Young's modulus and the flexural strength along the transverse direction were studied by four-point bending tests. The results showed an improvement for both properties compared to native birch wood. The fracture perpendicular to the grain (TR system) was investigated by performing *in situ* single-edge-notched four-point bending tests onto a scanning electron microscope to observe how the cracks propagate in this complex microstructure. A remarkable improvement (about 275 percent) in fracture toughness was found compared to the native wood. Furthermore, the *in situ* single-edge-notched four-point bending test was also applied, together with the digital image correlation (DIC) technique, to study the strain field during the crack growth, specifically the formation of the fracture process zone (FPZ) around the crack tip. Then, an equation describing the cohesive law was proposed for both materials based on experimental observations that can be ultimately used for fracture mechanics simulations. Finally, it was briefly shown how to make use of the measured mechanical properties of the novel TW for material selection for engineering applications.

### **Keywords:**

Transparent wood, biocomposite, birch, mechanical properties, fracture toughness, *in situ* experiments, cohesive zone model

## Contents

<b>Summary .....</b>	i
<b>List of abbreviations.....</b>	xxvii
<b>1. Introduction .....</b>	1
<i>1.1 Background .....</i>	1
<i>1.2 Research Aims .....</i>	2
<i>1.3 Structure of the Thesis .....</i>	2
<b>2. Wood.....</b>	3
<i>2.1 Softwood and Hardwood .....</i>	3
<i>2.2 Cell structure.....</i>	5
<i>2.3 Betula Pendula .....</i>	5
<i>2.4 Mechanical properties of wood.....</i>	6
<i>2.4.1 Fracture toughness of wood .....</i>	6
<b>3. Transparent wood biocomposites .....</b>	9
<i>3.1 From native wood to transparent wood .....</i>	9
<i>3.2 Mechanical properties of transparent wood biocomposites .....</i>	11
<b>4. Materials and Methodology.....</b>	13
<i>4.1 Samples.....</i>	13
<i>4.1.1 Multilayer transparent wood synthesis.....</i>	13
<i>4.1.2 Sample preparation.....</i>	15
<i>4.2 Characterization.....</i>	16
<i>4.2.1 Wood cell wall volume fraction .....</i>	16
<i>4.2.2 Optical microscopy .....</i>	17
<i>4.2.3 Scanning electron microscopy .....</i>	17
<i>4.2.4 Four-point bending test .....</i>	17
<i>4.2.5 Single-edge-notched four-point bending test .....</i>	20
<i>4.2.6 Digital Image Correlation (DIC).....</i>	22
<i>4.2.7 Cohesive law measurements .....</i>	22
<i>4.2.8 Material selection .....</i>	22
<b>5. Results and Discussion .....</b>	25
<i>5.1 Elastic modulus and flexural strength along the weak direction .....</i>	25
<i>5.1.1. Fracture surfaces .....</i>	27
<i>5.2 Fracture toughness along the TR system .....</i>	28

5.2.1 In situ observations.....	30
5.2.2 Fracture surfaces .....	33
5.3 <i>DIC analysis</i> .....	35
5.4 <i>Cohesive law</i> .....	39
5.5 <i>Demonstration of use of the measured mechanical properties for material design</i> ....	43
<b>6. Conclusion and future works</b> .....	47
6.1 <i>Résumé</i> .....	47
6.2 <i>Future works</i> .....	47
<b>Acknowledgements</b> .....	48
<b>References</b> .....	49

## **Summary**

This section summarises the content of the dissertation in Italian as required by Politecnico di Torino in its guidelines.

## **Introduzione**

### *Background*

L'uomo ha utilizzato il legno come materiale da costruzione fin dai tempi più antichi [1], ma, a partire dal XIX secolo, lo ha progressivamente rimpiazzato con acciaio e calcestruzzo. Tuttavia, le sfide climatiche che il mondo affronta oggigiorno richiedono di ripensare l'intera società in un'ottica più rispettosa dell'ambiente e, per questo motivo, la domanda di materiali che possa coniugare contemporaneamente elevate prestazioni e sostenibilità cresce di giorno in giorno [2]. Nel settore edilizio, dove le proprietà meccaniche giocano un ruolo fondamentale, i biocompositi a base legno sono visti come una possibile alternativa ai materiali tradizionali. Tra questi materiali innovativi, spicca il legno trasparente (transparent wood or TW in inglese) che combina buone performance meccaniche e leggerezza [3]. Questo biocomposito si basa sull'impregnazione di un template di legno delignificato da parte di un polimero avente il medesimo indice di rifrazione [4,5]. La delignificazione è uno step importante del processo produttivo in quanto permette di rimuovere i gruppi cromofori del legno e di facilitare l'impregnazione tramite l'aumento di porosità [3,6]. Questo porta, come suggerisce il nome del materiale stesso, ad ottenere un'elevata trasmittanza ottica nel composito finale.

Inoltre, la delignificazione, aumentando l'accessibilità della parete cellulare del legno, facilita la funzionalizzazione del materiale [6], permettendo di modificare le proprietà finali del biocomposito e, eventualmente, di aggiungerne di nuove [7]. Per questo non stupisce lo sforzo della comunità scientifica nello studio e nella modifica delle proprietà funzionali del legno trasparente [3,4,6,7,9-12].

Lo stesso non si può dire per le proprietà meccaniche, dove poco è stato fatto e soprattutto limitatamente al modulo elastico e alla resistenza alla trazione [5,13-16] ma il crescente interesse intorno a questo materiale richiede che un ulteriore passo verso la completa caratterizzazione meccanica venga compiuto.

Per materiali utilizzati in applicazioni strutturali, la tenacità a frattura è una delle prime proprietà che viene investigata in quanto fornisce informazioni utili sul comportamento a frattura del materiale [17]. La caratterizzazione dei meccanismi di frattura nel legno trasparente è però ancora a una fase embrionale, con poche pubblicazioni che trattano questo aspetto [13,16]. Pertanto, questa grave mancanza deve essere colmata se si vuole incentivare la sua commercializzazione.

## *Scopi della Ricerca*

L’obiettivo di questa tesi è stato di conseguenza quello di caratterizzare alcune delle proprietà meccaniche del legno trasparente e, più in particolare, del legno trasparente d-betulla/PMMA multistrato, dove “d” sta per delignificato. La betulla (*Betulla Pendula*) è stata scelta come template in quanto garantisce una buona frazione in volume di rinforzo nel materiale finale. Anche il comportamento meccanico del legno di betulla è stato studiato per fornire, insieme ai dati ricavati in letteratura, un termine di confronto per le proprietà del legno trasparente.

Il lavoro sperimentale ha previsto l’utilizzo di prove meccaniche come la flessione a quattro punti tradizionale per valutare la rigidezza e la resistenza a flessione nella direzione trasversale. La flessione a quattro punti in situ su provini di tipo single-edge notched bending è stata invece impiegata per lo studio della tenacità a frattura lungo il sistema tangenziale radiale (TR). Infatti, proprio come si verifica nel legno nativo [1-21], la cricca ha otto possibili sistemi di propagazione nel legno trasparente. L’utilizzo di una tecnica in situ all’interno di un microscopio elettronico (SEM) ha permesso di studiare in tempo reale la rottura del materiale e i suoi meccanismi di frattura. Le informazioni ricavate durante le osservazioni in situ, combinate all’analisi tramite digital image correlation (DIC) delle immagini acquisite al SEM durante il test, ha permesso di fornire una prima modellizzazione della legge coesiva per il legno trasparente. Infine, i dati raccolti sono stati brevemente studiati tramite i diagrammi di Ashby.

In conclusione, il principale scopo di questa tesi è stato quello di studiare la risposta meccanica e i meccanismi che portano alla frattura del legno trasparente d-betulla/PMMA, fornendo allo stesso tempo informazioni per la modellazione del comportamento del materiale.

## *Struttura della tesi*

La tesi è organizzata in diversi capitoli. Il primo contiene informazioni sul background e sugli scopi della ricerca. Nel Capitolo 2 viene riportata una descrizione della struttura e delle proprietà del legno mentre nel Capitolo 3 viene fornita una panoramica sul legno trasparente. Il Capitolo 4 ha l’obiettivo di descrivere la produzione del biocomposito studiato e introdurre le tecniche utilizzate per la caratterizzazione dei materiali. Nel Capitolo 5 vengono riportati e discussi i risultati ottenuti durante il lavoro sperimentale. Per concludere, l’ultimo capitolo riassume ciò che è stato ottenuto e fornisce spunti per future ricerche.

## Il legno

Le strabilianti proprietà meccaniche che hanno fatto sì che il legno sia stato utilizzato come materiale da costruzione fin dall'antichità derivano dalla particolare organizzazione della sua struttura interna. Tale tipo di organizzazione strutturale è detto gerarchico, ed è molto comune negli esseri viventi, basti pensare alle ossa umane [23].

Macroscopicamente, il legno può essere catalogato come materiale cellulare. In questo caso, le cellule sono modellizzate come cilindri cavi. Tuttavia, analizzando la singola cellula, la struttura è più simile a quella di un composito rinforzato con fibre. La parete cellulare è, infatti, costituita da un insieme di microfibrille di cellulosa tenute insieme da una matrice di emicellulosa e lignina [24]. Tale complessità strutturale ha inevitabilmente delle ripercussioni sulle proprietà del legno e pertanto deve essere approfondita.

Il legname disponibile in commercio viene generalmente diviso in due grosse categorie: legno tenero e legno duro. Da un punto di vista più rigoroso, il termine “legno tenero” indica il legname prodotto da specie appartenenti alla famiglia delle gimnosperme mentre il “legno duro” è ottenuto da alberi appartenenti alla famiglia delle angiosperme. L'appartenenza a famiglie di piante differenti si riflette anche sulla microstruttura, con il legno tenero che presenta una complessità microstrutturale inferiore [28-29].

Nei legni teneri i principali tipi di cellula sono le tracheidi e il parenchima. Le tracheidi costituiscono la maggior parte del volume cellulare e svolgono sia l'azione di supporto meccanico della pianta sia quella di distribuzione dei fluidi all'interno della stessa. Le tracheidi cresciute in primavera presentano un diametro maggiore e una parete cellulare più sottile rispetto a quelle sviluppatesi durante l'estate [29].

Nelle angiosperme, la varietà di cellule aumenta in quanto esse sono più specializzate rispetto a quelle presenti nel legno tenero. In questo caso la funzione di trasporto dei liquidi è assolta dalle cellule note come vasi mentre le fibre provvedono al supporto meccanico. I vasi, spesso visibili ad occhio nudo, sono costituiti da una sottile parete cellulare mentre la parte centrale della cellula risulta vuota e con le estremità aperte, proprio come un tubo [29,31]. Un altro tipo di cellule che non può essere trascurato sono le cellule del parenchima radiale che si estendono lungo il piano radiale, perpendicolarmente alle fibre [1,30]. Un'ulteriore suddivisione basata sulla distribuzione dei vasi può essere fatta per il legno duro. In questo caso si identificano tre sottocategorie: legno con porosità ad anello, con porosità diffusa e infine, legno con porosità a semi-anello [29,31].

Nel legno, la struttura generale della cellula è costituita da una parte centrale cava, chiamata lume cellulare, e dalla parete cellulare [31], quest'ultima, può essere divisa in tre regioni chiamate: lamella mediana, parete primaria e parete secondaria [29,31,33]. I principali costituenti biologici della parete cellulare sono cellulosa, lignina ed emicellulosa [28,29,31,33]. La lamella mediana è il primo strato che si incontra procedendo dall'esterno verso il centro della cellula ed è anche il più ricco in lignina dell'intera parete cellulare. La parete primaria, che costituisce il successivo strato, è invece formata da microfibrille di cellulosa con orientazione casuale. Le pareti primarie di due cellule adiacenti e la lamella mediana compresa tra esse costituiscono il composto lamella mediana [29,31]. La parete secondaria può essere a sua volta divisa in tre distinti strati S1, S2 e S3. S2 costituisce la maggior parte della parete cellulare e da esso dipendono le proprietà del legno [29,31,33]. Anche S2 è costituito da microfibrille di cellulosa ma in questo caso esse sono fortemente

orientate. L'angolo formato dalle microfibrille con l'asse della cellula influenza enormemente le proprietà finali del legno. Infatti, angoli piccoli garantiscono migliori prestazioni meccaniche.

*Betulla Pendula*, volgarmente nota come betulla argentata, produce legno duro con porosità diffusa. Questo legname è usato soprattutto sottoforma di compensato in applicazioni strutturali [35,37].

La complessa microstruttura del legno rende la sua risposta meccanica anisotropa [1,28], ma nel caso il legno venga estratto sufficientemente lontano dal centro del tronco, le proprietà possono essere considerate ortotropiche. Quando si tratta di legno, i tre assi ortogonali seguono una diversa nomenclatura. L'asse parallelo alle fibre prende il nome di longitudinale (L), lungo questo asse sono registrate le migliori performances meccaniche. L'asse tangente agli anelli di crescita è l'asse tangenziale (T) mentre l'asse normale agli anelli è l'asse radiale (R). Sia l'asse tangenziale che quello radiale sono perpendicolari alle fibre.

Prima di parlare della tenacità a frattura del legno, occorre introdurre il concetto di meccanica della frattura. Le sollecitazioni che provocano la propagazione di una cricca possono essere ricondotte a tre modi di carico o a una loro combinazione [40]. Nel Modo I la frattura avviene per apertura, nel Modo II per scorrimento mentre nel Modo III per lacerazione [40,41]. Ad ogni modalità di sollecitazioni è associato un parametro chiamato fattore di intensità degli sforzi ( $K$ ), diverso per ciascun modo.  $K$  è una misura dello sforzo intorno all'apice della cricca e viene usato per predire il comportamento del materiale durante la propagazione del difetto. Il valore che  $K$  assume subito prima dell'inizio della crescita della cricca è definito come fattore di intensità degli sforzi critico ( $K_c$ ) o tenacità alla frattura ed è riconosciuto come proprietà del materiale.

Lo studio della frattura del legno non è nuovo date le sue implicazioni in ambito industriale [44]. Ashby e i suoi coautori [21] hanno individuato otto diversi sistemi, riportati in Figura 1, lungo la quale un difetto può propagarsi nel legno. Ciascun sistema di propagazione viene identificato da due lettere, la prima indica la direzione normale al piano di propagazione mentre la seconda la direzione lungo la quale la cricca si propaga. Nei sistemi LT e LR la cricca propaga perpendicolare alle fibre mentre nei restanti sistemi cresce parallela all'orientazione delle fibre.

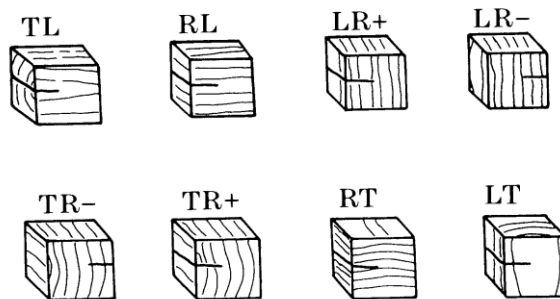


**Figura 1.** Sistemi di frattura nel legno [21]

Inoltre, i ricercatori [21] hanno osservato che la frattura dovuta al Modo I avviene principalmente per rottura della parete cellulare nei legni a bassa densità relativa (la densità relativa è definita come il rapporto tra la densità del legno e quella della parete cellulare).

Discorso diverso per i legni con alta densità relativa, in questo caso la rottura avviene per distacco tra le pareti cellulari di due cellule adiacenti. In base alla densità relativa del legno, una stima può essere fatta sulla tenacità a frattura in direzione parallela o perpendicolare alle fibre. La relazione che lega la densità relativa,  $\rho/\rho_s$ , e la tenacità a frattura nella direzione parallela alle fibre è la seguente [1,21]:

$$K_{Ic} = 1.8 \left( \frac{\rho}{\rho_s} \right)^{3/2} \quad (1)$$

Nel caso di propagazione parallela alle fibre,  $K_{Ic}$  risulta essere un decimo rispetto alla tenacità a frattura registrata nella direzione perpendicolare.

Nel caso di comportamenti complessi durante la frattura (per esempio, il bridging di fibre), due ulteriori parametri possono essere impiegati: il CTOD (crack tip opening displacement) e l'integrale  $J$ , con quest'ultimo che esprime il rilascio di energia durante il processo [17,40,42,45]. Per modellizzare questi comportamenti si fa riferimento alle leggi di coesione teorizzate da Dugdale e Barenblatt [40,41]. Questo modello presuppone l'esistenza di una zona (fracture process zone o FPZ), all'apice della cricca, dove i meccanismi di frattura si manifestano ben prima della propagazione della cricca stessa [46,47]. La legge di coesione permette di esprimere lo stress all'apice della cricca in funzione dell'integrale  $J$  e di CTOD (qui indicato come  $\delta$ ). La formula generale della legge di coesione è espressa come:

$$\sigma(\delta) = \frac{dJ}{d\delta} \quad (2)$$

## Il legno trasparente

Il primo articolo che menziona la produzione del legno trasparente risale al 1992 [49]. In quel caso, però, il materiale era stato pensato solo come un mero mezzo per facilitare l'osservazione della struttura interna dell'albero e niente più. Solo recentemente è stato riscoperto e rivalutato come possibile materiale per applicazioni strutturali e non solo [5,20].

Per rendere trasparente il legno comune tre problematiche devono essere risolte: 1) riduzione dello scattering tra i composti che formano il legno, 2) eliminare i gruppi responsabili dell'assorbimento della radiazione luminosa (principalmente lignina) e 3) minimizzazione della porosità che agisce come ulteriore fonte di scattering [7,13]. Rimuovere la lignina ha il doppio vantaggio di diminuire l'assorbimento di luce fino al 95% e di ridurre lo scattering [7,20], inoltre, la delignificazione preserva la struttura del template e aumenta la porosità in vista dell'impregnazione. Differenti trattamenti di delignificazione sono stati sviluppati dai diversi gruppi di ricerca [7,50]. Alla fine del processo, qualsiasi sia il trattamento utilizzato, il template di legno risulta essere di color bianco a causa scattering causato dalla differenza di indice di rifrazione tra l'aria, che riempie le porosità della struttura, e i componenti del legno quali cellulosa ed emicellulosa (entrambe con  $n \approx 1,53$ ) [7,20], per questo motivo il template delignificato viene infiltrato con un polimero avente un indice di rifrazione quanto più simile al suo. I più utilizzati sono PMMA e resine epossidiche [5,7,14,20,50]. Lo step finale del processo produttivo consiste invece in un trattamento termico per promuovere la polimerizzazione [20].

In campioni spessi 1,2 mm, il legno trasparente mostra una trasmittanza ottica vicina al 90% [4]. La bassa conduttività termica ( $0,15 \text{ W m}^{-1} \text{ K}^{-1}$ ) unita al fatto che quando si rompe non produce schegge pericolose, lo rendono un'alternativa interessante al vetro sodico calcico comunemente usato nel settore edilizio [6,7,13,22]. Tuttavia, il legno trasparente presenta ancora alcune criticità. Infatti, essendo ancora prodotto solamente in laboratorio, il processo produttivo risulta lento, energivoro e poco efficiente. Per quanto riguarda il trattamento di delignificazione, esso richiede un'ingente quantità di prodotti chimici dannosi per l'uomo e per l'ambiente e il cui riciclo è spesso difficile da realizzare [7,50,51]. In aggiunta, c'è un limite sullo spessore massimo con cui questo materiale può essere prodotto se si vuole mantenere un'elevata trasmittanza ottica [6,7,51,52]. Analogamente, il rinforzo (ossia la cellulosa e l'emicellulosa) non deve superare il 30% del volume del composito, pena un peggioramento delle proprietà ottiche [4,7]. Infine, un importante parametro che non deve essere trascurato quando si produce questo biocomposito è la compatibilità tra matrice polimerica e rinforzo. Infatti, spesso si utilizzano polimeri idrofobici mentre il template ha un comportamento idrofilico, e ciò si traduce in una cattiva adesione e pertanto in un peggioramento delle proprietà ottiche e meccaniche [7,22].

Diverse strategie sono state adottate nel cercare di risolvere alcuni dei problemi appena descritti [50]. Ad esempio, si è valutato, peraltro con promettenti risultati [52], la realizzazione di un biocomposito multistrato, in modo da rendere più efficiente il processo di delignificazione quando si vogliono produrre campioni con spessori maggiori. Differenti team di ricerca hanno ridotto il consumo di composti chimici e di energia durante la delignificazione provando a eliminare esclusivamente i gruppi cromofori della lignina e non l'intero composto [15,51], ottenendo, tra l'altro, migliori proprietà meccaniche grazie al mantenimento della lignina all'interno del template [15]. Per migliorare l'adesione tra polimero e rinforzo e quindi poter produrre compositi dallo spessore maggiore, si è provato

ad acetilare il template delignificato [22]. Il risultato è stato quello di migliorare la compatibilità tra i due componenti tramite la riduzione dell'idrofilicità della parete cellulare.

Analogamente al legno, il comportamento meccanico del legno trasparente risulta essere anisotropo e fortemente influenzato dalla frazione in volume di rinforzo [7-20]. Ovviamente, le proprietà migliori sono registrate nella direzione parallela alle fibre, con valori doppi di rigidezza e resistenza a trazione rispetto alla direzione normale alle fibre. Inoltre, sempre in questa direzione, le proprietà sono migliori sia di quelle del polimero sia di quelle del legno. Per quanto riguarda le proprietà nella direzione perpendicolare alle fibre, Jungstedt et al. [14] hanno misurato, per un composito betulla delignificata/PMMA, una resistenza a trazione inferiore a quella del PMMA, oltre ad osservare una rottura di tipo fragile lungo questa direzione. Come accennato precedentemente il legno trasparente è spesso visto come una possibile alternativa al vetro per la produzione di finestre, non deve quindi stupire che questi due materiali siano stati confrontati [15]. Il risultato ha dimostrato che, in generale, il legno trasparente possiede una risposta meccanica migliore.

## Materiali e Metodi

### *Preparazione dei campioni*

Nove campioni sono stati preparati per ciascun materiale analizzato. Sia il legno di betulla sottoforma di tavola (spessore 3 mm e densità 772 kg/m<sup>3</sup>) sia quello in forma di piallaccio presentavano le fibre disposte parallelamente alla superficie. Il legno trasparente è stato invece prodotto nel laboratorio del dipartimento di biocompositi del KTH.

Per prima cosa i piallacci (spessore 0,5 mm) sono stati tagliati in pezzi più piccoli di dimensione 100x100 mm<sup>2</sup>. La delignificazione, che segue il processo sviluppato al KTH [3,7,14], prevede di lasciare i piallacci in una soluzione buffer acetata (pH=4,6), a cui è aggiunto 1,25% in peso di NaClO<sub>2</sub>, il tempo necessario affinché diventino incolore (circa 6 ore a 75 °C). I piallacci vengono quindi risciacquati tre volte in acqua deionizzata sottovuoto, successivamente in etanolo e infine in acetone (sempre tre volte e sempre in vuoto). L'uso di etanolo e acetone migliora la stabilità dimensionale del template e ne facilita l'impregnazione [14]. Lo step successivo consiste nell'infiltrazione da parte del polimero (in questo caso polimetilmelacrilato). Il monomero del PMMA è stato prima filtrato per rimuovere l'inibitore e poi prepolymerizzato a 75°C. Quattro piallacci delignificati sono stati quindi immersi nel prepolymero per un'intera notte e dopodiché sono stati sovrapposti, avendo cura che avessero tutte le fibre orientate nella medesima direzione, racchiusi tra due lastre di vetro e fasciati con fogli di alluminio. Il composito è stato quindi messo in forno per 3 ore a 35°C per poi aumentare la temperatura a 45°C. Dopo ulteriori 3 ore la temperatura è stata portata a 70°C e lasciata invariata per un'intera notte. Al termine del trattamento termico è stato estratto dal forno, si è così ottenuto il campione di legno trasparente mostrato in Figura 2.



**Figura 2.** Legno trasparente multistrato

In seguito, i campioni sottoposti a flessione a quattro punti sono stati tagliati per mezzo di una sega portatile per legno. Il taglio è stato effettuato in modo che le fibre fossero orientate parallelamente al lato corto dei campioni stessi. Invece i provini utilizzati per la valutazione della tenacità sono stati ottenuti tramite il taglio laser. Sfruttando il taglio laser è stato possibile evidenziare la microstruttura altrimenti difficile da osservare nei campioni tagliati tramite sega. Anche la cricca, realizzata in modo che si propagasse lungo il sistema TR, è stata effettuata al laser e poi affilata con una lama da rasoio. Infine, i campioni sottoposti all'analisi tramite DIC, pur essendo sottoposti a prove in situ, sono stati preparati

utilizzando la sega invece che il laser, in quanto non si era interessati ad osservarne la microstruttura, per poi essere spruzzati di inchiostro al fine di creare il pattern necessario all'analisi.

### *Caratterizzazione dei campioni*

La frazione in volume di parete cellulosa,  $V_f$ , è stata valutata per entrambi i materiali.

All'interno di microscopio elettronico a scansione da banco (Hitachi TM-1000) sono stati eseguiti i test in situ di flessione a quattro punti su provini single-edge notched e la caratterizzazione dei materiali.

Il test di flessione a quattro punti ha fornito una misura del modulo di Young e della resistenza alla flessione nella direzione trasversale. La prova è stata condotta utilizzando un macchinario Instron 5566 Universal Testing Machine equipaggiato con una cella di carico da 500 N. Il setup è stato organizzato in modo che i risultati fossero consistenti con quelli misurati dalle prove in situ. Il modulo elastico è stato ricavato utilizzando l'equazione [66]:

$$E_T = \frac{d^2[3L - 4d]}{bh^3} \frac{dP}{dw} \quad (3)$$

Dove  $d$  è la distanza tra il supporto e punto di carico più vicino,  $L$  è la distanza tra i due supporti,  $b$  e  $h$  sono rispettivamente larghezza e spessore del campione e  $\frac{dP}{dw}$  è la pendenza della curva carico- deflessione.

La resistenza a flessione è stata invece calcolata utilizzando l'equazione [67]:

$$\sigma_T = \frac{3P_c(L - l)}{2bh^2} \quad (4)$$

Dove  $l$  è la distanza tra i punti di carico.

Invece, i test in situ all'interno del microscopio elettronico sono stati eseguiti sfruttando un microster (Deben Microtest 200N) equipaggiato con una cella di carico da 50 N. Il vantaggio nell'utilizzare prove in situ risiede nel fatto di poter osservare i meccanismi di frattura in tempo reale senza essere costretti a dedurli a posteriori [68]. Basandosi sulla letteratura [43] si è optato per un approccio che prevedesse il calcolo dell'integrale  $J$  per la stima della tenacità a frattura. L'integrale  $J$  è stato quindi ottenuto tramite l'equazione [16,45]:

$$J_{Ic} = \frac{2U(P_c)}{(h - a)b} \quad (5)$$

Dove  $U(P_c)$  è l'area sottesa dalla curva carico-deflessione nel punto di carico critico e  $a$  è lunghezza della cricca.

Successivamente la tenacità a frattura è stata espressa sottoforma di fattore critico di intensità degli sforzi elastoplastico equivalente [69] per mezzo dell'equazione [16]:

$$K_{Jc} = (J_{Ic} E_T (1 - v_{TR}^2))^{1/2} \quad (6)$$

Per semplicità,  $K_{Jc}$  d'ora in poi verrà indicato come  $K_{Ic}$

Per calcolare  $K_{Ic}$  è stato necessario utilizzare il coefficiente di Poisson,  $v_{TR}$ , che per il legno trasparente è stato stimato tramite l'equazione [70]:

$$v_{TR} = v_w V_w + v_{PMMA} (1 - V_w) \quad (7)$$

Dove  $v_w$  è il coefficiente di Poisson del template mentre  $v_{PMMA}$  quello del polimero

Per condurre l'analisi DIC alla fine di ottenere l'andamento dei campi di deformazione dalle immagini ottenute al SEM è stato utilizzato il software VIC-2D.

Per ottenere l'equazione della legge di coesione per i due materiali studiati, i dati ottenuti sfruttando l'equazione (5) sono stati plottati insieme al CTOD utilizzando il software MATLAB® per poi essere fittati e derivati.

Lo studio preliminare di selezione dei materiali è stato effettuato utilizzando il software Ansys Granta EduPack.

## Risultati e Discussione

I grafici che mostrano l'andamento del carico in funzione della deflessione, ottenuti dalla prova di flessione a quattro punti, sono riportati in Figura 3.

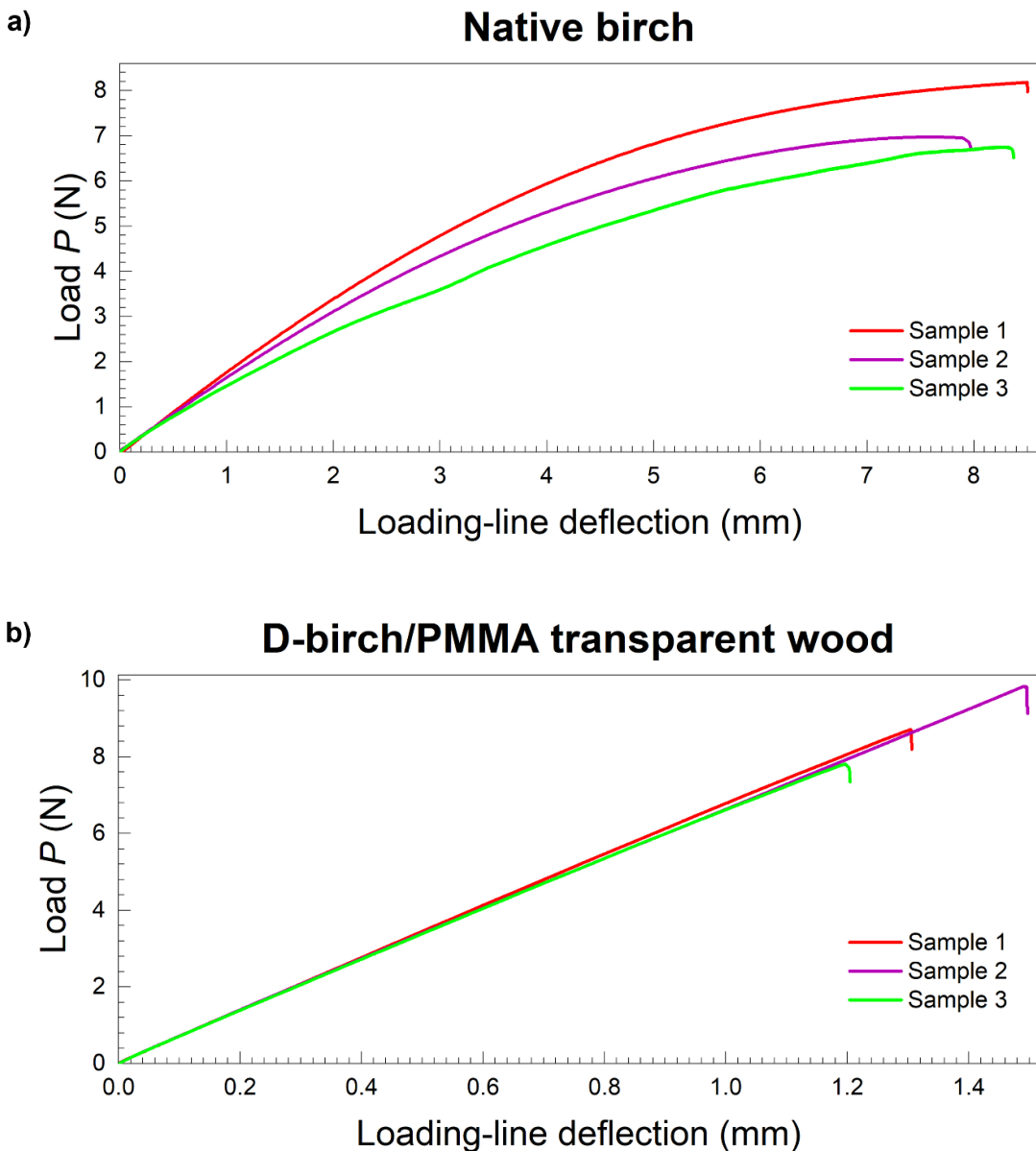


**Figura 3.** Grafici ottenuti dalla prova di flessione a quattro punti per a) legno di betulla e b) legno trasparente.

La deflessione del legno trasparente nella direzione trasversale risulta essere circa un ottavo di quella del legno tradizionale. Tale fenomeno è probabilmente dovuto al fatto che nel biocomposito la parete cellulare non può flettersi liberamente a causa del PMMA che

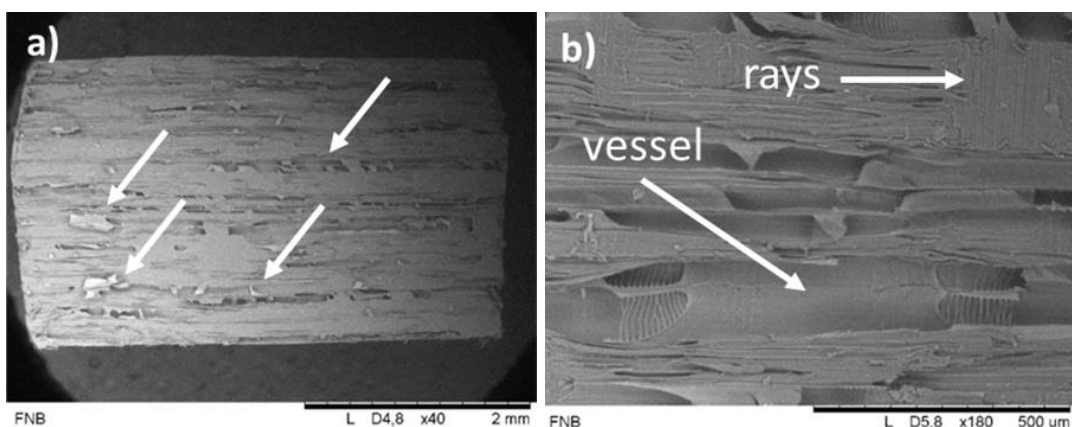
riempie il lume della cellula [1,14]. Inoltre, si può osservare che il TW presenta un comportamento lineare elastico a differenza del legno di betulla.

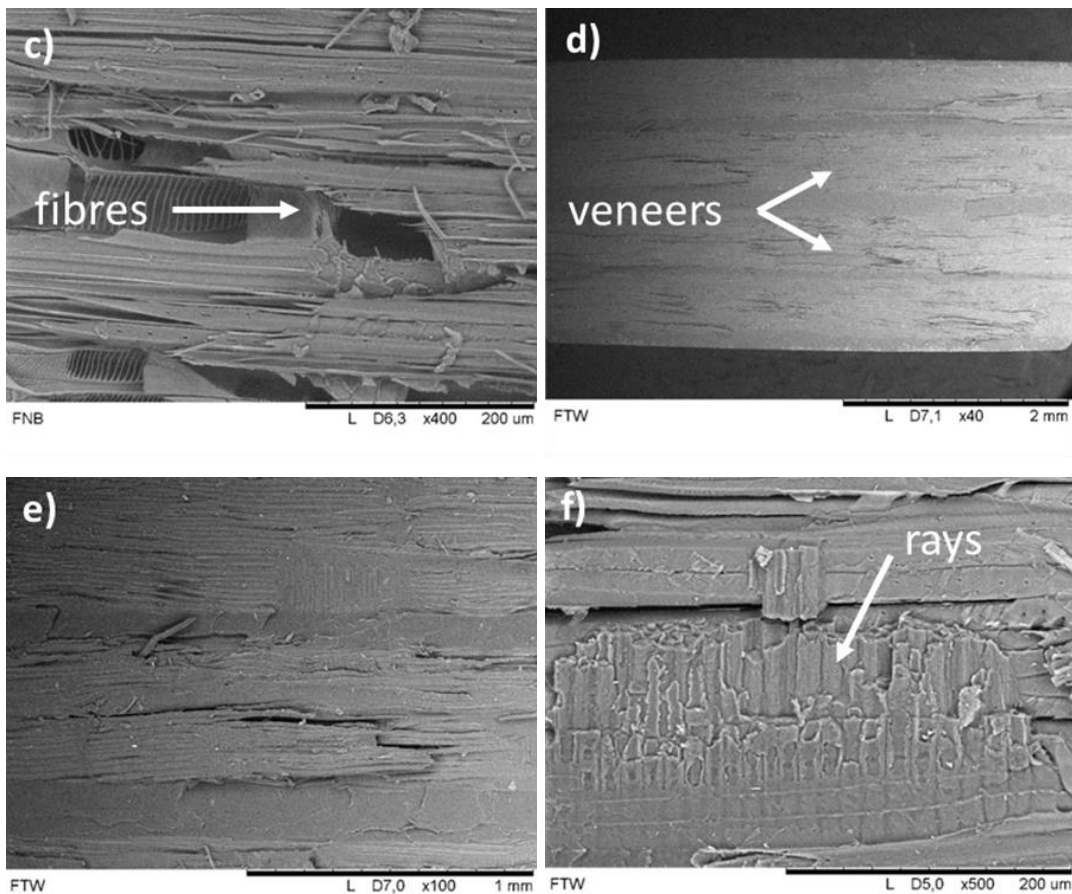
La Tabella 1 riporta alcune delle proprietà misurate. Il modulo elastico nella direzione trasversale del legno trasparente e del legno tradizionale, rispettivamente circa 3,3 GPa e 0,5 GPa, sono consistenti con i dati presenti in letteratura [14]. Il modulo del legno trasparente risulta essere superiore alla somma dei moduli di Young dei suoi componenti, infatti, il PMMA sopprimendo la flessione della parete cellulare rende il materiale più rigido. Analizzando invece i valori di resistenza a flessione, si osserva che questa migliora solo marginalmente rispetto a quella del legno nativo, rimanendo comunque molto inferiore rispetto alla resistenza del PMMA. Una possibile causa di ciò può essere una cattiva adesione tra polimero e parete cellulare che non garantisce un'efficace distribuzione degli stress.

**Tabella 1.** Proprietà meccaniche della betulla, del PMMA e del legno trasparente

Proprietà	Betulla	PMMA [1,2]	Legno trasparente
$E_T$ (GPa)	$0.5 \pm 0.1$	2.4	$3.3 \pm 0.0$
$\sigma_T$ (MPa)	$11.6 \pm 0.8$	117.9	$17.2 \pm 2$
$V_f$ (%)	0.51	/	0.23
$v_{TR}$	0.38 [3]	0.35	0.36

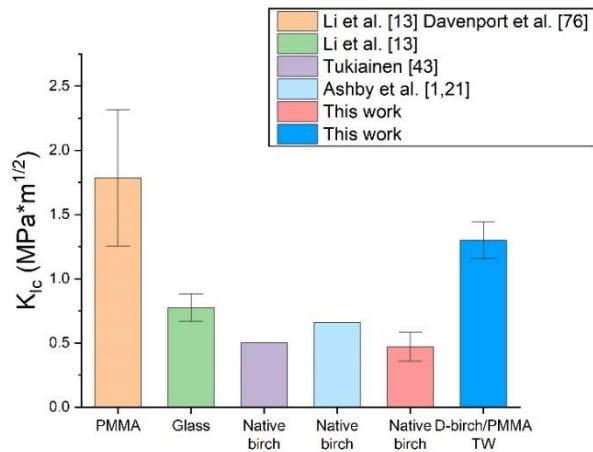
Alla fine della prova le superfici di frattura sono state osservate al SEM. Analizzando quelle del legno di betulla si può osservare che alcuni vasi presentano la rottura della parete cellulare (Figura 4 (a) e (b)). Inoltre, cellule del parenchima radiale possono essere individuate nella Figura 4 (c) suggerendo che la frattura si sia propagata lungo tali cellule. Se si osserva invece la superficie di frattura del legno trasparente, i differenti layers che la compongono possono essere facilmente identificati in Figura 4 (d). Considerando la Figura 4 (e) si può notare che in generale il polimero ha raggiunto l'intero substrato, tuttavia, la Figura 4 (f) mostra alcuni vuoti tra le fibre, probabilmente dovuti a una non perfetta impregnazione. Anche in questo caso si osservano cellule del parenchima radiale rotte, suggerendo che il meccanismo di frattura possa essere simile a quello del legno tradizionale.





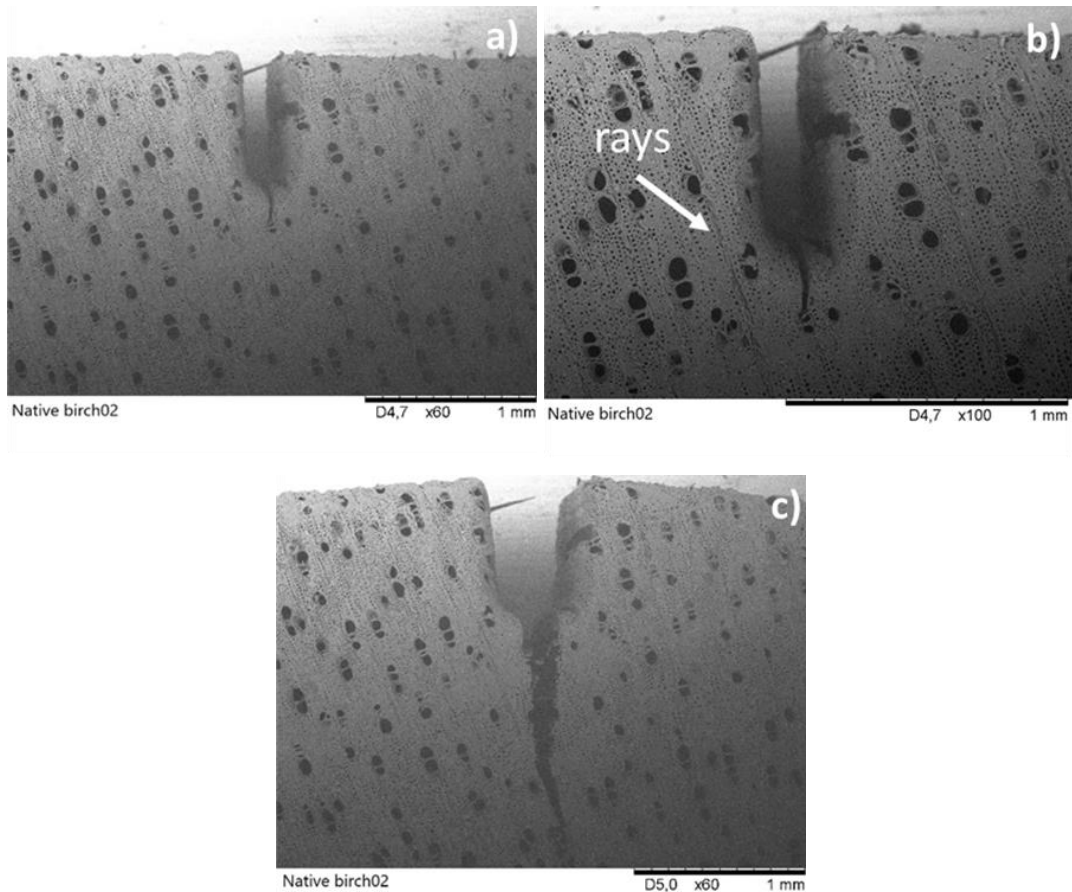
**Figura 4.** Superfici di frattura. (a)-(c) betulla e (d)-(f) legno trasparente

Analogamente alle prove tradizionali, anche nei test in situ si è osservato che il TW presenta una deflessione inferiore rispetto al legno tradizionale. I valori di tenacità a frattura per il legno trasparente e per la betulla sono confrontati in Figura 5 con i dati presenti in letteratura per lo stesso legno di betulla ma anche con il vetro e con il PMMA. Il valore di  $K_{Ic}$  misurato per la betulla ( $\approx 0,5 \text{ MPa m}^{1/2}$ ) è in linea con i dati presenti in letteratura [43] e con la stima effettuata utilizzando l'equazione (1). La tenacità a frattura del legno trasparente ( $\approx 1,3 \text{ MPa m}^{1/2}$ ) tende al valore medio di tenacità del PMMA puro [13,76], oltre a essere pressoché doppio di quello del vetro comune [13], giustificando così un possibile rimpiazzo di quest'ultimo nel settore edilizio.



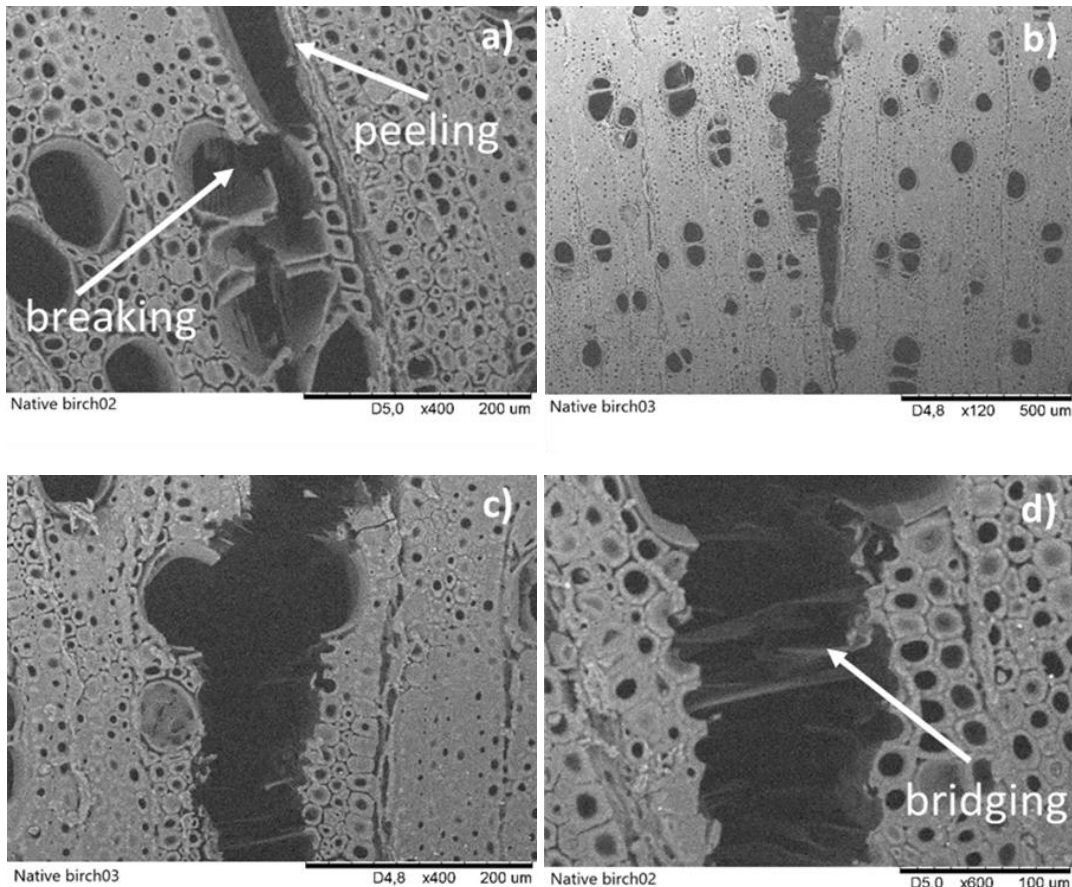
**Figura 5.** Grafico a barre mostrante la tenacità dei materiali considerati.

Esaminando le immagini acquisite durante le prove in situ di tenacità alla frattura è possibile osservare in Figura 6 come, per il legno tradizionale, la frattura si sia propagata lungo le cellule del parenchima radiale in quanto queste risultano essere punti di debolezza della struttura nel sistema TR [21].



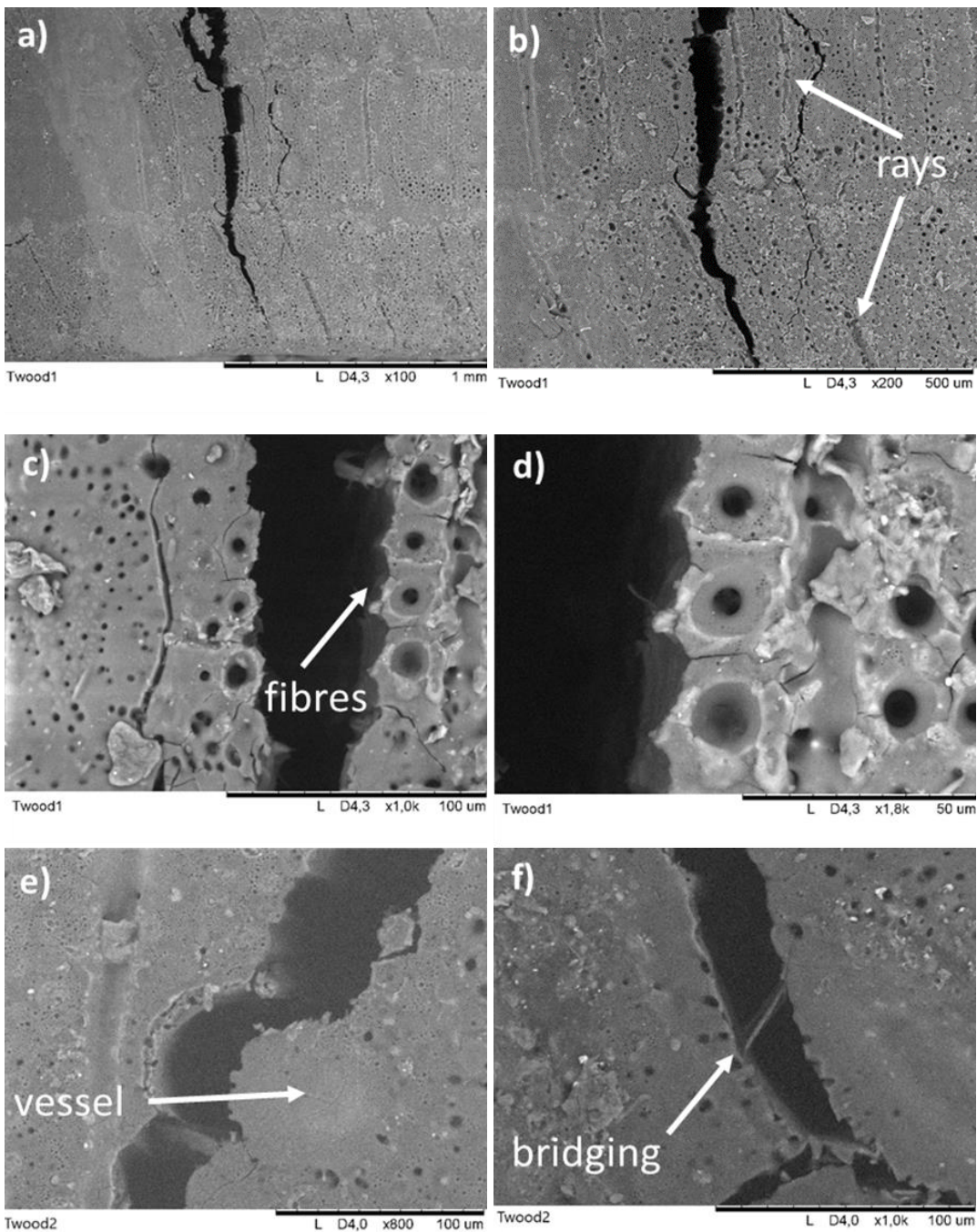
**Figura 6.** Legno di betulla (a)-(b) prima e (c) dopo la prova in situ

Se si studiano i meccanismi di frattura si osserva che la cricca si è propagata sia per frattura intracellulare sia per frattura intercellulare (vedere Figura 7 (a)-(c)). Interessante notare la presenza di fiber bridging (Figura 7 (d)), fenomeno solitamente non osservato per questo sistema di frattura su scala macroscopica [21,43].



**Figura 7.** Immagini SEM del legno di betulla. (a)-(c) frattura intercellulare e frattura intracellulare e (d) fiber bridging.

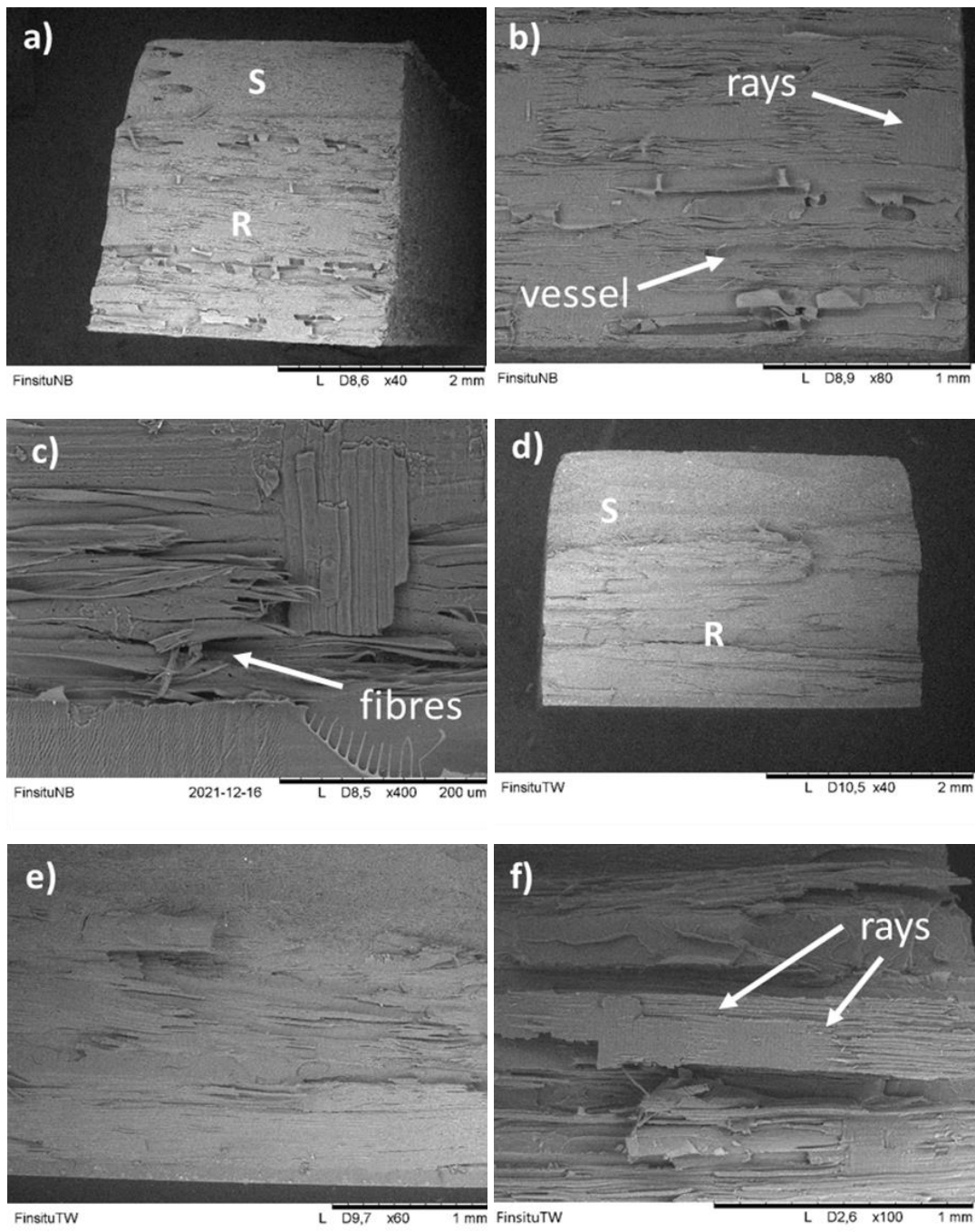
Per il legno trasparente è stato visto come la frattura si propaghi lungo le cellule del parenchima radiale dei piallacci (vedere Figura 8 (a) e (b)), esattamente come avviene nel legno tradizionale. Tra i differenti strati di biocomposito non è stata osservata nessuna delaminazione mentre è stato possibile riscontrare la rottura delle pareti cellulari così come la scollatura tra pareti cellulari adiacenti (vedere Figura 8 (c)-(e)). Il distacco avviene probabilmente al livello della lamella mediana, qui si trova infatti l’interfaccia PMMA/parete cellulare. Figura 8 (f) mostra come il fiber bridging avvenga anche nel legno trasparente. Infine, è stata notata la presenza di microcricche che si diramano a partire dalla cricca principale. La porosità che si osserva nelle immagini è dovuta al taglio laser. Essa non va a intaccare le proprietà meccaniche in quanto risulta interessare solo lo strato superficiale di PMMA.



**Figura 8.** Immagini SEM per il legno trasparente. (a) e (b) propagazione della cricca, (c) e (d) scollatura delle pareti cellulari, (e) frattura della parete cellulare e (f) fiber bridging.

Analogamente a quanto fatto per i provini testati tramite flessione a quattro punti, le superfici di frattura dei campioni in situ sono state studiate. Per il legno di betulla sono stati identificati alcuni vasi e fibre rotti e la presenza di cellule del parenchima radiale (vedere Figura 9 (a)-(c)). Per il biocomposito, a differenza di quanto si osserva nella superficie di frattura del test precedente, è quasi impossibile identificare la struttura a strati (vedi Figura 9 (d)-(f)). È interessante osservare che, in Figura 9 (f), alcune cellule del parenchima radiale possono essere individuate, ciò avvalora l'ipotesi che la frattura si propaghi in modo analogo sia nel legno trasparente che nel legno comune. Inoltre, non si osservano modifiche

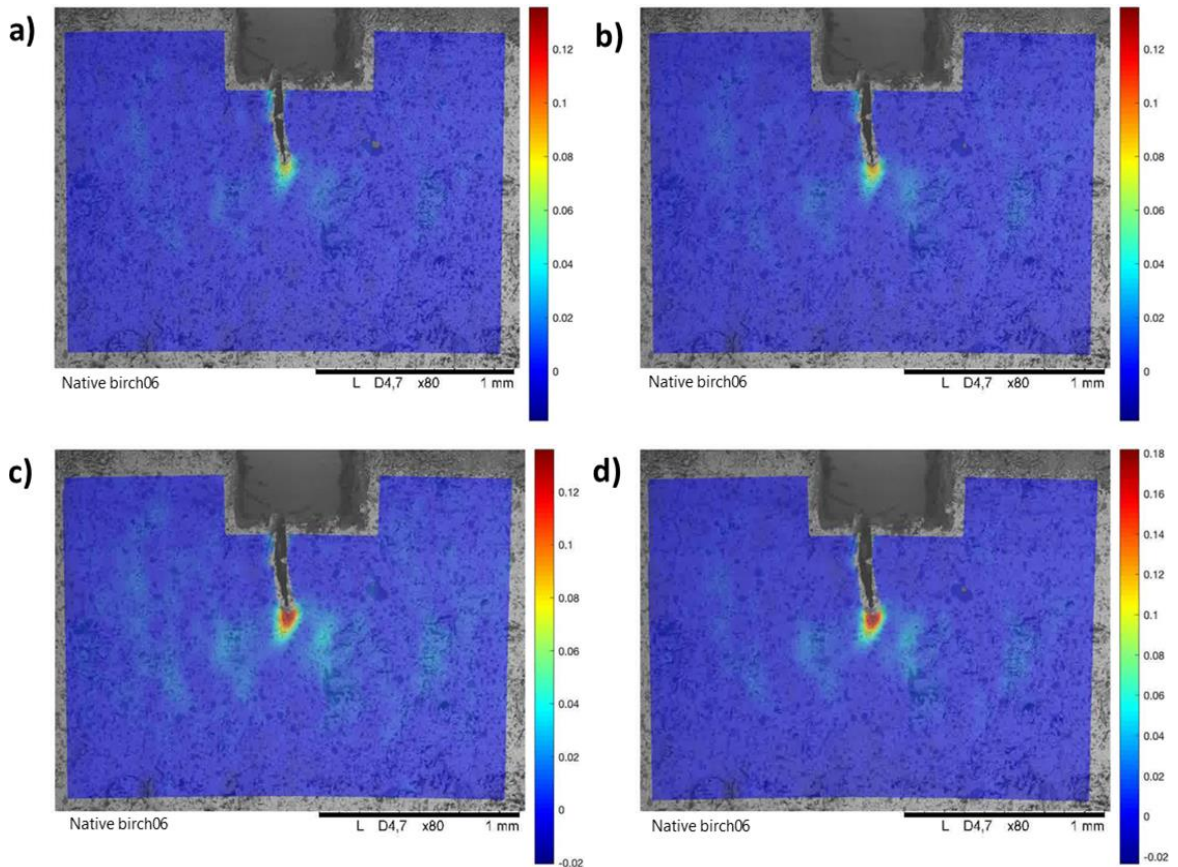
dovute alla struttura interna dovute al laser avvalorando quindi l'affermazione precedentemente secondo la quale il laser non provoca variazioni microstrutturali interne.



**Figura 9.** Superfici di frattura. (a)-(c) betulla e (d)-(f) legno trasparente.

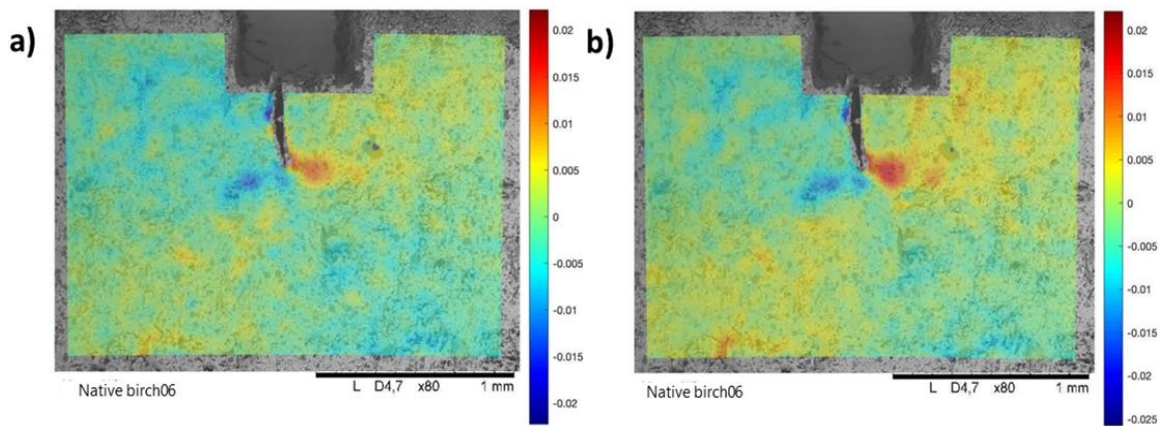
L'analisi DIC si è concentrata nello studiare i campi di deformazione  $\varepsilon_T$  ed  $\varepsilon_{TR}$ . La Figura 10 mostra il campo di deformazione  $\varepsilon_T$  per il legno di betulla. L'aumento di deformazione intorno all'apice della cricca suggerisce la presenza della fracture process zone. Nel legno, la FPZ è causata da meccanismi di dissipazione di energia quali microcricche e fiber

bridging [77,78] che contribuiscono ad incrementare la tenacità del materiale. Infine, si può osservare come la zona di processo sia limitata al solo intorno della cricca.



**Figura 10.** Campo di deformazione  $\varepsilon_T$  del legno di betulla prima della propagazione della cricca.

Considerando la deformazione  $\varepsilon_{TR}$  (vedi Figura 11) si osserva una zona rossa scura corrispondente a un'area di concentrazione degli sforzi probabilmente dovuta alla presenza di inomogeneità nella struttura del materiale.



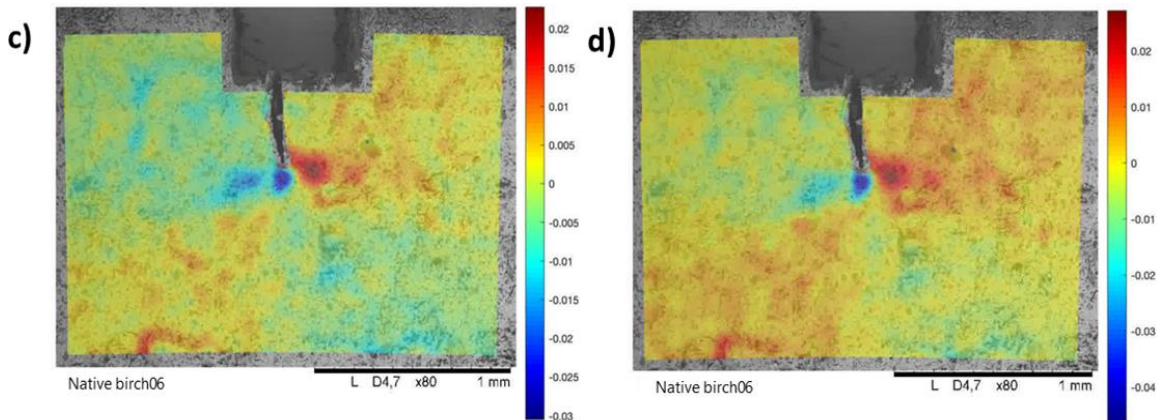


**Figura 11.** Campo di deformazione  $\varepsilon_{\text{TR}}$  del legno di betulla prima della propagazione della cricca.

Il campo di deformazione  $\varepsilon_T$  per il legno trasparente è invece mostrato in Figura 12. In questo caso la FPZ risulta estendersi per una distanza maggiore rispetto a quella del legno nativo.

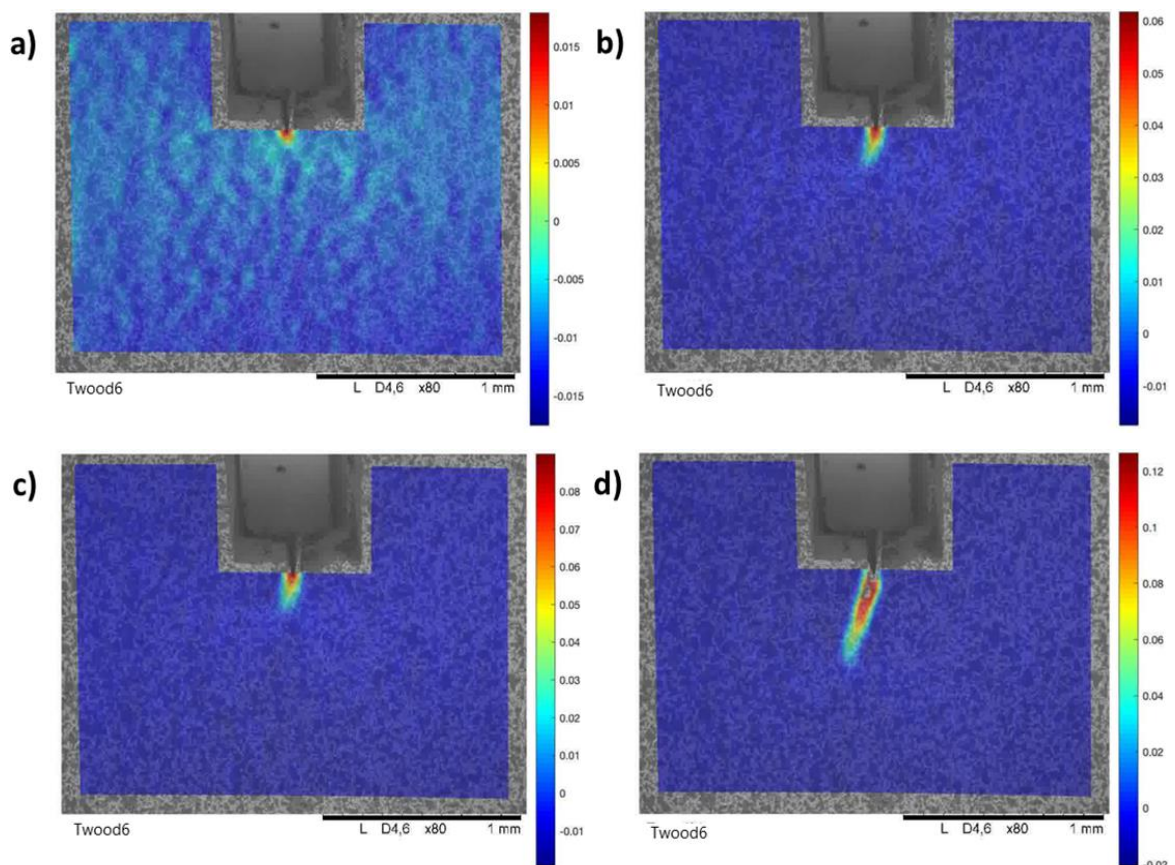


**Figura 12.** Campo di deformazione  $\varepsilon_T$  del legno trasparente prima della propagazione della cricca.

Studiando invece la deformazione  $\varepsilon_{\text{TR}}$  (vedi Figura 13) si è avuta la conferma che la delaminazione non si verifica durante la propagazione della cricca. Questo suggerisce che il legame tra i diversi layers è sufficientemente buono per evitare una propagazione lungo l’interfaccia.

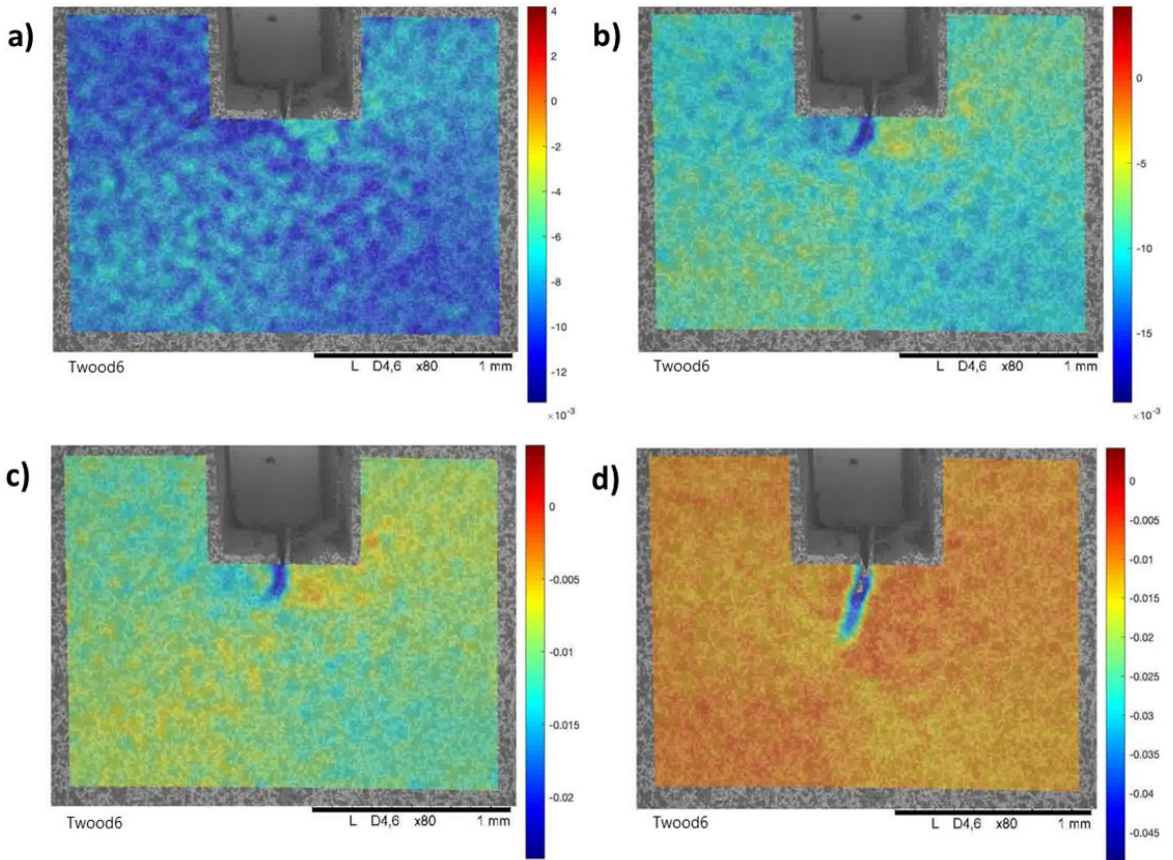


**Figura 13.** Campo di deformazione  $\varepsilon_{\text{TR}}$  del legno trasparente prima della propagazione della cricca.

Dalle osservazioni in situ si deduce che il fiber bridging per il legno trasparente, pur essendo presente come mostrato in Figura 14, non è esteso come nel caso del legno di betulla, suggerendo che lo sviluppo della zona di processo sia principalmente dovuto alla formazione di microcricche (vedi Fig. 8 (c)-(e)).

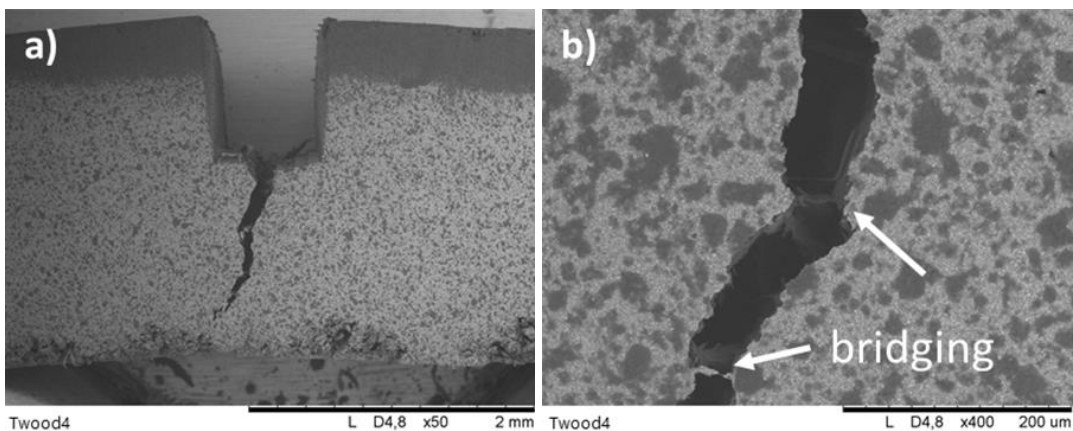


**Figura 14.** Fiber bridging nel legno trasparente.

Sulla base dei test e della analisi fin qui discussi, si è decisi di investigare la possibilità di applicare la legge di coesione ai materiali testati. Le curve che rappresentano l'interpolazione dei dati sperimentali del legno di betulla sono riportati in Figura 15.

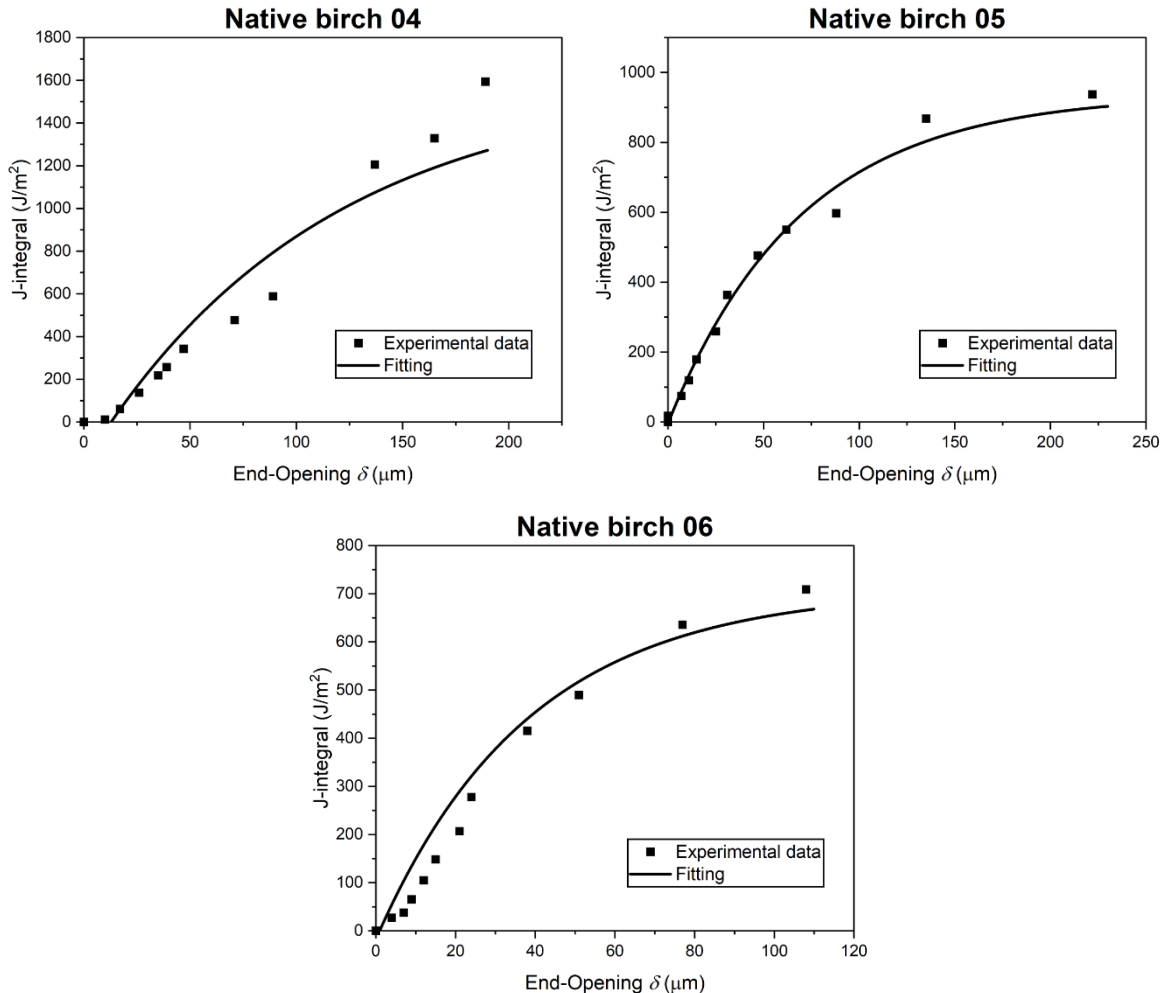


**Figura 15.** Interpolazione dei dati sperimentali per il legno di betulla.

La funzione che si è deciso di utilizzare è rappresentata dall'equazione generale:

$$J = a(1 - b \exp(-c\delta)) \quad (8)$$

Questa equazione è stata ricavata supponendo che l'andamento della legge di coesione per il sistema TR fosse simile a quello degli altri sistemi di frattura del legno [82]. I coefficienti ricavati dall'interpolazione e il valore di  $R^2$  sono riportati in Tabella 2.

**Tabella 2.** Parametri ottenuti dal fitting dei dati sperimentali della betulla

Campione	a	b	c	R <sup>2</sup>
Native birch 04	1593.5	1.123	9.042	0.9184
Native birch 05	937.5	1.004	14.42	0.9877
Native birch 06	708.8	1.089	24.32	0.9798

Le curve così ottenute sono state quindi derivate (vedere Figura 16) per ottenere l'andamento dello stress in funzione di  $\delta$ . Le curve risultanti sembrano consistenti tra loro e, inoltre, la differenza tra gli stress massimi è molto ridotta. Tuttavia, il principale obiettivo di questo studio era esclusivamente quello di verificare l'applicabilità della legge di coesione, con i dati che sembrano dimostrare che ciò è possibile ma comunque ulteriori studi sono necessari per una completa caratterizzazione della curva.

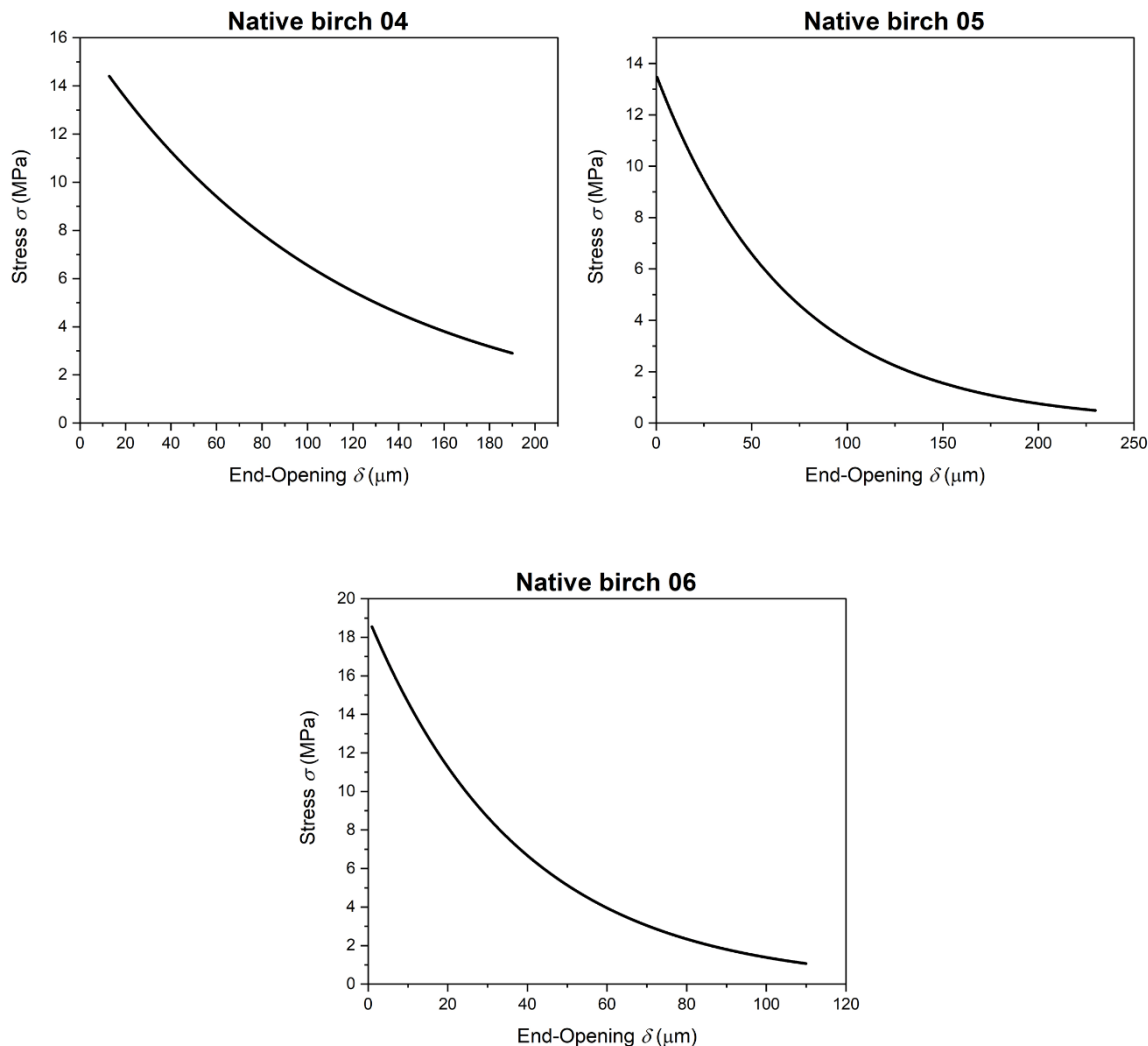


**Figura 16.** Andamento dello stress  $\sigma$  in funzione  $\delta$  nel legno di betulla.

La legge coesiva sembra essere soddisfatta anche per il legno trasparente come mostrato in Figura 17.

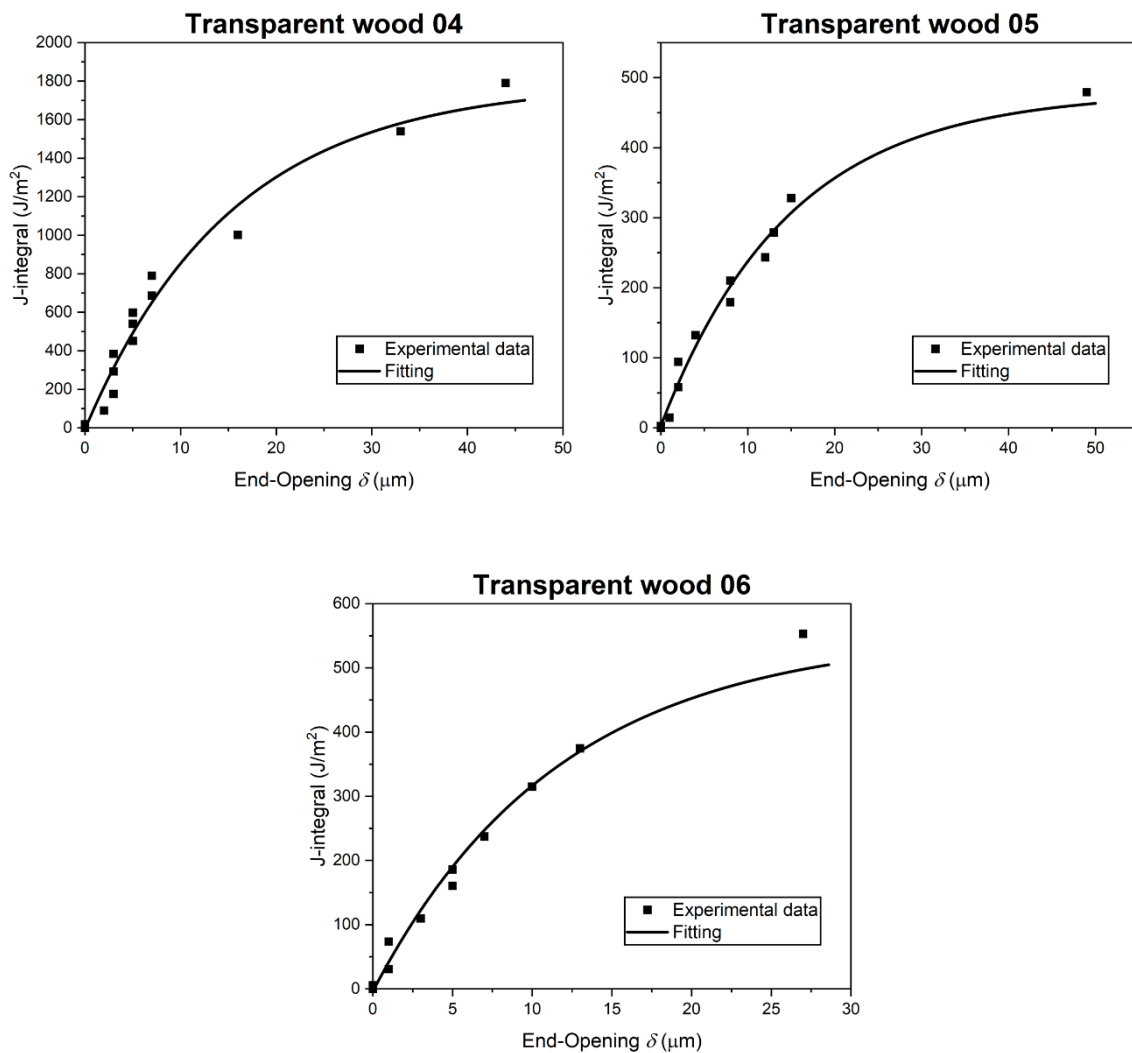


**Figura 15.** Interpolazione dei dati sperimentali per il legno trasparente.

L’equazione generale è la stessa del legno tradizionale (equazione 8). I coefficienti di fitting e il valore di  $R^2$  sono riportati in Tabella 3.

**Tabella 3.** Parametri ottenuti dal fitting dei dati sperimentali del legno trasparente

Campione	a	b	c	$R^2$
TW 04	1790.5	1.004	65.12	0.9708
TW 05	479.3	0.9938	67.83	0.9851
TW 06	553	1.007	85.59	0.9818

Le curve che mostrano l’andamento dello stress in funzione del crack tip opening displacement per il TW sono invece mostrate in Figura 18. In questo caso, i valori di stress massimo ottenuti differiscono molto, soprattutto nel caso del primo provino. Ciò può dipendere da molti fattori come la complessità della microstruttura o la presenza di difetti locali. Tuttavia, essendo uno studio preliminare, lo scopo era solamente quello di verificare la fattibilità dell’utilizzo della legge di coesione per il legno trasparente. Dai risultati

ottenuti, sembra ragionevole assumere che tale modello possa essere applicato alla frattura di questo biocomposito nel sistema TR, ma, così come per la betulla, sono necessarie ulteriori indagini.

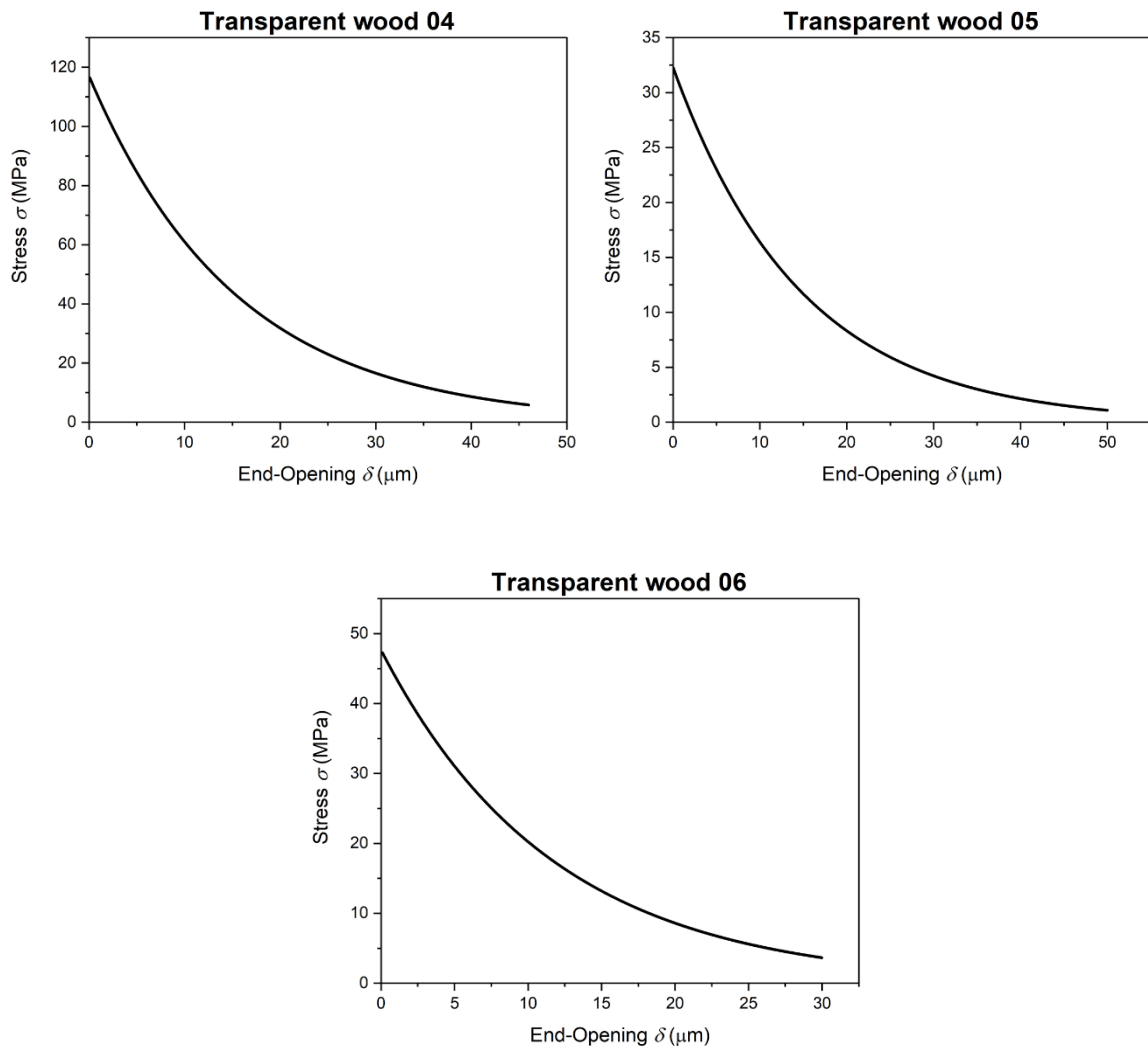


**Figura 18.** Andamento dello stress  $\sigma$  in funzione  $\delta$  nel legno trasparente.

Per concludere, i parametri quali modulo elastico, tenacità a frattura e resistenza a flessione sono stati utilizzati per dimostrare che tali grandezze possono essere utili nell'effettuare uno studio preliminare di design dei materiali basato sui criteri di Ashby [74]. Il grafico di Figura 19 è risultato essere il più significativo, esso mostra la tenacità a frattura rappresentata insieme alla densità, dove i materiali migliori sono considerati quelli che presentano bassa densità ed elevata tenacità. In questo caso, si osserva che il legno trasparente possiede una tenacità a frattura specifica maggiore rispetto ai vetri sodico calcico comunemente usati in edilizia.

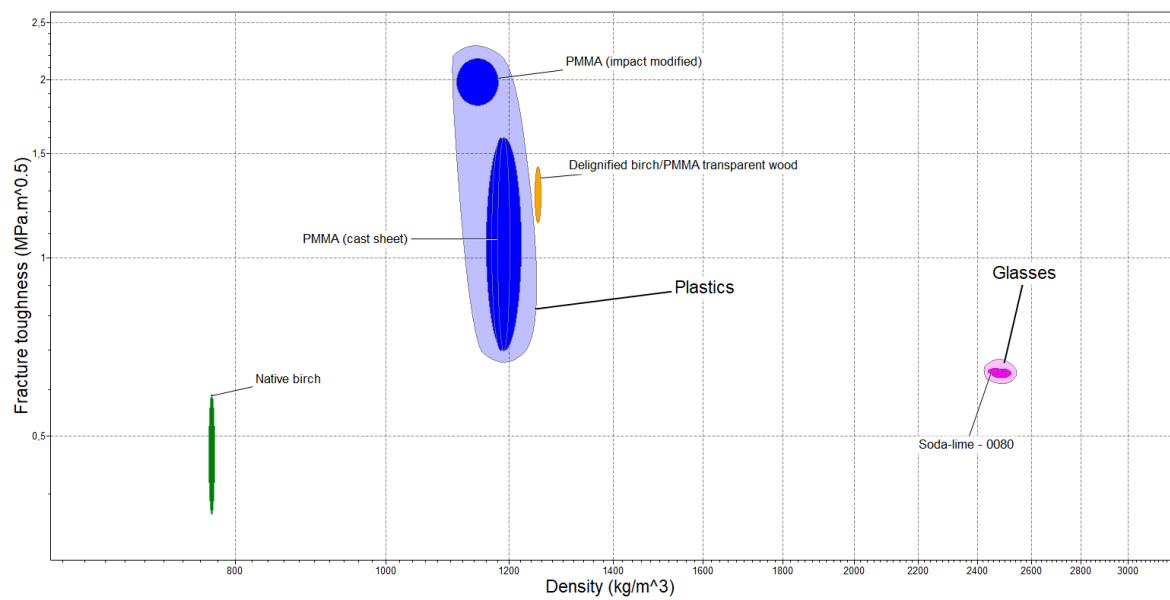


**Figura 19.** Diagramma di Ashby  $K_{Ic}$  vs densità

## **Conclusioni e lavori futuri**

L'obiettivo di questa tesi, ossia ampliare la conoscenza attuale sulla risposta meccanica del legno trasparente, è stato raggiunto. Inoltre, come risultato aggiuntivo, sono state fornite dimostrazioni della presenza di fiber bridging nella frattura lungo il sistema TR, così come dell'applicabilità della legge di coesione lungo il medesimo sistema di frattura per il legno di betulla.

Pur avendo contributo ad aumentare la comprensione sul comportamento meccanico del legno trasparente, tale lavoro non ha potuto fornire una caratterizzazione meccanica a 360 gradi. Per questo motivo c'è ancora molto da fare. Per esempio, occorrerebbe valutare l'effetto che trattamenti, quali l'acetilazione, hanno sulle proprietà meccaniche, così come occorrerebbe studiare l'influenza degli effetti viscoelastici sulla risposta meccanica. Infine, come menzionato, ulteriori indagini sono necessarie per caratterizzare in modo esaustivo la legge coesiva. Comunque, i dati ottenuti permettono di costruire le prime simulazioni numeriche sul comportamento del materiale.

## List of abbreviations

CTOD	Crack tip opening displacement
D-birch	Delignified birch
DIC	Digital Image Correlation
FPZ	Fracture process zone
L	Longitudinal
NW	Native wood
PMMA	Poly(methyl methacrylate)
R	Radial
RL	Radial-Longitudinal
SEM	Scanning electron microscope
T	Tangential
TL	Tangential-Longitudinal
TR	Tangential-Radial
TW	Transparent wood

# 1. Introduction

## 1.1 Background

Wood has been used as a structural material for millennia, as confirmed by the wooden artefacts found in the pyramids [4]. However, starting from the 19<sup>th</sup> century, it has been replaced by metals and concrete in most applications. In load-bearing structures, the demand for new materials that cope with sustainable development has grown enormously nowadays and immediate solutions are needed [5]. The human-made climate damage done since the first industrial revolution has led society to look more carefully at the material selection and what the environmental impact of this choice will be. In this light, wood-based composites have been gaining attention in the scientific community, especially transparent wood (TW) which has the potential to be used in load-bearing applications (e.g., in buildings) thanks to its good mechanical performance associated with lightweight [6]. Transparent wood is defined as a biocomposite where a delignified wood substrate has been impregnated by a refractive index-matching polymer [7,8]. In the synthesis of this biocomposite, delignification is essential to remove the chromophore groups from wood, while increasing the porosity for better infiltration of the polymer [6,9]. The match of refraction index between the wood and polymer also yields a higher optical transmittance for the composite, which is another added functionality besides the mechanical improvements. For this purpose, Poly(methyl methacrylate) PMMA is one of the most used polymers because its refractive index is fairly similar to that of delignified wood template [10]. In addition, this polymer guarantees excellent weather resistance [2], which is crucial in building applications.

It is worth mentioning that delignification can also be considered as a preparatory step for functionalization of wood as it increases the cell wall accessibility [9]. Indeed, wood functionalization is of great interest because it can widen the application areas of transparent wood outside the building sector [10]. A large effort has been put in order to tailor and characterize the functional properties of transparent wood biocomposites [6,7,9–14].

Unfortunately, a similar trend has not yet been seen in the study of mechanical properties. Very few works have investigated the mechanical behaviour [1,8,15–17], usually reporting only figures of the Young's modulus and the strength. However, the growing interest in this material is demanding and pushing for its full characterization.

Fracture toughness is one of the mechanical properties that should be addressed when a material is evaluated as a possible candidate for structural applications as it provides insightful information on the failure of the material itself [18]. Fracture toughness is studied by means of Fracture Mechanics. Approaches based on Fracture Mechanics are regularly applied to wood and wood-based materials, e.g., in machining problems [19,20].

However, the author has found only very few articles dealing with the fracture of transparent wood [15,17], although in a very limited way. Therefore, there is a lack in quantifying the fracture toughness for this versatile composite. The reasons behind this deficiency can be drawn as (i) the material is relatively new [8,21], and (ii) the fracture mechanisms are complex because of the hierarchical wood structure associated with the impregnated polymer that composed transparent wood. Nevertheless, a deep understanding of the failure mechanisms of this class of materials is necessary for their large-scale production and commercialisation.

## *1.2 Research Aims*

In this thesis, some of the mechanical properties of TW were quantified, especially its fracture behaviour. The TW biocomposite chosen for the study was a multilayer delignified-birch/PMMA transparent wood. The results were also compared with those of native silver birch wood (*Betula Pendula*) in the same experimental conditions and with data from literary studies. Birch wood was chosen as the template of TW because it is a high-density hardwood. Indeed, high-density hardwood species are the ideal raw material for transparent wood biocomposites as they guarantee an elevated wood volume fraction (important for the mechanical properties) compared to other types of wood [21].

First, the transverse elastic modulus and transverse flexural strength were evaluated by means of the four-point bending test. Then, the fracture toughness was quantified based on data acquired during in situ single-edge-notched four-point bending tests. Like in wood [4,22], the crack can propagate along eight different systems in transparent wood. In this work, it was chosen to study only the crack growth along the tangential-radial system (TR). Using in situ measurements inside an electronic microscope, it was possible to examine the failure behaviour of delignified birch impregnated with PMMA, which would otherwise have been difficult to study with conventional techniques due to the limited thickness of TW [23]. In situ tests also gave the chance to follow the crack growth during the experiment and to observe the damage mechanisms in real-time. The strain field was also measured during the in situ single-edge-notched four-point bending test through the digital image correlation (DIC) technique to pinpoint possible microdefects that might occur during the fracture process. Based on the results of the in situ experiments and the DIC analysis, it was feasible to obtain a preliminary cohesive law equation for TW, which is essential for predicting fracture of structures via numerical simulations. Finally, a demonstration that the properties found can be used for a basic material selection was given.

In conclusion, the main research goal of this thesis was to closely understand and characterize the failure mechanisms of delignified birch/PMMA transparent wood, while providing useful information for modelling the material behaviour.

## *1.3 Structure of the Thesis*

This work of thesis is divided into several sections organized as: Chapter 1, where the background and the aims of this thesis are introduced; Chapters 2 and 3 explain the structure and the properties of native wood and transparent wood, respectively; Chapter 4 aims to illustrate the production of transparent wood and the techniques used to characterize the materials; Then, in Chapter 5, the results from the analysis of the two materials are reported and discussed; Finally, the last chapter summarises what has been done and provides some ideas for future works.

## 2. Wood

The outstanding mechanical properties of wood depend on its hierarchical structure (see Figure 2.1). Indeed, this kind of structure is often used by nature (wood, bones, nacre, ...), as it guarantees excellent specific properties because it maximises performance using as little material as possible [24]. The hierarchical organization can be found at each scale level of the tree, from the trunk (macroscale) to the arrangement of the biocompounds of the single wood cell wall (nanoscale).

At the macroscopic level, wood consists of cells that can be modelled as empty tubes. For this reason, it is considered a cellular material at this length scale. However, looking at the single wood cell, the cell wall is composed of bundles of cellulose microfibrils embedded in a matrix of lignin and hemicellulose, making it more similar to a fiber composite [25].

Since the hierarchical structure of wood is the result of millions of years of adaptation to the surrounding environment, it has a great influence on the final properties of the material [25–27]. Therefore, a description of it is useful in order to understand the mechanical behaviour of wood.

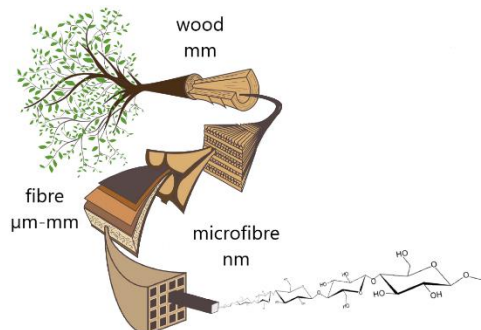


**Figure 2.1.** The hierarchical structure of wood [28].

### 2.1 Softwood and Hardwood

Normally wood is categorized into softwood and hardwood. They are tradenames, where softwood indicates the class of plants called gymnosperms while hardwood refers to species belonging to the class of angiosperms [29,30]. Looking at the microscopic structure, softwoods have a much simpler structure than hardwoods. This can be explained by the fact that gymnosperms are less advanced organisms from an evolutionary point of view than angiosperms.

In softwood, three types of cells can be recognized: tracheids, parenchyma, and epithelial cells. Tracheids are by far the most important cells, representing 90%-95% of the overall cell volume. They have an elongated shape, transport fluids through the tree, and provide mechanical support. During the spring, trees form the earlywood, which consists of tracheids with a thin cell wall and a large diameter (see Figure 2.2). During the summer, the latewood is made of tracheids with a thicker cell wall and a smaller diameter (shown in Figure 2.2). Depending on the climate of the region in which the tree grew, the transition between early and latewood can be quite sharp [30].

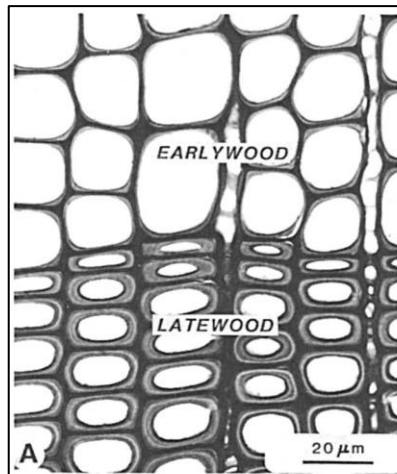


**Figure 2.2.** Micrography of the transition between latewood and earlywood [29].

In hardwood, the number of cell types is larger since the cells have become specialized. Therefore, the liquid transportation and the mechanical support are no longer provided by the same cell type as in softwood, but by two different kinds of cells, vessels and fibers, respectively. Moreover, another noteworthy type of cell is the ray parenchyma cell. The ray parenchyma extends perpendicular to the fibers along the radial plane [4,31]. Vessels, which can often be seen by the naked eye, have a large empty lumen and a thin cell wall with open ends and, when seen in the transverse section, look like holes. Because of the vessels, hardwoods are also known as “porous woods” [30,32].

As in softwoods, the change between early and latewood can be abrupt or not. Depending on the distribution and size of the vessels, three types of hardwood can be defined: “ring-porous”, “semi-ring porous” and “diffuse-porous” [30] (see in Fig. 2.3). In ring-porous woods, the difference in size between vessels of early and latewood can be up to an order of magnitude, whereas in diffuse-porous wood, the size of the vessels is fairly constant. Finally, semi-ring porous wood represents a condition in between ring-porous and diffuse-porous woods [30,32].

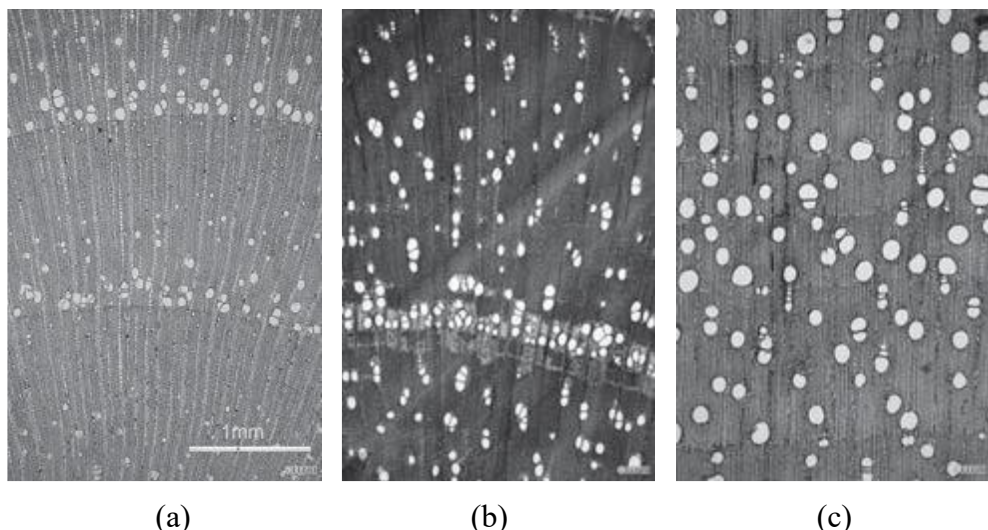


**Figure 2.3.** Microstructure of (a) ring-porous, (b) semi-ring porous, and diffuse-porous hardwoods [33].

## 2.2 Cell structure

As mentioned before, wood can be defined as a natural cellular material at a macroscale level [4]. The general wood cell structure consists of a central empty open portion (lumen) and cell wall [32]. In addition, the cell wall itself can be divided into three regions called middle lamella, primary wall, and secondary wall [30,32,34] as shown in Figure 2.4. This organization of the cell wall is common to most wood cells in both hardwood and softwood [32]. The three main compounds of the wood cell wall are cellulose, lignin, and hemicellulose [29,30,32,34].

Moving toward the centre of the cell, the middle lamella is the first layer that can be encountered. This lignin-rich layer binds the cells together enabling the transport of water and biochemicals in the tree [32]. The primary wall is the next layer and is formed by a single layer of randomly oriented cellulose microfibrils. The primary walls of two nearby cells and the middle lamella between them form the so-called compound middle lamella, as the three entities often appear indistinguishable even using a scanning electron microscope [30,32]. Finally, there is the secondary cell wall which consists of three layers ( $S_1$ ,  $S_2$ ,  $S_3$ ).  $S_2$  is the thickest one and forms most of the cell wall [30,32,34]. It is also the main responsible for the outstanding properties of wood. In  $S_2$ , the orientation of cellulose microfibrils is almost vertical. The angle between the cell axis and the microfibrils is defined as MFA (microfibril angle), small MFAs give excellent mechanical properties while the other way around is true with large MFAs.

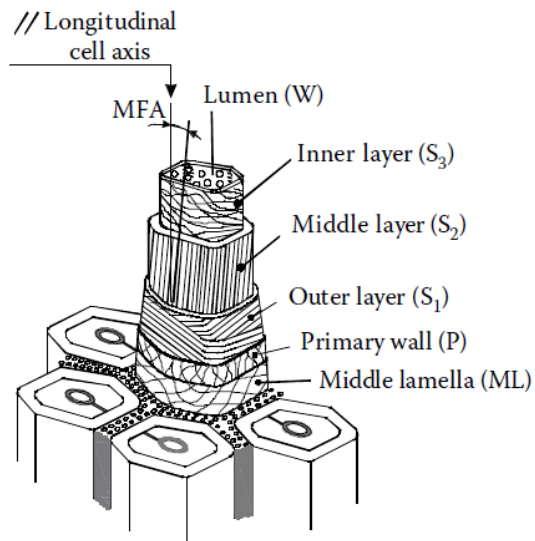


**Figure 2.4.** Representation of the cell wall structure [35].

## 2.3 *Betula Pendula*

*Betula Pendula*, commonly known as silver birch [36], is one of the countless existing subspecies of birch. Widespread throughout northern and eastern Europe [37], it belongs to the family of diffuse-porous hardwoods. Birch wood can be used in the form of veneer, timber, and plywood [38]. However, most of this wood is processed into plywood because of its use in structural applications [39,40]. The features of birch wood are its light colour, medium density, and moderate swelling and shrinkage during moisture fluctuations [38].

## 2.4 Mechanical properties of wood

The structure of wood, both at the macro and microlevel, makes it an anisotropic composite material [4,29]. Nevertheless, if the piece of wood is taken from a region of the trunk far enough from the centre, the curvature of the growth rings becomes negligible and the properties can be considered orthotropic [4]. Orthotropic means they change along the three orthogonal directions [32]. In wood, the three axes are called longitudinal (L), radial (R), and tangential (T) [4,32]. Along the longitudinal direction, also called axial direction or grain direction [19], the best mechanical properties are recorded since it is the axis parallel to the fibers. On the other hand, T and R axes are perpendicular to the fiber direction but the radial axis is normal to the growth rings while the tangential direction is tangent to them [32] as shown in Figure 2.5.

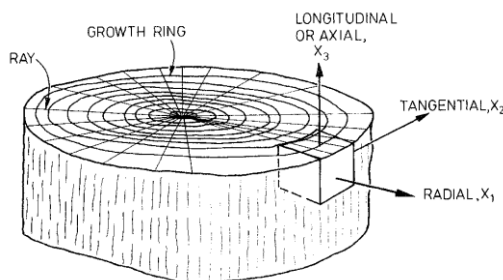


**Figure 2.5.** Axis arrangement in wood [4].

### 2.4.1 Fracture toughness of wood

As a brief introduction of fracture mechanics, the types of loading that promote the crack propagation can be attributed to three stress modes or a combination of them [41]. These modes are called Mode I, Mode II, and Mode III, respectively (see Figure 2.6).

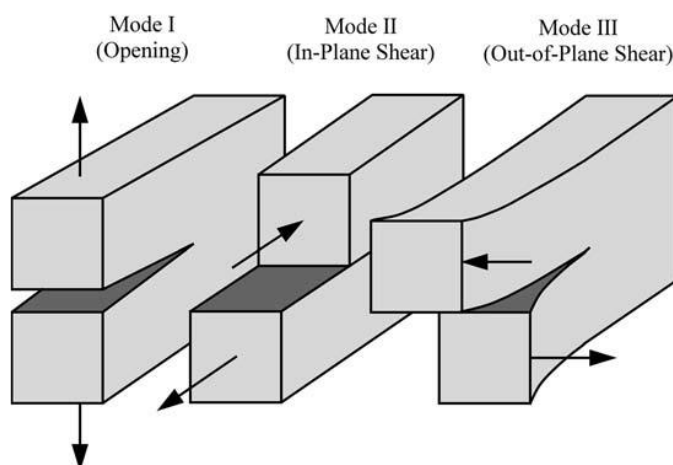


**Figure 2.6.** Modes of crack loading [41].

Mode I is when the crack opening is the result of a stress applied normal to the plane of the crack. On the other hand, if it is in-plane shear stress that generates the crack propagation

then Mode II occurs. Finally, in Mode III, the crack propagates because of out-of-plane shear stresses [41,42].

Each load mode is linked to a parameter called stress intensity factor,  $K$ , which is nothing more than a measure of the stress field around the crack tip. Therefore, three different intensity stress factors can be defined:  $K_I$ ,  $K_{II}$ , and  $K_{III}$  which refer to Mode I, Mode II, and Mode III, respectively. This parameter helps predict when the material failure is likely to occur as a result of the crack growth. Just before the crack starts propagating, the critical value of the stress intensity factor ( $K_c$ ) is reached for a specific mode of loading and this is regarded as a material property called fracture toughness [3,41,43].

The crack propagation in wood has been extensively investigated for its implications in structural and industrial applications [44]. Indeed, the understanding of the crack growth would save energy and reduce damage to the end product during industrial processes such as knife cutting. Ashby et al. [22] stated that the crack can propagate along eight different systems. Two letters are used to identify each system: the former is the direction normal to the plane in which the crack is located, the latter is the direction of the crack propagation (see Figure 2.7). In six of the eight systems, the crack propagates along the fiber direction; only in the LT and LR systems does the crack propagate through the grain.

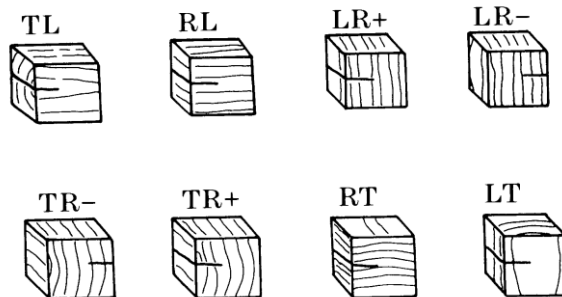


**Figure 2.7.** crack propagation systems in wood [22].

Two mechanisms are mainly responsible for the crack propagation in mode I in wood: cell wall breaking and cell wall peeling. If the relative density ( $\rho/\rho_s$ , the ratio between the density of the wood and that of the cell wall) is less than 0.2, the cell wall breaking is predominant. On the other hand, if  $\rho/\rho_s > 0.2$ , cell wall peeling is the main failure mechanism [22]. Furthermore, Ashby and his co-authors formulated two equations that link the relative density to the fracture toughness of wood along or normal to the fibers respectively. According to them, when the crack propagates along the fiber direction, a fair estimation of  $K_{Ic}$  can be obtained from the following equation [4,22]:

$$K_{Ic} = 1.8 \left( \frac{\rho}{\rho_s} \right)^{3/2} \quad (1)$$

In this direction, the fracture toughness is expected to be approximately one-tenth of that for a crack that grows normal to the grain [22].

For complex nonlinear fracture behaviour (e.g., fibre bridging in wood), fracture mechanics relies on two parameters: the crack tip opening displacement (called CTOD), displayed in

Figure 2.8, and the J-integral, where the latter is nothing more than the energy release rate during the process [18,41,43,45].

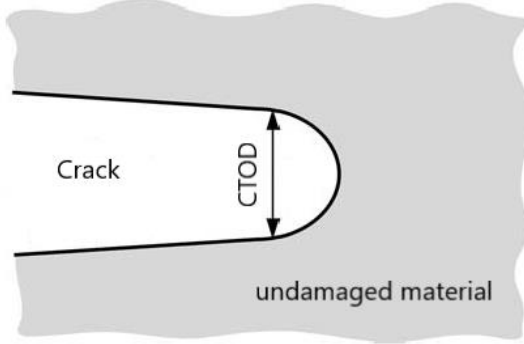


**Figure 2.8.** Sketch of the crack tip [41].

The approach discussed above was explored for the development of cohesive zone law, which was theorized by Dugdale and Barenblatt [41,42]. It was first applied to concrete [41] as the previous theories alone were not enough to explain the fracture behaviour of this material. In recent years, the cohesive law has also been successfully used to predict the failure of adhesive joints and fiber composites since it allows the modelling of phenomena of energy dissipation, such as bridging, by theorizing the existence of a fracture process zone (FPZ) ahead of the crack tip where these energy-dissipation mechanisms take place [46,47]. Moreover, when applied to wood, the cohesive zone model allows taking into account the intrinsic heterogeneity of this material [48].

The cohesive law explains the cohesive stress  $\sigma$  in the area around the crack tip in terms of J-integral and end-opening  $\delta$  ( $\delta$  corresponds to CTOD). These parameters are related to  $\sigma$  by the equation [47]:

$$\sigma(\delta) = \frac{dJ}{d\delta} \quad (2)$$

According to this model, when the critical value of end opening,  $\delta_c$ , is reached, J reaches a plateau ( $J_{ss}$ , steady-state J) and consequently,  $\sigma$  tends to zero [42,47].

### 3. Transparent wood biocomposites

Siegfried Frink [49] wrote an article entitled “Transparent Wood- A New approach in the Functional Study of Wood Structure” in 1992. This is recognized as the first paper that describes how transparent wood can be produced. However, the author’s purpose was to use this material as a means of observing the 3D internal structure of the wood rather than as a material in itself. For this reason, it should not sound strange that the comprehensive study of transparent wood only began about 25 years later Frink’s publication [8,21], when the scientific community understood the enormous potential of this biocomposite as structural material and more. Since then, different kinds of transparent wood have been developed, tailoring the wood structure in order to meet different needs [26,50].

#### *3.1 From native wood to transparent wood*

As can be experienced daily, wood is an opaque material. But why is this so? First of all, its chemical composition is inhomogeneous, and therefore, scattering occurs because of the difference in refractive indexes of its constituents. In addition, some of the compounds forming the cell wall act as strong light absorbers (mainly lignin). Finally, the porosity of its microstructure provides another source of scattering [10,15]. By minimising these three factors, wood can become transparent.

As a first step, it is necessary to extract lignin which is responsible for 80-95% of the light absorption in wood [10,21]. Removing lignin also reduces the scattering since it has a different refractive index (1.61) than cellulose and hemicellulose (1.53 for both) [10].

Lignin is extracted through a chemical treatment called delignification. Two main delignification processes have been developed: NaClO<sub>2</sub> method at KTH Royal Institute of Technology and NaOH/Na<sub>2</sub>SO<sub>3</sub> + H<sub>2</sub>O<sub>2</sub> method at the University of Maryland, however, other groups have modified these methods according to their needs [10,50]. After the delignification treatment, whatever it is, the wood template turns whitish. A whitish colour indicates that most of the lignin has been removed. It is not yet transparent because there is still scattering between the air that fills the pores and cellulose and hemicellulose. The process preserves the original structure of the native wood although the porosity has increased due to the removal of lignin. Fortunately, the increase in porosity is regarded as an advantage because it makes the next step, i.e., polymer impregnation, easier [10,21]. The choice of the polymer is made by trying to match the refractive index of cellulose and hemicellulose. PMMA and epoxy resin are widely used since they have a refractive index of about 1.5 [1,8,10,21,50], which is quite close to that of delignified wood. Unfortunately, they are fossil-based polymers and therefore the transparent wood that is produced cannot be considered fully bio-based. Aiming to overcome this drawback, Montanari et al. [7] have recently developed a bio-based thermoset, called PLIMA, to replace PMMA and epoxy resin. Whatever polymer is chosen, after the porous template has been infiltrated, the material is thermally treated to promote polymerization [21]. As result, transparent wood is obtained (Figure 3.1).

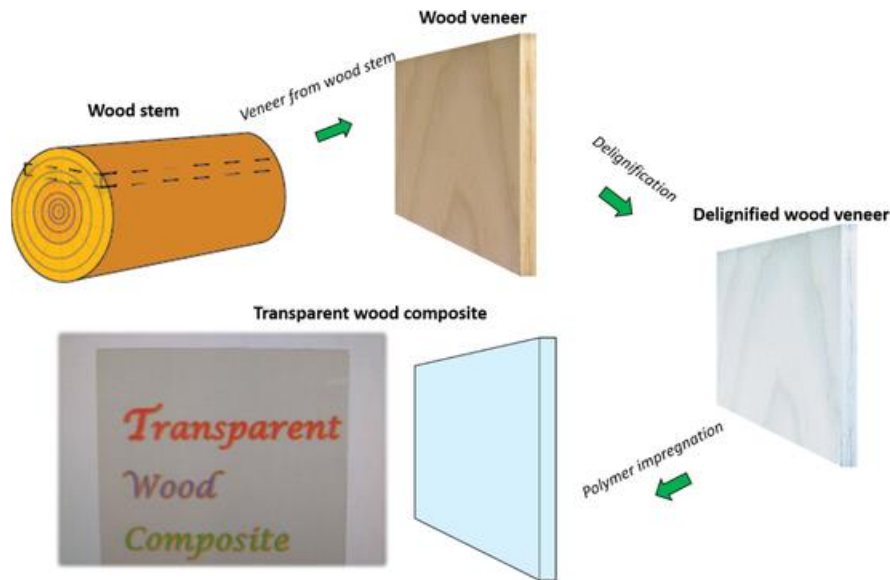


**Figure 3.1.** Steps in transparent wood production [1].

Transparent wood exhibits an optical transmittance of up to 90% in 1.2 mm thick samples, while the haze, i.e., the ratio between the diffused transmitted light and the total transmitted light, is up to 80% [7]. Moreover, other interesting features are its low thermal conductivity ( $0.15 \text{ W m}^{-1} \text{ K}^{-1}$ ) [9] and failure behaviour since it does not shatter [10,15]. All these characteristics make it an attractive alternative to soda-lime glass in applications such as energy-efficient buildings [10,23].

Unfortunately, the process is still on a lab-scale, which means it is very time-consuming and energy demanding and thus, the production is limited to small samples. Furthermore, the delignification requires a large amount of chemicals, which are often toxic to humans and the environment, and produces a liquid waste that is difficult to recycle [10,50,51]. There is also a limit to the thickness of the sample that can be produced. Indeed, using a thicker wooden template increases the delignification time and makes it more difficult the polymer infiltration. Also, by increasing the thickness, the optical transmittance is reduced because of the longer path the light has to travel and the increased fraction of interfaces [9,10,51,52]. The low cellulose content is another weakness of transparent wood; in fact, the volume fraction of cellulose is usually around 30% or less[7], otherwise the optical transmittance would drop similarly to what happens when the thickness increases [7,10]. Finally, the compatibility between the polymer and the cell wall, and the shrinkage during the polymerization are parameters that must be taken into account during the production of transparent wood [10,23]. Indeed, these two aspects have a great influence on the optical transmission of the final product since they affect the adhesion of the polymer to the wood tissue. Furthermore, adhesion plays an important role in the stress-transfer mechanism between matrix and reinforcement. The main reason for the lack of compatibility is the different nature of the two components. The polymers that are used are often hydrophobic while cellulose and hemicellulose are hydrophilic [23].

Having these issues in mind, the different research groups have come up with different solutions [50]. A promising alternative seems multilayer transparent wood [52], which is based on wood veneers instead of a single thick wood block. This approach reduces the delignification time and the cost of the process improving the scalability of the process and making its industrialization more likely.

Trying to solve the drawbacks of the delignification process, Xia et al. [51] have modified the lignin instead of removing it. Their method is based on brushing H<sub>2</sub>O<sub>2</sub> on the wood structure to modify the lignin and then exposing the template to UV radiation to remove the chromophoric groups of the lignin. Since the wood is not dipped in chemicals, the lignin modification can be performed selectively on specific areas. Moreover, the consumption of chemicals and energy decreases drastically. In contrast, the production of lignin-retaining transparent wood developed by the group at KTH uses a different approach [16]. In this case, delignification is replaced by lignin modification through alkaline H<sub>2</sub>O<sub>2</sub> treatment. This process is used in the pulp industry to produce bleached pulp. It removes only the chromophores of the lignin, retaining up to 80% of the initial lignin content. As a result, the optical properties of lignin-retaining transparent wood are similar to those of traditional TW. Alkaline H<sub>2</sub>O<sub>2</sub> treatment is faster than delignification and more environmentally friendly, which means a further step towards industrial scalability of transparent wood production. In addition, preserving the lignin improves the mechanical structure and reduces damage to the cell wall structure, extending the number of wood species that can be utilized. Indeed, wood species such as pine cannot be used to produce transparent wood if they undergo a traditional delignification step because they become too brittle after the treatment.

As said before, it is challenging to produce thick transparent wood that can maintain high transparency, thus transparent wood has usually a thickness of a few millimetres. For this reason, Li et al. [23] have tried to produce thicker TW by acetylating the delignified wood template. After acetylation, the compatibility with the polymer increases because the acetate groups reduce the hydrophilic nature of the cell wall, improving the interface between the two components. This makes it possible to manufacture centimetre thick transparent wood biocomposites.

### *3.2 Mechanical properties of transparent wood biocomposites*

Transparent wood, similarly to native wood, is not an isotropic material and this is reflected in its mechanical properties [10]. In addition, the mechanical properties strongly depend on the wood volume fraction [21]. Zhu et al. [8] pointed out that TW with fiber orientation parallel to the load shows values of elastic modulus and tensile strength twice as great as those of transparent wood with fibers perpendicular to the load direction. Moreover, the mechanical properties along the fiber direction are better than both the neat polymer and the delignified template, suggesting that, although not perfect adhesion, there are synergistic reinforcement mechanisms between wood and the polymer matrix [10]. On the other hand, along the weak direction, Jungstedt et al. [1] found that the tensile strength and strain to failure of delignified-birch/PMMA transparent wood are better than native birch but worse than neat PMMA and that the biocomposite shows a brittle failure along this direction.

Since transparent wood is seen as a promising substitute for soda-lime glass in building applications, the mechanical performance of the two materials was compared in 2017 [16]. As a result, the tests showed similar fracture stresses for LT transparent wood and glass but with a higher strain to failure for TW (about 2.18% instead of 0.19% for glass). Furthermore, although the researchers have considered transparent wood as an ideal brittle material, its fracture toughness along the strong direction was greater than that of glass while they were similar when studying the weak direction [15]. Transparent wood can also replace glass fiber polymer composites in load-bearing applications because they show similar specific elastic modulus and tensile strength, with the advantage that TW is more convenient from an environmental point of view [1].



## 4. Materials and Methodology

### 4.1 Samples

Nine specimens were prepared for each material analysed. Native birch wood (3 mm thick,  $\rho=772 \text{ kg/m}^3$ ) and birch veneers had been purchased from Calexico Wood AB. Both were flat sawn in order to obtain the grain direction parallel to the surface. Transparent wood was manufactured in the department's laboratory instead.

#### 4.1.1 Multilayer transparent wood synthesis

The production of TW was performed following a well-established process [1,6,10] that took place entirely under a fume hood for safety reasons.

The veneers of birch (0.5 mm thick) were cut into smaller pieces ( $100 \times 100 \text{ mm}^2$ ). Twelve pieces were cut. Indeed, the delignification makes the wood veneers very fragile since lignin acted as a binder between the cells [53], and thus, some of the specimens might break. For this reason, several samples are usually prepared to ensure the success of the process.

The delignification was carried out according to the  $\text{NaClO}_2$  method. This process removes lignin making it more water-soluble [16]. After the treatment, the lignin content in birch veneers decreases from 20% to about 3% [1]. First, the veneers were dipped in a beaker containing an acetate buffer solution ( $\text{pH}=4.6$ ) to which 1,25 wt%  $\text{NaClO}_2$  (Sigma-Aldrich) was added. They were left in the solution for 6 h at  $75^\circ\text{C}$  until they turned whitish, as shown in Figure 4.1. Then, they were washed under vacuum with deionized water three times. The following step was dehydration using ethanol and then acetone (three times, under vacuum). The use of ethanol, before acetone, makes it possible to reduce the shrinkage and thus better preserve the wood structure, while acetone helps the infiltration by the polymer [1].

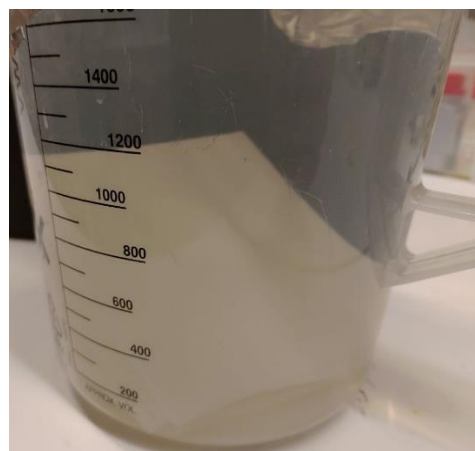


**Figure 4.1.** Delignified veneers.

Indeed, the next step was polymer impregnation. In this project, polymethyl methacrylate (PMMA) was chosen as polymer matrix. PMMA is a synthetic amorphous thermoplastic polymer belonging to the acrylate group. It was discovered in the 1930s. Often referred to as organic glass, in contrast to inorganic (silica) glass, thanks to its excellent transparency,

it is commonly known by its trade name Plexiglas [54–56]. Polymethyl methacrylate is produced by polymerization of the monomer methyl methacrylate (MMA) [54–58]. The structure of MMA and the repeating unit of PMMA are shown in Figure 4.2.

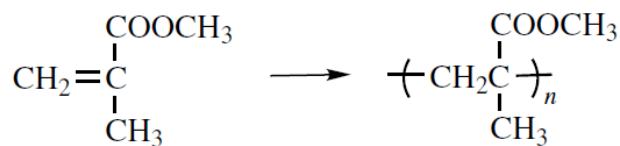


**Figure 4.2.** Methyl methacrylate (on the left) and repeating unit of PMMA (on the right) [58].

Liquid methyl methacrylate (Aldrich) was passed through  $\text{Al}_2\text{O}_3$  powder in order to remove the inhibitor and finally collected in a round-bottom flask. 0.3 wt% of initiator 2,2'-azobis (2-methyl-propionitrile) (Sigma-Aldrich) was added to MMA and then the monomer was pre-polymerized at 75°C for 10-15 minutes, during the process gases were released. After that, the flask was placed in an ice bath to stop polymerization.

The delignified veneers were immersed in the pre-polymer bath for the vacuum infiltration (overnight). After being infiltrated, the templates were packed between two glass slides making sure that they were oriented the same way, and finally wrapped with aluminium foil. In this case, the multilayer transparent wood was produced using 4 veneers to have a final thickness of approximately 3 mm, therefore comparable with that of the native birch board.

Next, they were put in the oven at 35°C for 3h, then the temperature was increased and maintained at 45°C for another 3h, after which the temperature was set at 70°C overnight. Some weights were used during the heat treatment to make sure to get a flat sample. When the specimen was removed from the oven, the weights were held until the sample reached room temperature.

After becoming cold enough to be handled safely, the aluminium foil and the glass slides were removed, and the transparent wood was obtained (see Figure 4.3).

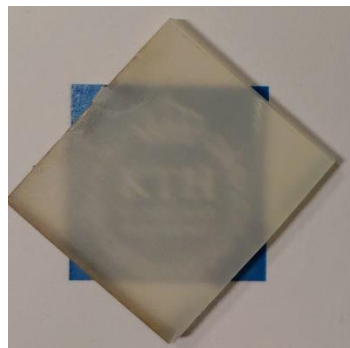


**Figure 4.3.** Multilayer transparent wood.

#### 4.1.2 Sample preparation

For the four-point bending test, the specimens, shown in Figure 4.4, were cut into the size of  $70 \times 5 \times 3 \text{ mm}^3$  with a portable scroll saw (Dremel, Moto-Saw MS20-15). They were cut so that the fibers arranged parallel to the short side of the sample.

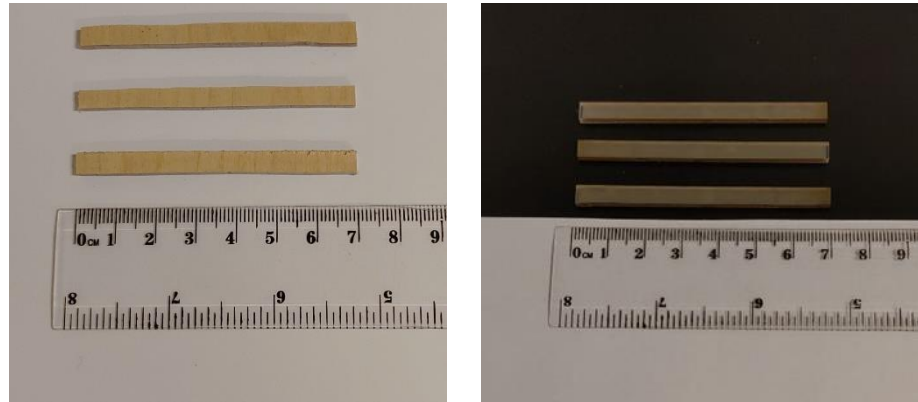


**Figure 4.4.** Native wood (on the left) and transparent wood samples (on the right).

The in situ single-edge-notched four-point bending specimens for both materials were produced by laser cutting to have more control and precision in the geometry. Here, the sample size was  $30 \times 3 \times 3 \text{ mm}^3$  with an initial notch of 1 mm made in such a way that its propagation took place in the TR system. Then, the crack was manually sharped by a razor blade. The laser cutting was necessary to highlight the microstructure of the materials in order to understand the fracture mechanisms at the scanning electron microscope, especially for the native wood (NW) as shown in Figure 4.5, where two specimens, one obtained from laser cutting and the other from sawing, are compared.

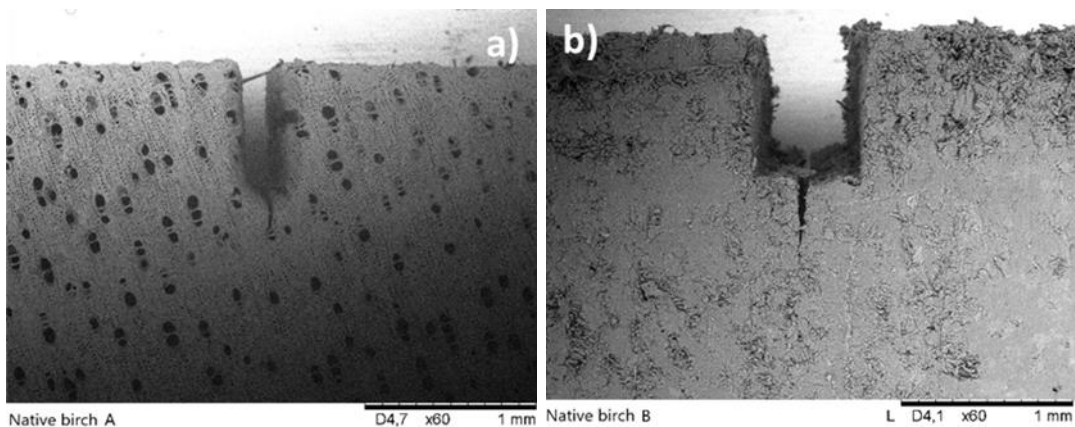


**Figure 4.5.** Native wood cut by laser (a) and cut by saw (b).

The DIC samples were cut by saw instead, with the same sample size and an initial notch of 1 mm in the TR system manually sharped with a razor blade. The speckle pattern was created by spraying ink on the specimens (see Figure 4.6).



**Figure 4.6.** Deposition of the black ink on the sample with an air mini paint spray gun.

After a few trials, two inks, one white and one black, were chosen to ensure a pattern that could be suitable for the DIC measurements (see Figure 4.7).

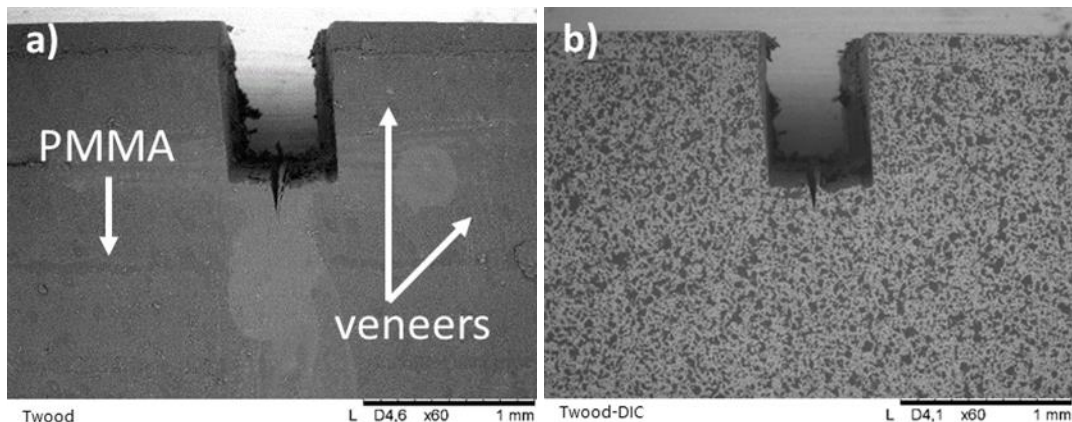


**Figure 4.7.** Transparent wood (a) before and (b) after speckle deposition.

## 4.2 Characterization

### 4.2.1 Wood cell wall volume fraction

The volume fraction of wood cell wall of the two materials was calculated. For transparent wood, the volume fraction was obtained as follows [21]:

$$V_f = \frac{W_f \rho_c}{\rho_f} \quad (3)$$

Where  $W_f$  is the cellulose weight fraction (0.28) and  $\rho_f$  is the density of the cellulose (1500 kg/m<sup>3</sup>) [21]. The weight fraction was measured by dividing the weight of the delignified wood template by the total weight. On the other hand,  $\rho_c$  is the density of the composite (1259 kg/m<sup>3</sup>). The density of the composite was calculated by weighing it and measuring its volume.

The volume fraction in native wood is equal to its relative density, which is calculated as [1]:

$$V_f = \frac{\rho}{\rho_f} \quad (4)$$

Where  $\rho$  is the density of native wood. It assumed that the density of the cell wall ( $\rho_f$ ) is equal to that of cellulose.

#### 4.2.2 Optical microscopy

An optical microscope (Leica M205 FA) connected to a digital camera (Hamamatsu C11440) was used to look at the cross-section of the samples and acquire images of it.

Also, a light stereomicroscope (Nissho Seimitsu Kogaku SS) was used to ensure the cracks generated in the samples met the requirements for the *in situ* single-edge-notched four-point bending tests.

#### 4.2.3 Scanning electron microscopy

Scanning electron microscope (SEM) is a powerful tool that allows investigating not only the surface topography of the materials but also their composition and crystal structure [59,60]. Instead of using visible light to look at the sample as in a common optical microscope, SEM imaging is based on electrons.

In this work, a tabletop SEM (Hitachi TM-1000), shown in Figure 4.8, was used to carry out the characterization of the samples and *in situ* mechanical tests. The advantage of using this instrument, which is a low-vacuum SEM, is there is no need to coat the samples and therefore the crack growth can be followed without worrying about possible problems due to charging up [61]. Also, the images were captured in back-scattered electron (BSE) imaging mode, which reduced brightness changes during the experiment compared to using secondary electron (SE) mode [62].



**Figure 4.8.** Hitachi TM-1000 Tabletop scanning electron microscope [63].

#### 4.2.4 Four-point bending test

Before calculating the fracture toughness, it is necessary to measure the Young's modulus in the transverse direction,  $E_T$ . It was decided to obtain the elastic modulus employing a

four-point bending test to be consistent with the in-situ measurements. Unlike three-point bending [64], this test reduces shear effects on the sample (which otherwise would lead to an underestimation of Young's modulus). A further property, transverse flexural strength, was measured during this test. The testing equipment consisted of an Instron 5566 Universal Testing Machine with a load cell of 500 N (shown in Figure 4.9).

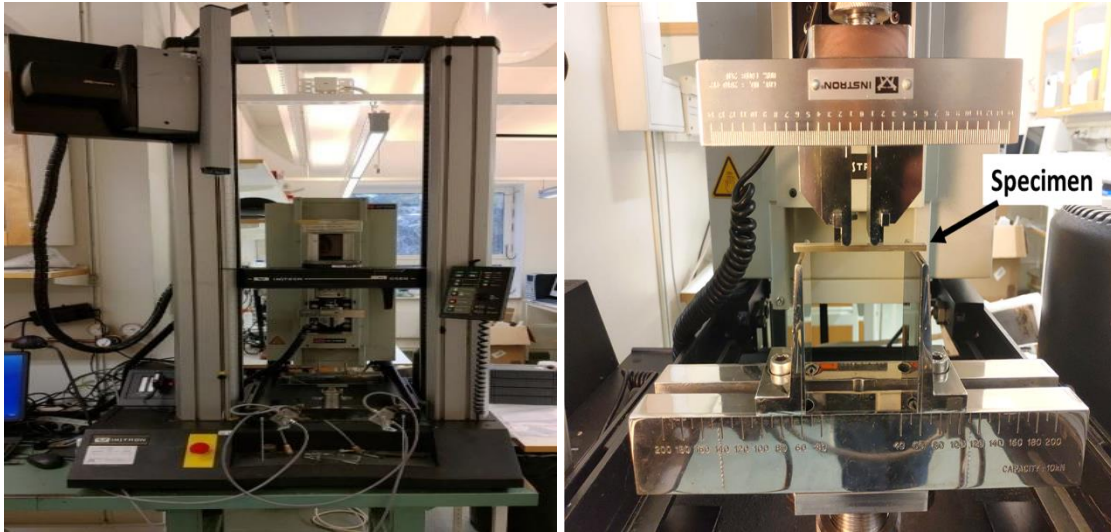


**Figure 4.9.** Instron 5566 Universal Testing Machine.

The setup was chosen based on the ISO 8375:2017 standard, the beam theory, and the in-situ test [65,66]. In this case, the support span was 60 mm and the load span 14 mm, thus maintaining the same ratio used in the in-situ experiments. The testing machine was set in displacement control mode with a speed of 0.1mm/min. The velocity was chosen the same as that used in the in-situ measurements in order to avoid the influence of the viscoelastic effect on the results. The tests were carried out in an environment-controlled room (22°C and relative humidity of 50%). Figure 4.10 schematically shows the test setup.

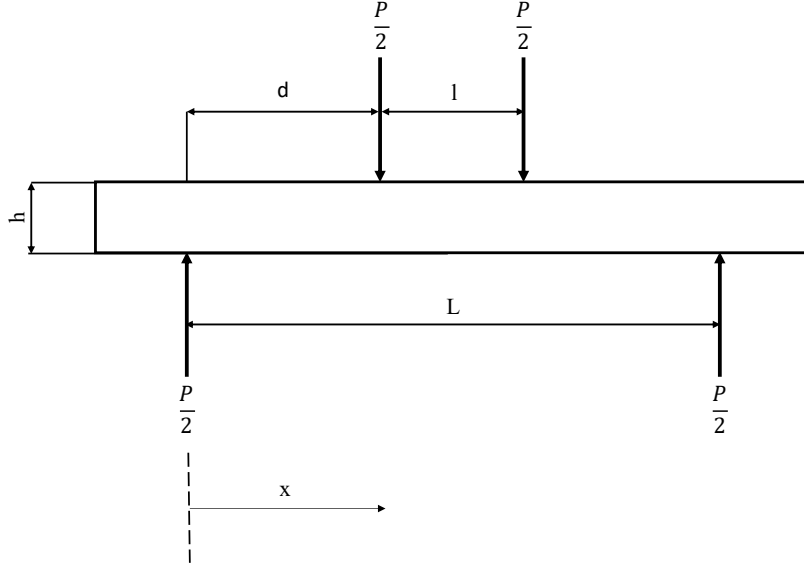


**Figure 4.10.** Sketch of the four-point bending test.

The elastic modulus can be obtained from the four-point bending test using the following formula [66]:

$$E = d[3Lx - 3x^2 - d^2] \frac{dP}{dw} \quad (5)$$

Where  $d$  is the distance between the support point and the closest loading point,  $L$  is the support span,  $x$  is the distance at which the deflection is measured, with respect to a fixed origin (i.e., the left support). The slope  $\frac{dP}{dw}$  is calculated from the initial part of the load-deflection curves. The range was set 10% and 50% of the maximum load as lower and upper limits of the elastic part respectively. The second moment of inertia is calculated as:

$$I = \frac{bh^3}{12} \quad (6)$$

Where  $b$  is the sample width and  $h$  is its thickness.

In this case, the deflection was measured by the position of the crosshead of the machine so  $x=d$ , and therefore the equation becomes:

$$E_T = \frac{d^2[3L - 4d]}{bh^3} \frac{dP}{dw} \quad (7)$$

Also, the flexural strength of the materials in the transverse direction was calculated using the formula [67]:

$$\sigma_T = \frac{3P_c(L - l)}{2bh^2} \quad (8)$$

Where  $l$  is the load span.

#### 4.2.5 Single-edge-notched four-point bending test

The advantage of in situ experiments is that the failure mechanisms can be observed in real-time, rather than inferred from test results as in macroscopic experiments, providing additional insights into that material [68]. The in situ four-point bending tests were performed in a Deben Microtest 200N tester equipped with a 50N load cell. The in situ equipment was located inside the specimen chamber of the tabletop SEM and then, the sample was inserted, making sure it was centred with respect to the loading points (see Figure 4.11).

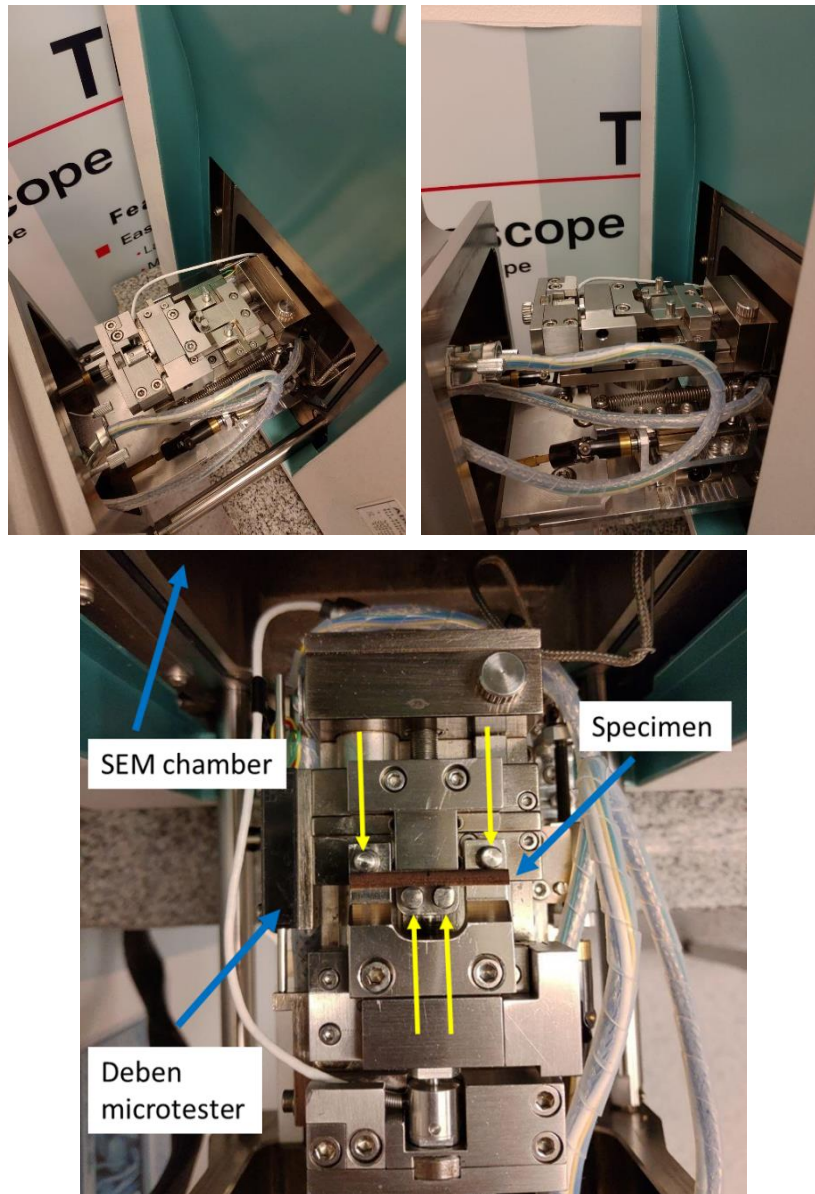


**Figure 4.11.** Deben Microtest inside the specimen chamber.

The support span was 23 mm while the load span was 5.5 mm. The deflection rate was 0.1mm/min. A sketch of the test setup is shown in Figure 4.12. The ImageJ software was used to measure the length of the crack at different stages of the in-situ four-point bending test.

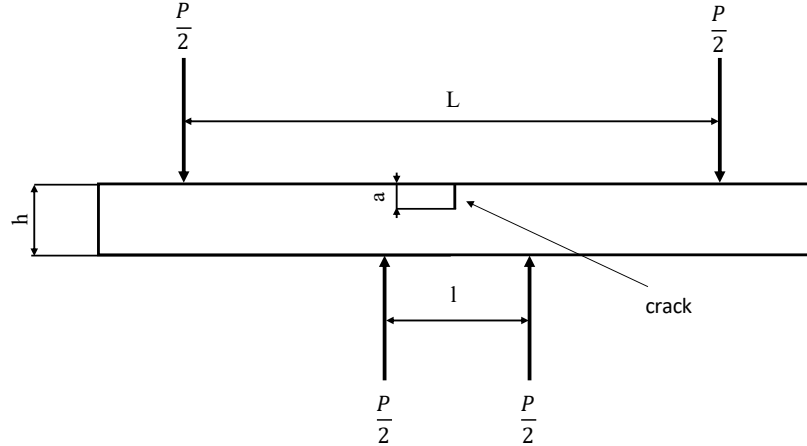


**Figure 4.12.** Representation of the in situ single-edge-notched four-point bending.

Due to the small sample size, the fracture toughness along the TR system was studied using an approach based on nonlinear elastic fracture mechanics as suggested by Tukiainen [3]. Therefore, the J-integral was calculated using the following equation [17,45]:

$$J_{Ic} = \frac{2U(P_c)}{(h-a)b} \quad (9)$$

$U(P_c)$  is the area under the curve load vs loading-line deflection at the critical load,  $h$  is the thickness of the sample,  $a$  is the length of the crack and  $b$  is the specimen width.

It was decided to express the fracture toughness in Mode I in terms of stress-intensity factor to make it possible to compare the results with the data in the literature. Therefore, the equivalent critical stress intensity factor  $K_{Ic}$  was obtained as follows [17,69]:

$$K_{Ic} = (J_{Ic}E_T(1 - v_{TR}^2))^{1/2} \quad (10)$$

For simplicity,  $K_{Ic}$  will be referred to as  $K_I$  from now on.

$E_T$  is the transverse elastic modulus and  $v_{TR}$  is the Poisson's ratio for TR system. For transparent wood, as a first approximation,  $v_{TR}$  was calculated using the rule of mixture [70]:

$$v_{TR} = v_w V_w + v_{\text{PMMA}}(1 - V_w) \quad (11)$$

$v_w$  and  $v_{\text{PMMA}}$  are the Poisson's ratios of the delignified wood and PMMA, respectively. As a simplification, the Poisson's ratio of delignified wood was assumed to be the same as that of native wood, which is 0.38 for birch in TR system [3]. For PMMA,  $v$  was taken equal to 0.35 [1].  $V_w$  is the volume fraction of delignified wood.

#### 4.2.6 Digital Image Correlation (DIC)

This non-contact optical method for measuring surface deformations was invented in the 1980s [71]. Since then, different DIC techniques have been developed [72], including two-dimensional (2D) digital image correlation, which was the method used in this project. DIC consists in taking images of the surface of the sample during the test and, through specific algorithms, elaborating these images in order to obtain the displacement and the strain field of the material. However, to do this, the surface must have specific features that can be used during post-processing. Sometimes, the natural texture of the material is enough, otherwise, ink can be sprayed to create an artificial speckle pattern [71,72]. Based on the information provided by digital image correlation, different material properties can be obtained such as the Young's modulus. This technique does not require expensive or complex equipment since even common digital cameras can be used. Furthermore, unlike other optical methods, there are no strict testing requirements regarding the conditions of the environment in which the experiment is carried out [71–73].

In this work of thesis, DIC was coupled with SEM images to study the strain field of native birch and d-birch/PMMA transparent wood during the in situ single-edge-notched four-point bending tests. Before the crack propagation, approximately every 0.25 N, the test was stopped to allow the image to be acquired. After the crack started propagating, images were recorded according to the crack behaviour. At least 13 images were taken for each specimen in order to follow the crack growth as closely as possible. The strain field was evaluated by using the software VIC-2D. The subset size was 35x35 pixels.

The strain field,  $\varepsilon_T$ , was expected to be predominant since the samples were tested by means of four-point bending tests (pure bending moment). However, the strains  $\varepsilon_{TR}$  and  $\varepsilon_{RR}$  were non-null because of the inhomogeneity of the material. The analysis of  $\varepsilon_T$  provided information about the fracture process zone ahead of the crack tip. Moreover,  $\varepsilon_{TR}$  was studied to check if delamination occurred during the test (particularly important for this kind of transparent wood biocomposite).

#### 4.2.7 Cohesive law measurements

The SEM images taken for the DIC analysis were also used to obtain the cohesive law, for both materials, according to equation 2. For each specimen tested, the J-integral was calculated from equation 8, before and after the onset of crack propagation. Then using the software MATLAB®, the J vs  $\delta$  data were plotted and fitted. The curve obtained was derived in order to get the stress vs end-opening curve.

#### 4.2.8 Material selection

It was demonstrated that a preliminary material selection can be done by using the material parameters obtained in this work of thesis. The software Ansys Granta EduPack was used

to do this as it implements the criteria elaborated by Ashby et al. for material selection [74,75].



## 5. Results and Discussion

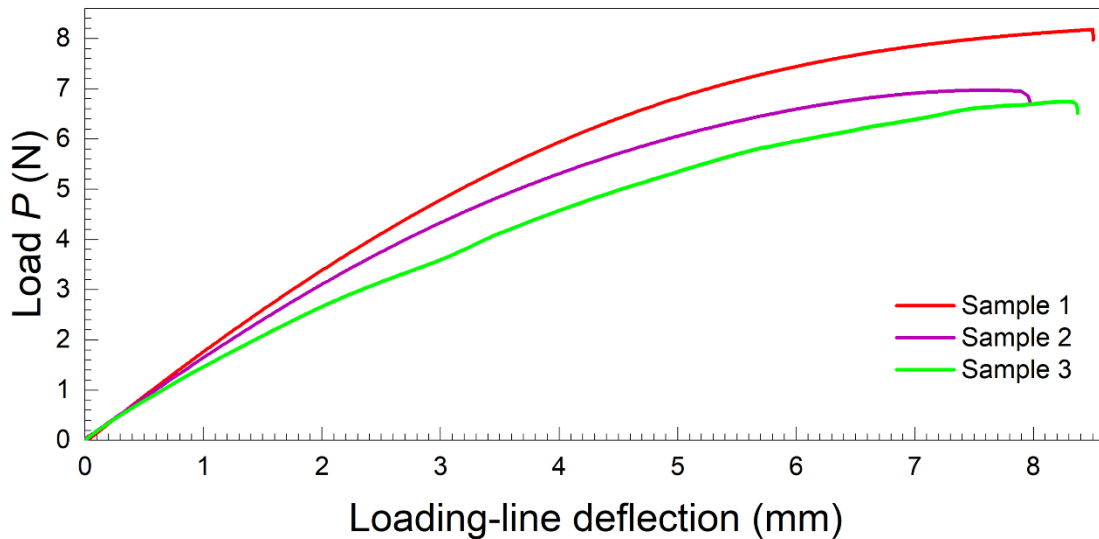
The Results and Discussion section is organized as follows: first, the results obtained from the macroscopic four-point bending test are introduced. Then, the fracture toughness and the observed mechanisms of fracture are presented. The following subsection covers the insights provided by 2D-DIC analysis. Next, the results from the application of the cohesive law model are discussed. Finally, a demonstration is given of how the obtained parameters can be used for material design.

### 5.1 Elastic modulus and flexural strength along the weak direction

Three specimens for each material analysed were tested by means of a four-point bending test. Figure 5.1 reports the curves obtained for native wood and transparent wood, respectively. It can be noticed the deflection before failure is much larger for native birch (about 8 mm on average) compared to that delignified birch/PMMA biocomposite (about 1.3 mm on average). Similar behaviour was observed by Jungstedt et. al [1] during tensile testing along the same direction. As reported in the literature [1,4], cell wall bending is very likely to occur when native wood is subjected to tension or compression in the transverse direction. On the other hand, in transparent wood, PMMA fills the cell lumen preventing the cell wall deformation and making the fracture more brittle. Indeed, the shape of the curve of TW is that typical of an ideal elastic material while native birch exhibits a certain degree of nonlinear deformation.

a)

**Native birch**



b)

## D-birch/PMMA transparent wood

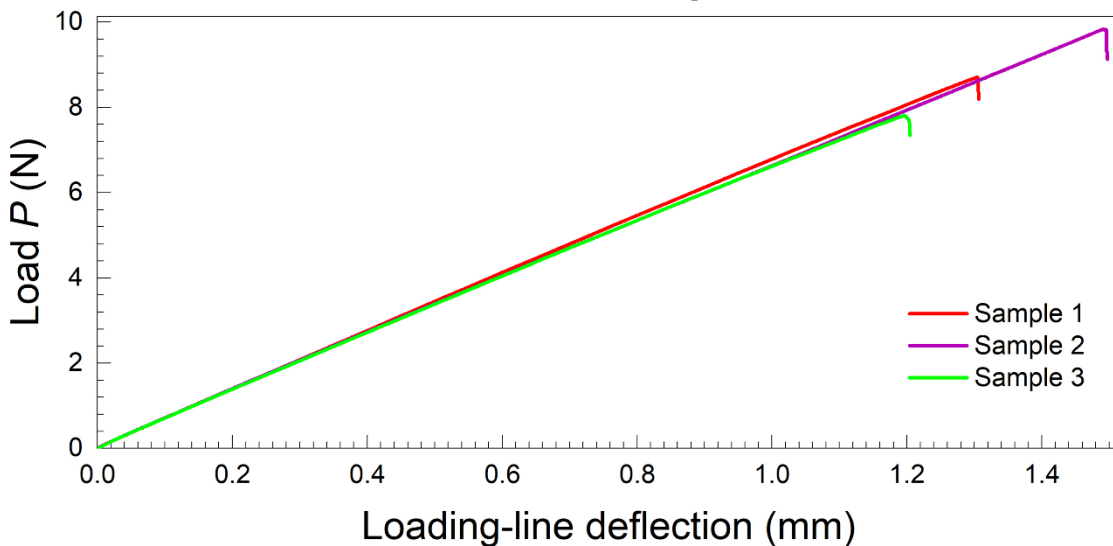


**Figure 5.1.** Four-point bending curves. (a) native wood (b) transparent wood

As mentioned before, equations 7 and 8 were exploited to calculate the transverse Young's modulus and the transverse flexural strength of native birch and TW. The values obtained, plus those of PMMA, are reported in Table 5.1 together with the volume cellulose content and the Poisson's ratio. The Young's modulus of transparent wood was very consistent, as the measurements differed by only a few MPa from each other, so no standard deviation was reported for this parameter.

**Table 5.1** Mechanical properties of NW, PMMA, and TW.

Properties	Native wood	PMMA [1,2]	Transparent wood
$E_T$ (GPa)	$0.5 \pm 0.1$	2.4	3.3
$\sigma_T$ (MPa)	$11.6 \pm 0.8$	117.9	$17.2 \pm 2$
$V_f$ (%)	0.51	/	0.23
$v_{TR}$	0.38 [3]	0.35	0.36

The measured elastic moduli are consistent with those reported by Jungstedt et al. [1]. They measured  $E_T \approx 0.5$  GPa for birch and  $E_T \approx 3.4$  GPa for delignified birch/PMMA transparent wood. If the transverse Young's modulus of biocomposite is compared to those of its constituents, it can be observed that its value is higher than the sum of those of its components. The reason behind it, again, can be the suppression of cell wall bending by the polymer, as has also been suggested in the literature[1]. Improving the stiffness along the weak direction is a desirable result for a material intended for use in load-bearing applications.

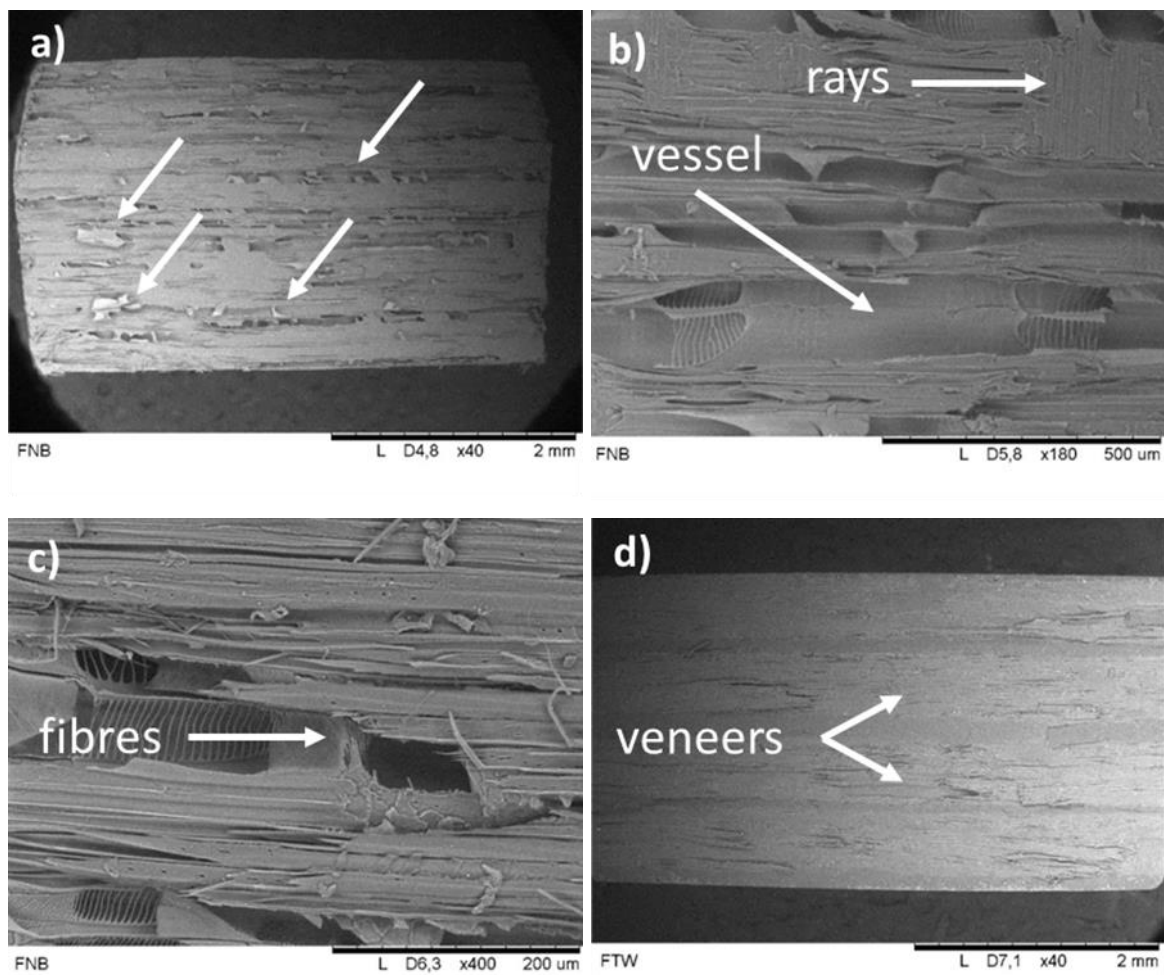
However, looking at the transverse flexural strength, the improvement compared to native wood is very marginal. An explanation for this might be a poor adhesion between PMMA and the delignified cell wall, which produces their detachment during the test, preventing an efficient stress distribution. Adhesion problems are often, as mentioned in Chapter 3, one of the side effects in chosen PMMA as matrix.

### 5.1.1. Fracture surfaces

After the four-point bending tests, a post-mortem analysis was performed on the tested specimens. The fracture surfaces studied correspond to the RL plane of the sample. The study was carried out using the tabletop SEM.

The images of the fracture surface of native birch, labelled as “FNB”, are shown in Figures 5.2 (a), (b), and (c). From the overview of the surface (see Fig. 5.2 (a)), cell wall breaking of the vessels can be clearly seen as pointed by the arrows. This is confirmed by Fig. 5.2 (b), where the inside of a vessel can be observed (bottom part of the image). In addition, in this image, the rays can be spotted in the upper right-hand corner. This indicates that the fracture could be initiated along the ray parenchyma. Finally, Fig. 5.2 (c) shows some broken fibres.

Figs. 5.2 (d)-(f), indicated as “FTW”, show the fracture surface of transparent wood, instead. Looking at Figure 5.2 (d), the layer structure of the material can be easily recognized, and the four veneers can be distinguished from the PMMA since, on their surface, the fibrous structure is evident. Figure 5.2 (e) allows some considerations to be made about the infiltration, which looks good overall. However, when looking at the sample much closer, some gaps between the fibers can be detected, for example in Figure 5.2 (f). The images also show some broken ray cells, suggesting that even in transparent wood the fracture may have developed along the ray cells.



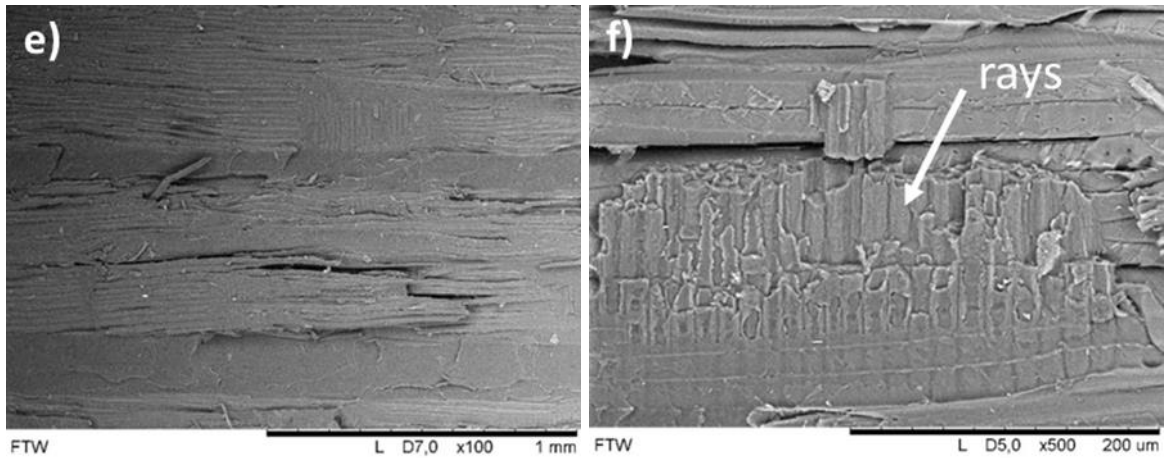
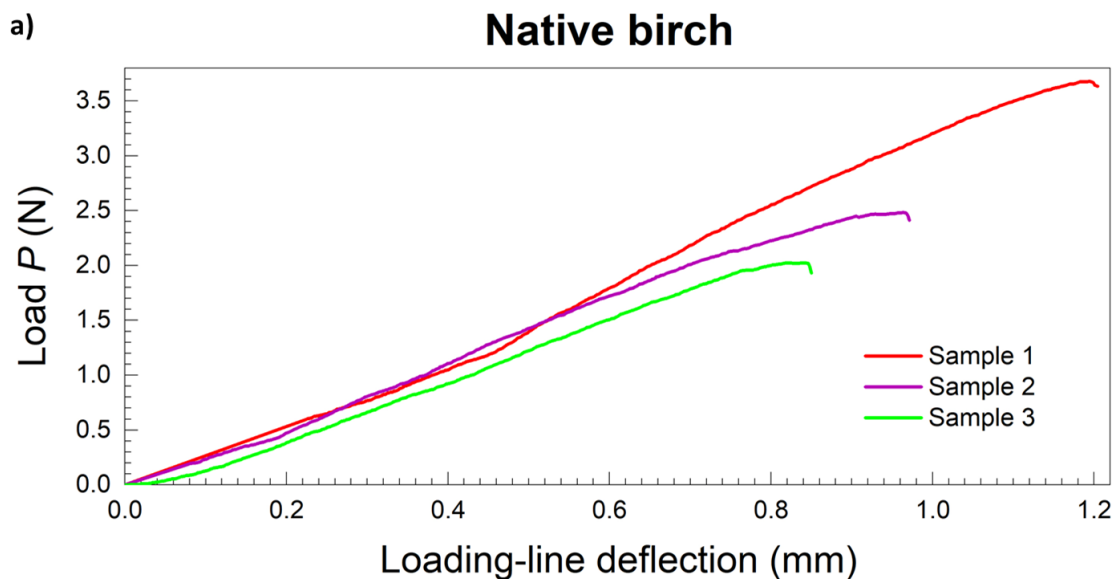


**Figure 5.2.** Fracture surfaces of sample evaluated by means of four-point bending test. (a)-(c) native wood and (d)-(f) transparent wood.

### 5.2 Fracture toughness along the TR system

The data resulting from the single-edge notched four-point bending test are reported in Figure 5.3. Similar to the previous test, the native wood exhibits on average a larger deflection compared to the biocomposite, although the difference is smaller than in the four-point bending test. Both materials present a certain degree of nonlinear deformation, but the linear part is still dominant.



b)

## D-birch/PMMA transparent wood

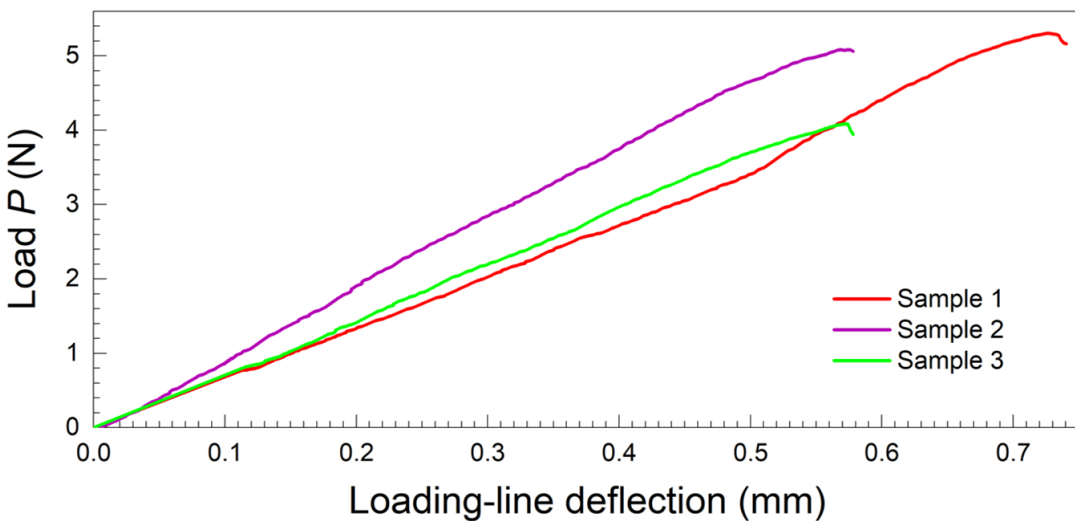


**Figure 5.3.** Single edge notched four-point bending curves. (a) native wood (b) transparent wood.

Figure 5.4 shows the fracture toughness, expressed as critical intensity factor, for the materials analysed. In addition, these results are compared to those of PMMA and glass. Looking at native birch, the value of  $K_{Ic}$  calculated ( $\approx 0.5 \text{ MPa m}^{1/2}$ ) was consistent to that reported in the literature ( $\approx 0.5 \text{ MPa m}^{1/2}$ ) [3] and to the estimation done based on equation 1 ( $\approx 0.66 \text{ MPa m}^{1/2}$ ). No data are available in the literature for the fracture toughness of transparent wood along TR direction. However, a comparison can be done with its constituents and with glass, as transparent wood is seen as a promising alternative to this material [10,23]. The improvement with respect to native wood is quite sharp, in fact,  $K_{Ic} \approx 1.3 \text{ MPa m}^{1/2}$  for D-birch/PMMA TW, which approaches the average value of neat PMMA [15,76]. Moreover, the fracture toughness of transparent wood is almost twice as large as that of soda-lime glass [15], which is the glass commonly used in the building sector. This result, combined with the fact that TW does not shatter when it breaks [10,15], may help promote the use of transparent wood in building applications in the next few years.

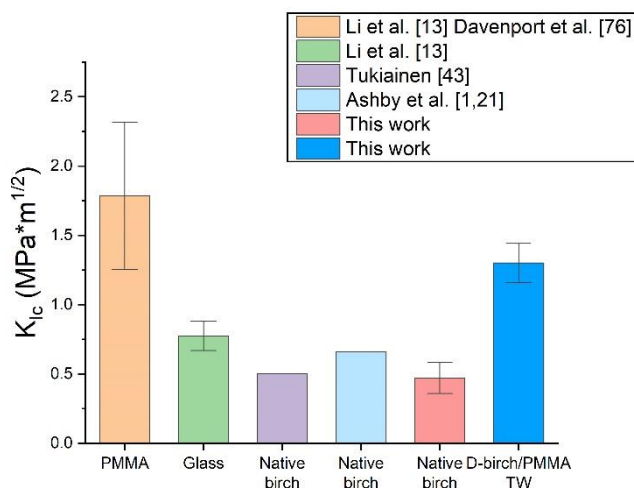
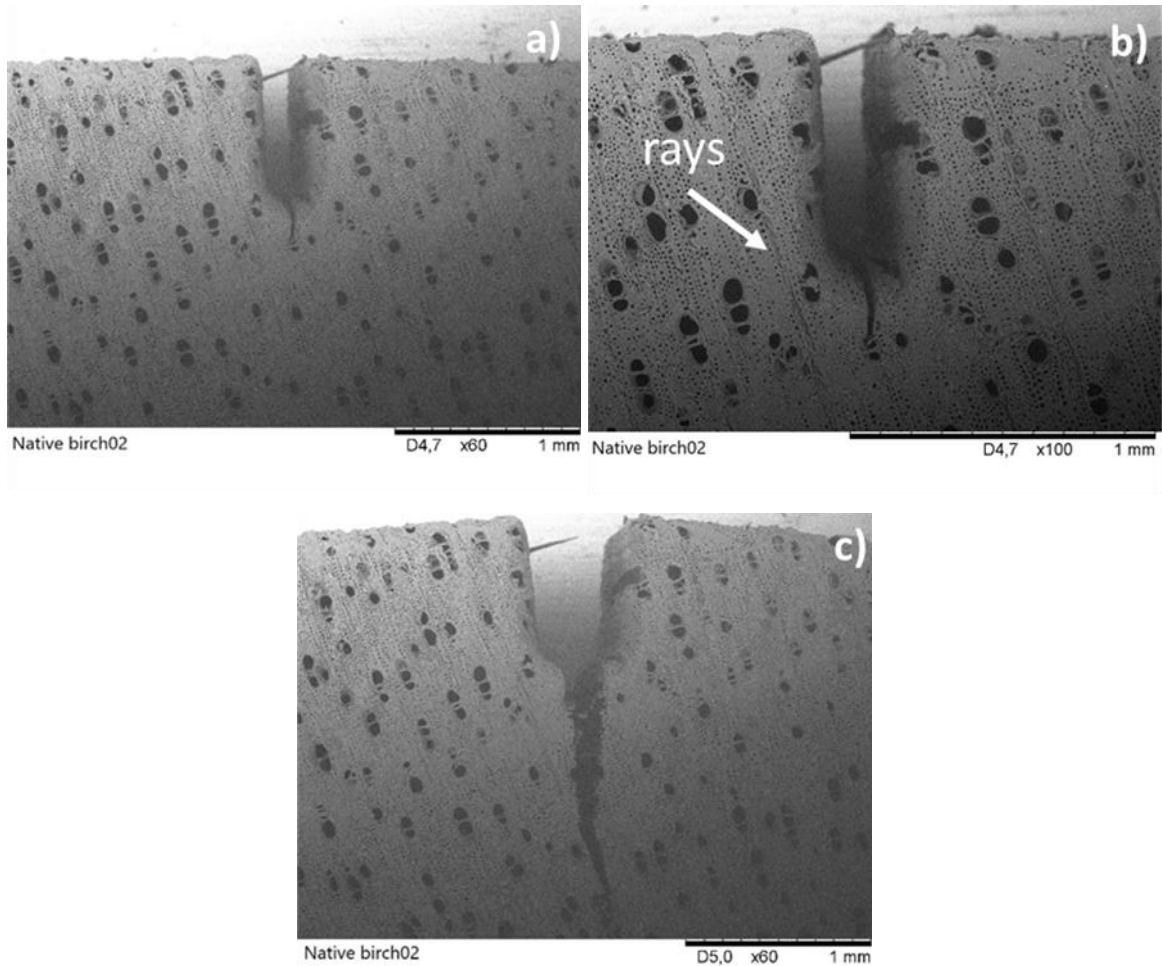


**Figure 5.4.** critical stress intensity factor bar chart.

### 5.2.1 In situ observations

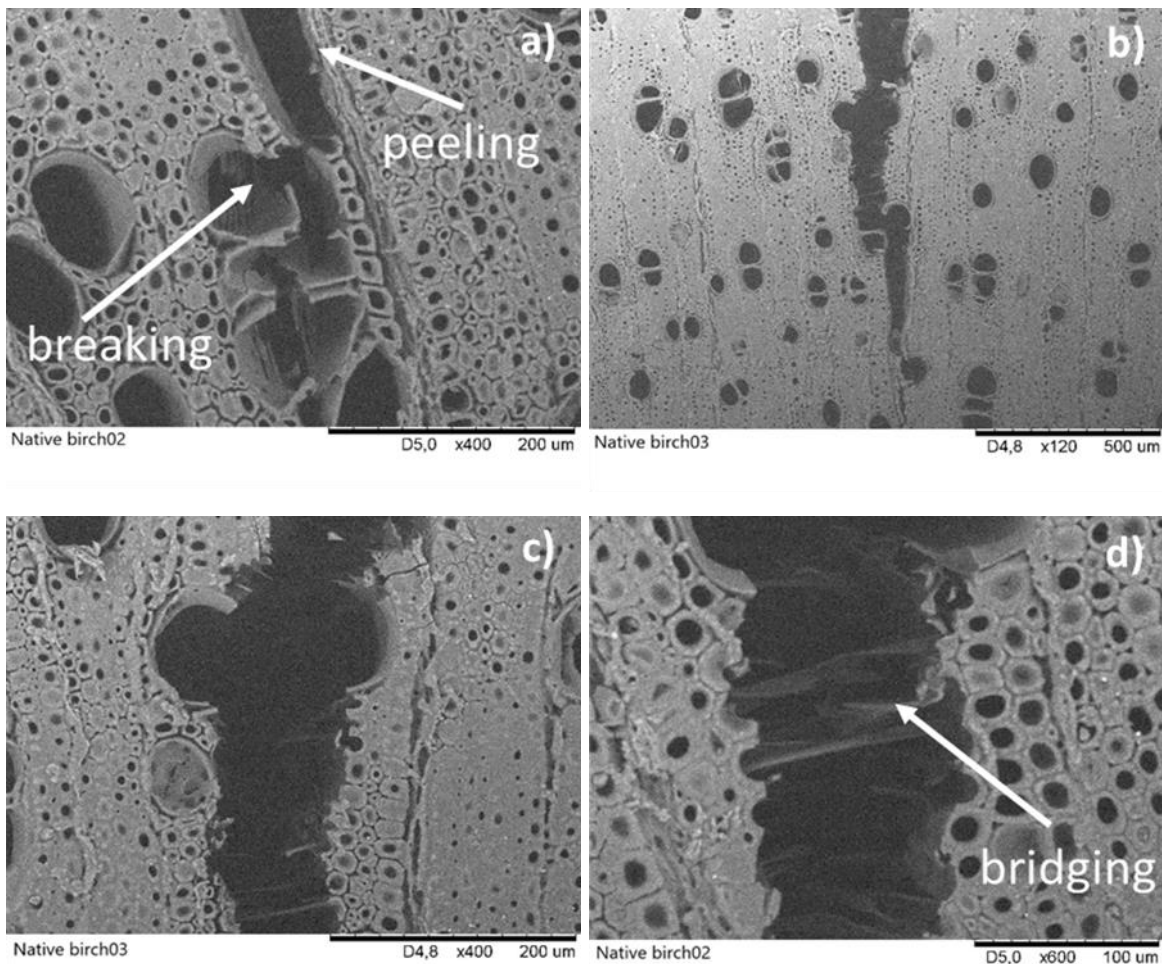
Carrying out the single-edge-notched four-point bending test inside the SEM was useful to understand how the crack propagates in the two materials.

Some of the images collected for NW are shown below. Figs. 5.5 (a) and (b) show the sample before being tested while Fig 5.5 (c) was taken at the end of the experiment. Essentially, for native birch, the crack grows seeking the rays, which are weak points in this fracture system [22], and then, once reached, tends to propagate along these cells (see Fig. 5.5 (b)).



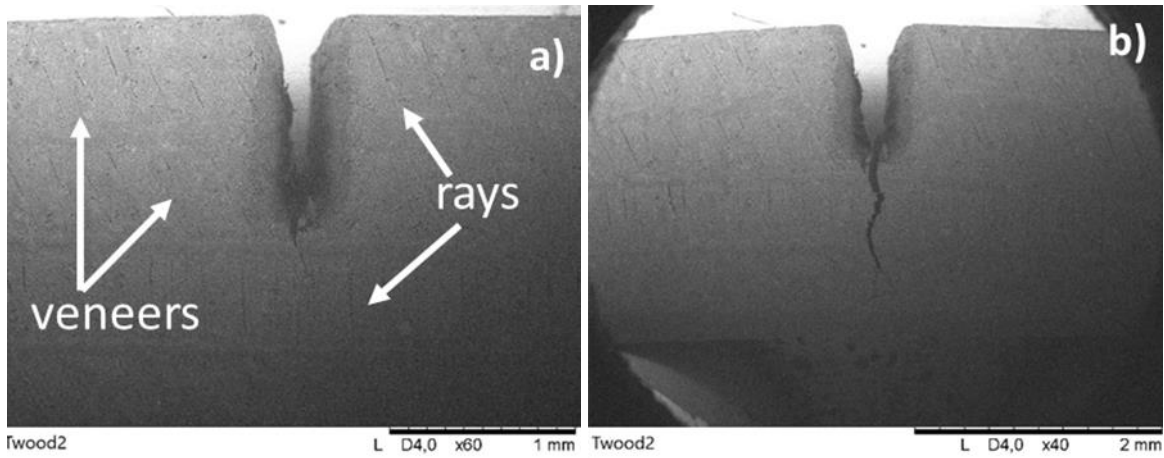
**Figure 5.5.** Native birch. (a) and (b) before and (c) after testing.

Figures 5.6 (a)-(c) demonstrate how the fracture occurs. The main fracture mechanism seems to be cell wall peeling, as expected from a crack that propagates along TR system in a high-density wood [4], however, the cell wall breaking is not negligible (mainly due to the vessels). When the mechanism is cell wall peeling, the fracture is likely to occur at the level of the primary wall or in the S1 layer [19]. In addition, fiber bridging has been observed (see Fig. 5.6 (d)), even though it is not reported in the literature [3,22], providing evidence for the use of the cohesive law. The reason why bridging has not been observed before by other authors might be because it is a local phenomenon on the microscale, which limits its detectability during macroscopic testing.



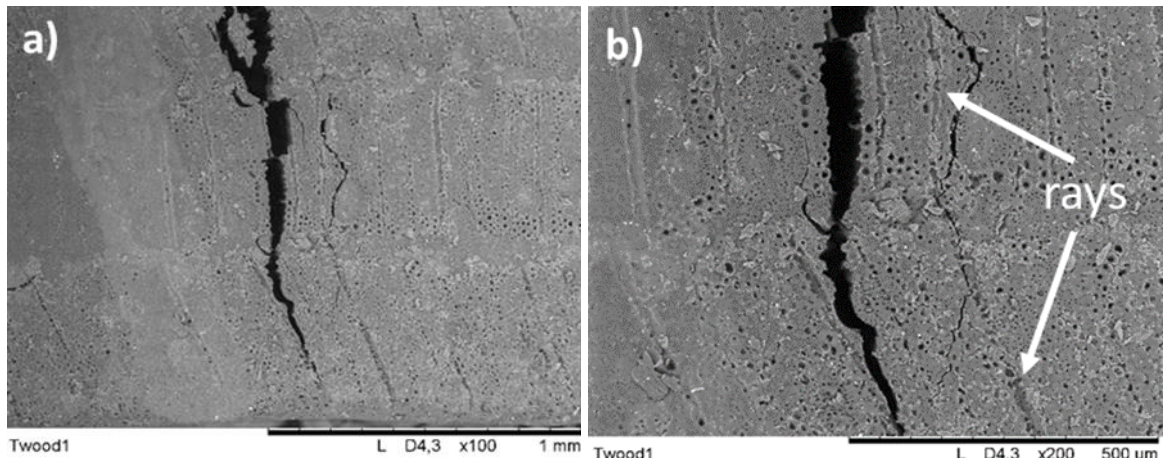
**Figure 5.6.** In situ observations of native birch. (a)-(c) cell wall peeling and cell wall breaking and (d) fiber bridging.

Looking at Figure 5.7, some considerations can be done on the fracture of delignified birch/PMMA transparent wood. Figs. 5.7 (a) and (b) show the specimen before and after testing. From these images, it can be noticed that, similar to what happens in native wood, the crack looks for propagating along the ray cells.



**Figure 5.7.** Transparent wood. (a) before and (b) after testing.

The propagation along the ray parenchyma is even more evident in Figs. 5.8 (a) and (b), where the two adjacent veneers have different ray orientations (in the upper one, the ray cells are straight while in the other, they are slightly tilted). Indeed, in this case, the crack started growing straight and then deviated in order to propagate along the ray parenchyma of the next veneer. No delamination between the layers has been observed, which means the lamination process does not seem to introduce any weaknesses into the material. Cell wall peeling can be recognized in Figs. 5.8 (c) and (d). Unlike the native wood, the cell wall separation in TW might happen at the level of middle compound lamella where the detachment at the interface between the cell wall and PMMA can occur. Indeed, the middle compound lamella is filled with PMMA because of the porosity created during the delignification [21] (remember this structure is the lignin richest region of the cell wall [32]). Detachment can be seen in Fig. 5.8 (e), where the crack broke the cell wall of a vessel and then propagated along the interface between the polymer and the inner cell wall. Finally, Fig. 5.8 (f) shows that bridging also occurs during the fracture of transparent wood biocomposites. It is worth noting that, besides the main crack, many small cracks have been developed in the samples (Fig 5.8 (c)). The small pores that can be seen in all the images as well as the porosity in the center of the cells in Figure 5.8 (d) are due to the laser cutting. They do not affect the mechanical properties as they are only superficial.



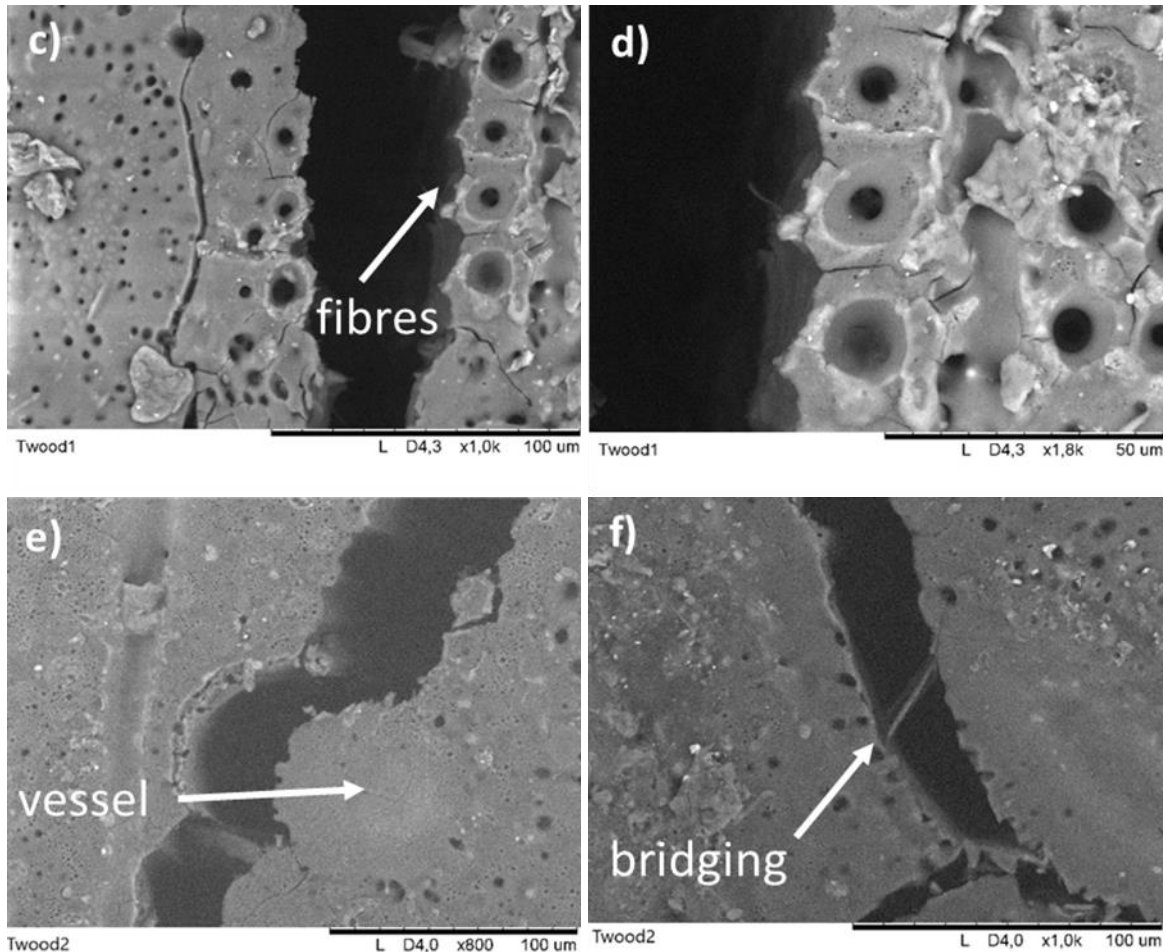


**Figure 5.8.** In situ observation of transparent wood. (a)-(b) crack propagation, (c)-(d) cell wall separation and detachment, (e) crack propagated through a vessel, and (f) bridging.

### 5.2.2 Fracture surfaces

As done for the samples after the four-point bending test, one tested specimen from each material was selected to observe its fracture surface with the scanning electron microscope. Figure 5.9 shows the fractographies acquired, where the label “FinsituNB” indicates those of native wood while the images named “FinsituTW” are the fracture surface of transparent wood.

Fig. 5.9 (a) shows an overview of the fracture surface of native birch where the area cut by laser (smoother, S) can be distinguished from that where the fracture occurred (rougher, R). Some details of the fracture surfaces, i.e., the broken cell walls of vessels and the ray cells are displayed in Fig. 5.9 (b). During the inspection, some broken fibers were observed (see Fig. 5.9 (c)).

In the case of delignified birch/ PMMA transparent wood, Fig. 5.9 (d) makes it possible to clearly differentiate the zone cut by laser (upper part of the image, S) and that where the crack has propagated (lower part, R). In the latter, no effects due to the laser cut can be seen, confirming that the laser only removed the superface layer of PMMA. Unlike what happens for the fractographies from the previous test, it is hard to distinguish the original layer structure of the biocomposite (see Figs. 5.9 (d)-(f)). In Fig. 5.9 (f), some broken ray cells

can be spotted, which sustain the hypothesis that the fracture propagates similarly in transparent wood and in native wood.

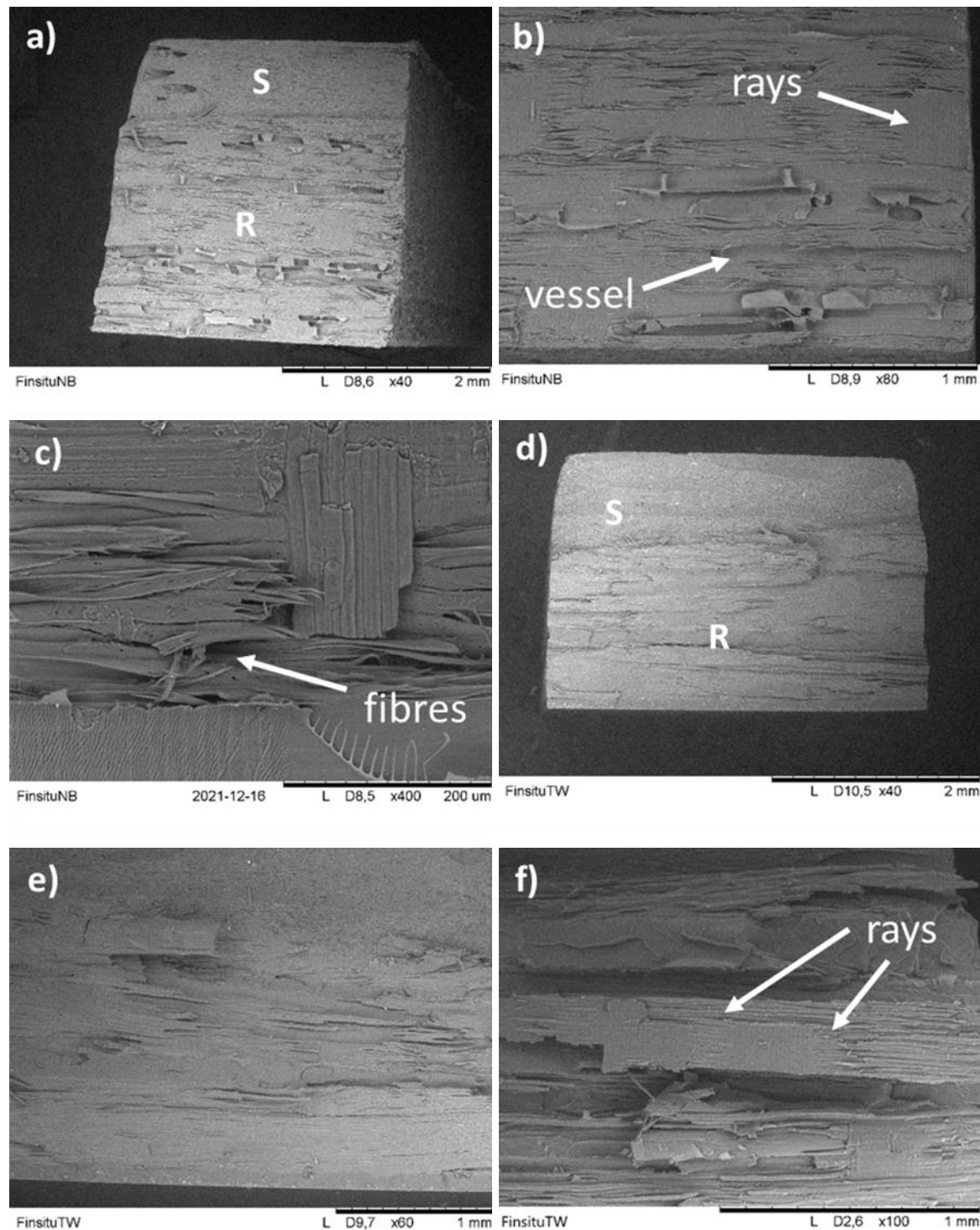
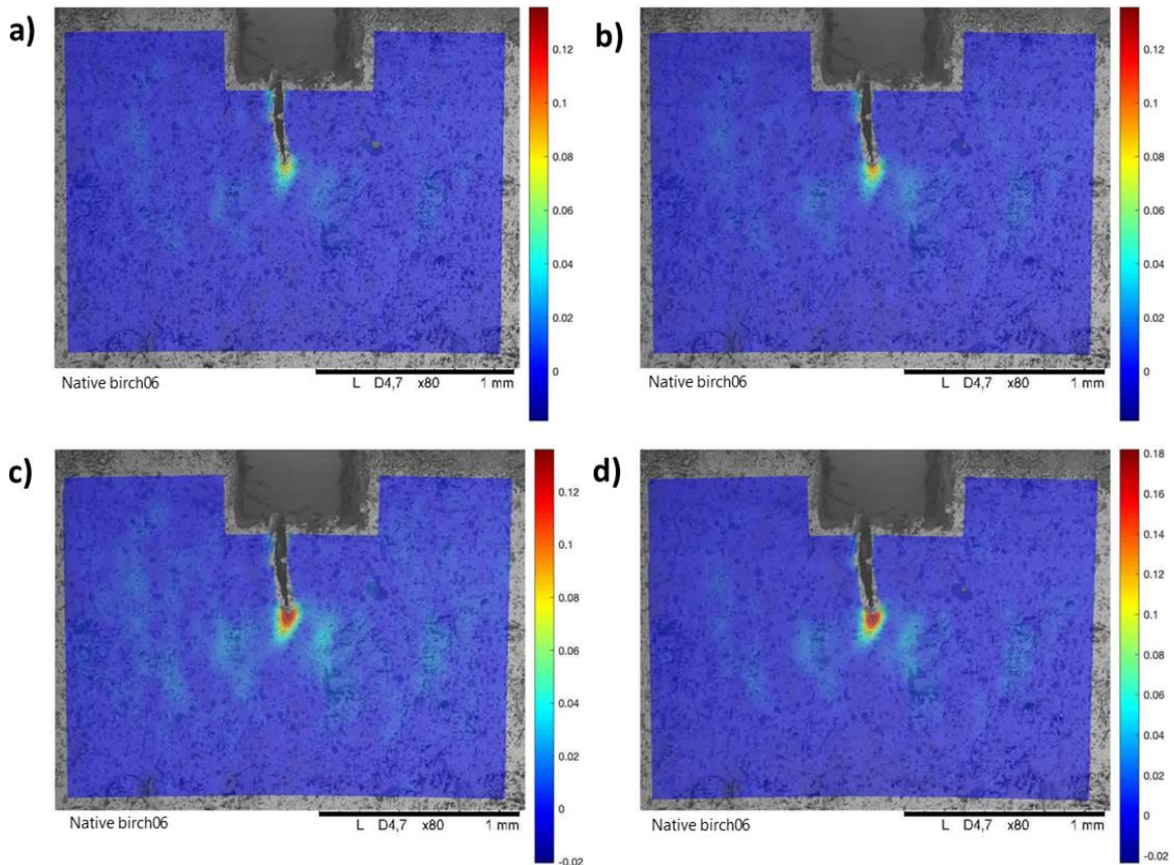


**Figure 5.9.** Fracture surfaces of sample evaluated by in situ single-edge-notched four-point bending test. (a)-(c) native wood and (d)-(f) transparent wood.

### 5.3 DIC analysis

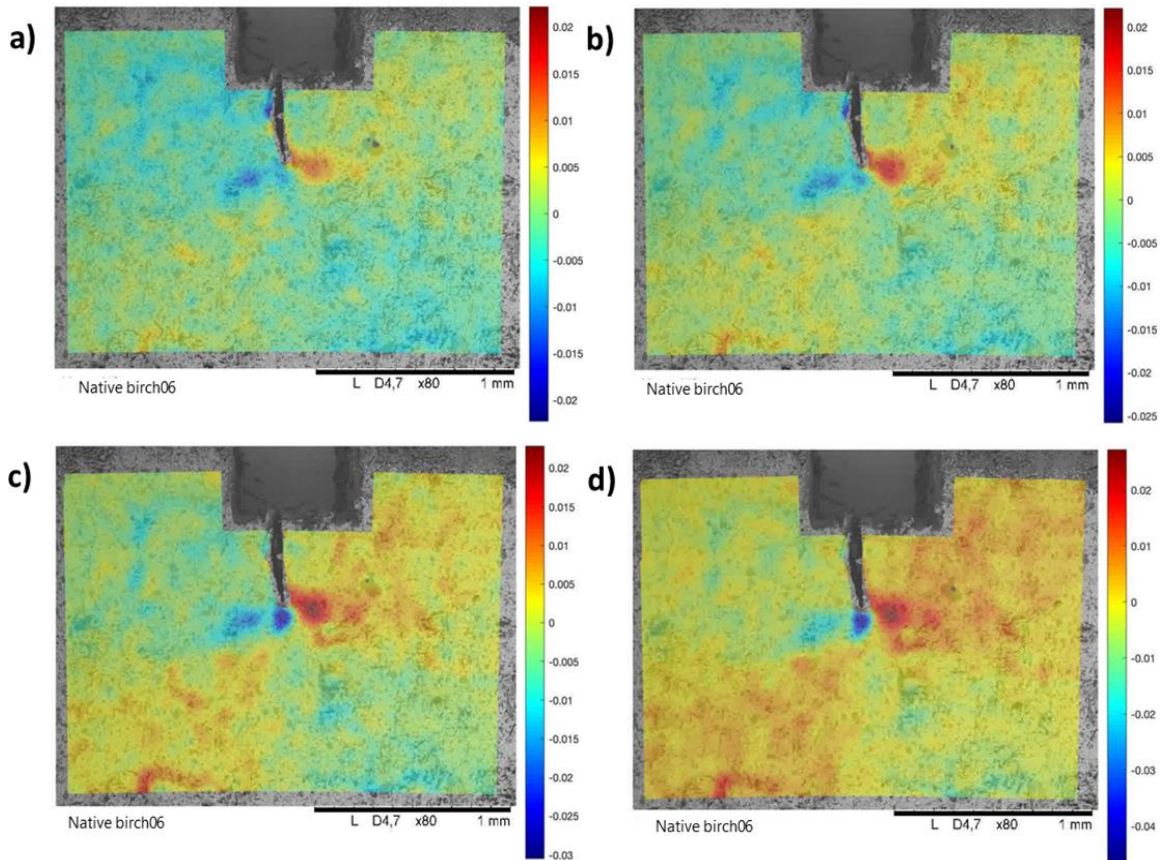
The DIC analysis focused on the strain fields  $\varepsilon_T$  and  $\varepsilon_{TR}$ . The shear strain was studied to understand if the samples underwent delamination during the test. Below, only images from a single specimen for each material are shown as representative of that material.

The strain field  $\varepsilon_T$  of a native birch sample resulting from the DIC analysis is shown in Figure 5.10, where different stages of the test are displayed. The images were acquired at 1.7 N, 1.9 N, 2 N, and 2.1 N, respectively. The increasing strain around the crack tip suggests the presence of the fracture process zone. The development of a FPZ in wood is mainly due to energy-dissipation mechanisms such as microcracks and fiber bridging [77,78]. They contribute to increase the toughness of the material [48]. However, the extension of the fracture process zone is very limited, suggesting the aforementioned energy-dissipation mechanisms are confined in a narrow region around the crack tip. Similar extensions of the FPZ were noticed for all the native wood specimens tested. This seems to support the general practice of using linear elastic fracture mechanics in the studying of the samples at the microscopic level [3].



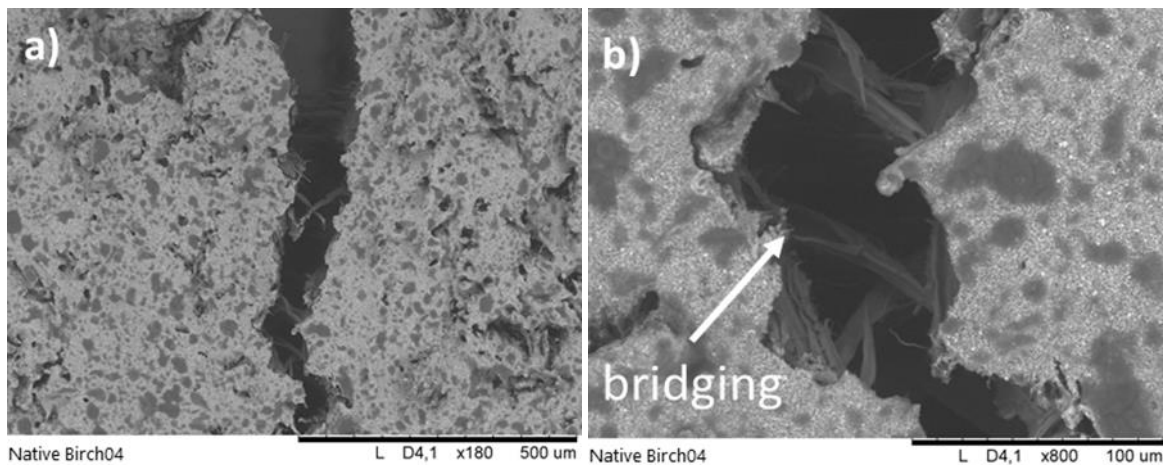
**Figure 5.10.** Strain field  $\varepsilon_T$  before crack propagation in native birch.

Now considering the strain field  $\varepsilon_{TR}$  in the same stages of the test, no delamination seems to occur (see Figure 5.11). However, a dark red area can be seen close to the crack tip, suggesting a region of stress concentration. It probably depended on some defects of the material that did not allow an ideal stress distribution. From Fig. 5.10 (d) and Fig. 5.11 (d), it can be noticed just before the crack onset, the strain  $\varepsilon_T$  is roughly nine times larger than the shear strain, however, this was expected as already discussed in section 4.2.6.



**Figure 5.11.** Strain field  $\varepsilon_{\text{TR}}$  before crack propagation in native birch.

The in situ observations on the samples provide further evidence on the presence of fiber bridging in native wood along TR system (see Figure 5.12).



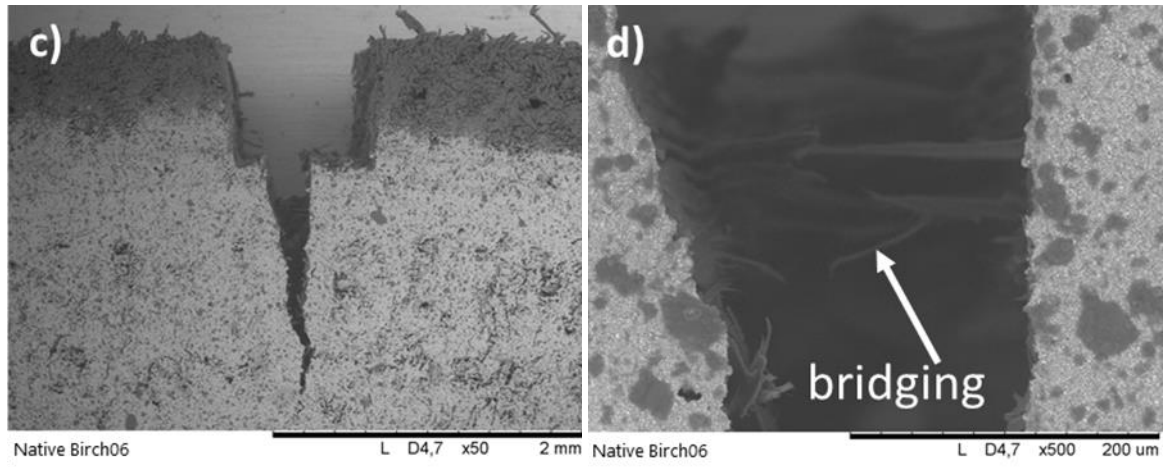


**Figure 5.12.** Fiber bridging in native birch.

The DIC analysis was carried out for transparent wood, too. Figure 5.13 shows the strain field  $\epsilon_T$  of one of the specimens. In this case, the images shown were acquired at 3.2 N, 3.4 N, 3.7 N, and 4 N, respectively. Again, the development of the FPZ was followed before the crack starts propagating. In this material, the fracture process zone extends relatively far away from the notch (see Fig. 5.13 (d)), when compared to native wood.

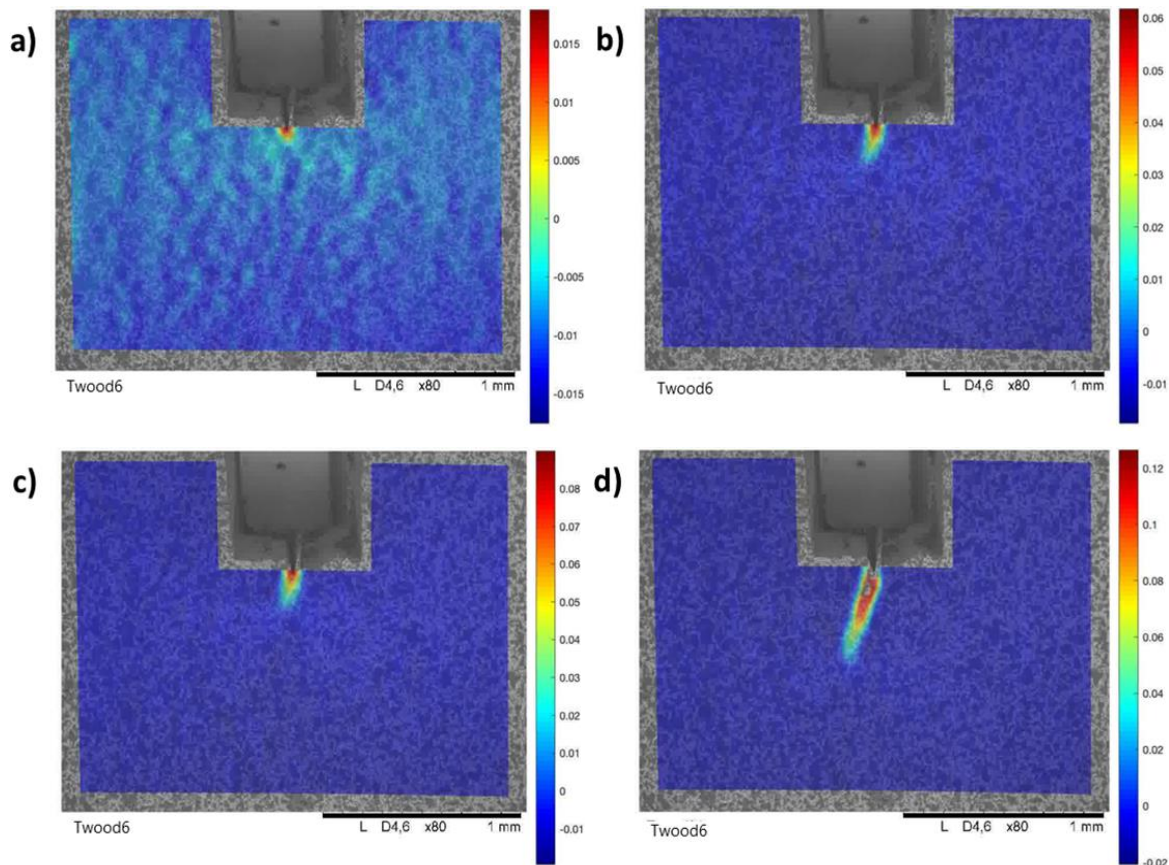


**Figure 5.13.** Strain field  $\epsilon_T$  before crack propagation in transparent wood.

Analysing the strain field  $\varepsilon_{TR}$  shown in Figure 5.14, no shear strains due to delamination can be seen. This result supports the in situ observations done during the previous tests. It also seems to confirm that the bond between the different plies is good enough as the crack does not tend to propagate at the interface between them.

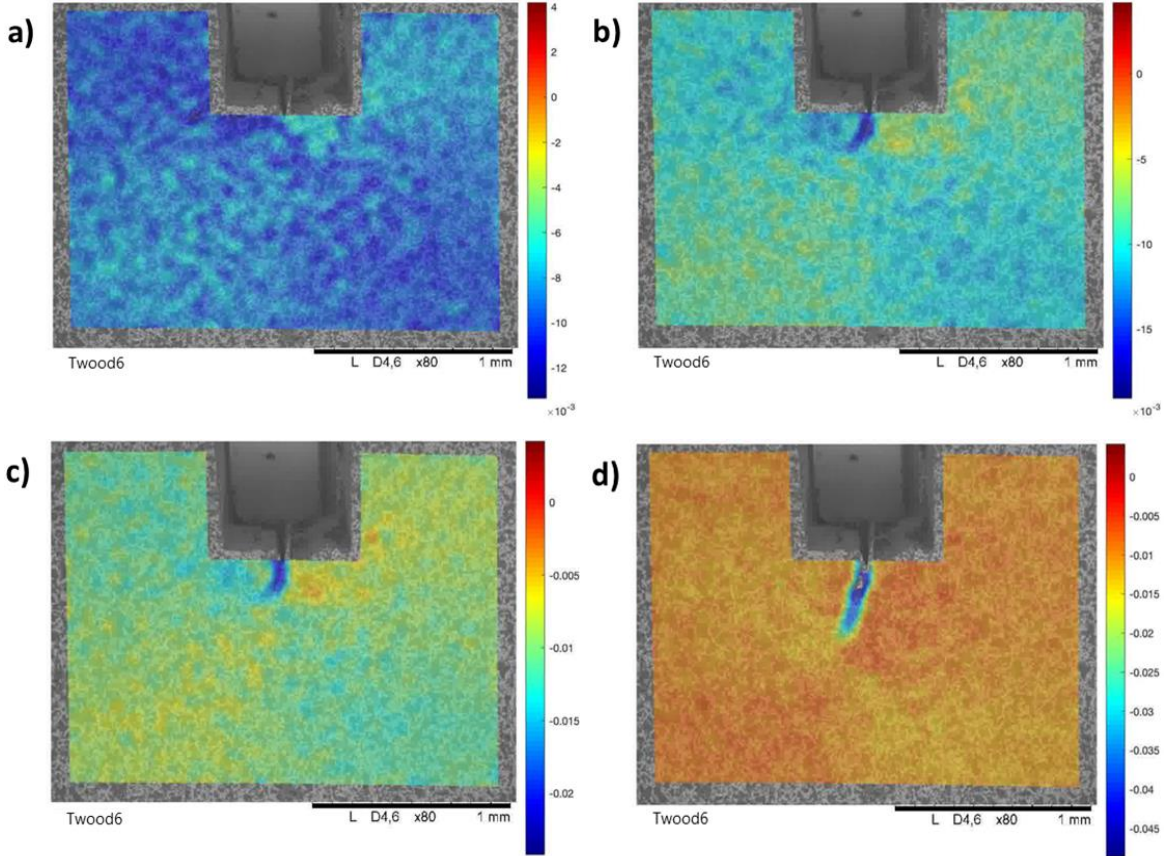


**Figure 5.14.** Strain field  $\varepsilon_{TR}$  before crack propagation in transparent wood.

From the in situ observations shown in Figure 5.15, it can be noticed that the fiber bridging is not as extensive as in native wood. This might suggest that microcracks are more important in the development of the fracture process zone in transparent wood. Indeed, although in this case microcracks cannot be seen due to the speckle, some microcracks departing from the main crack were observed for TW in the previous tests (see Figs. 5.8 (c)-(e)) but not for native birch.

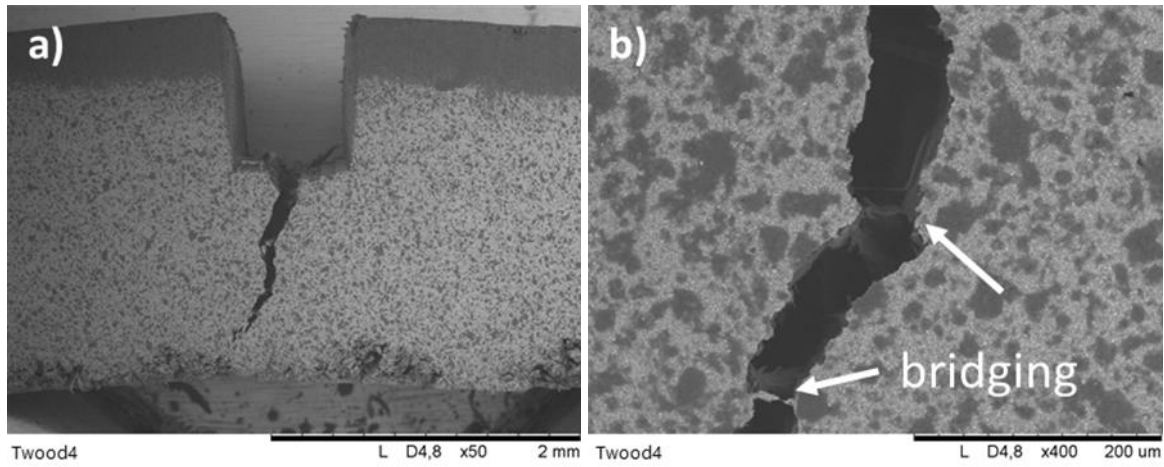
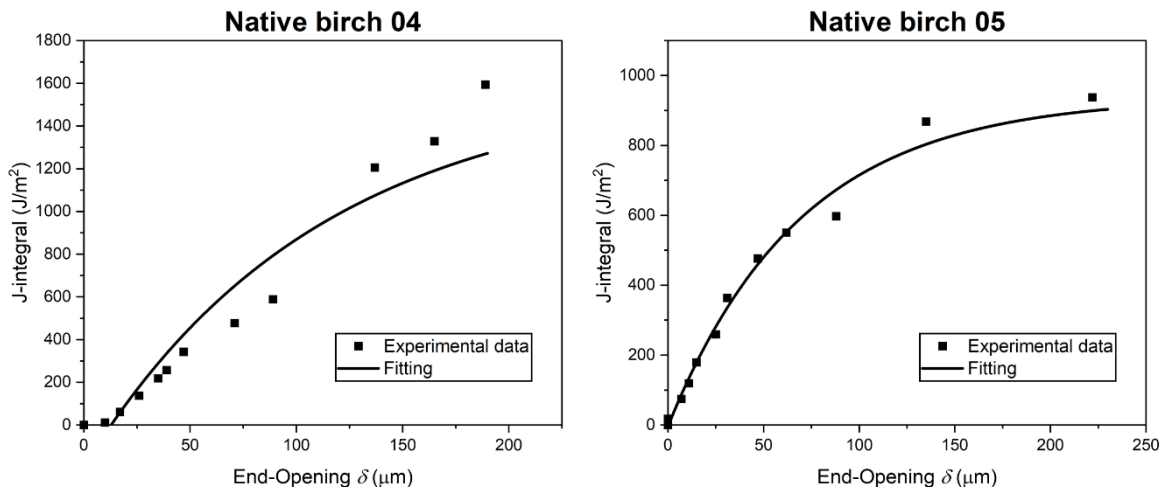


**Figure 5.15.** fiber bridging in transparent wood.

#### 5.4 Cohesive law

Since the in situ observations and the DIC analysis demonstrated the possible presence of the fracture process zone, the images obtained were studied trying to see if the cohesive law could be applied to the materials tested.

The curves that represent the fitting of the J-integral as function of end opening  $\delta$  for native wood are shown in Figure 5.16. There are several studies on the application of the cohesive model along the TL and RL systems for wood and wood composites [48,79–81] but, to the best of the author's knowledge, none has yet tried to apply the cohesive law to the TR system.



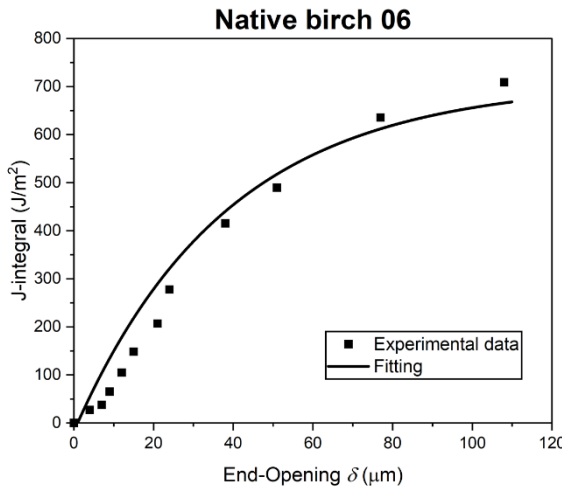


**Figure 5.16.** Curve Fitting of J- $\delta$  data for native birch.

As mentioned before, the experimental data were fitted to obtain a function that could express the relationship between the J-integral and the end-opening. For all specimens tested, the general equation found was:

$$J = a(1 - b \exp(-c\delta)) \quad (12)$$

The equation was chosen assuming the J-integral in the TR system follows the same exponential trend as the other fracture systems of wood [82]. The coefficient  $a$  corresponds to  $J_{ss}$  which is the value of the fracture resistance when the steady-state crack growth is reached [42,47]. In this case, the stress  $\sigma$  tends to zero. The coefficients  $b$  and  $c$  are obtained from the fitting.

The values of all coefficients are reported in Table 5.2, together with the  $R^2$  of the fitting.

**Table 5.2.** Fitting coefficients for native wood and relative R-Squared.

Sample	a	b	c	$R^2$
Native birch 04	1593.5	1.123	9.042	0.9184
Native birch 05	937.5	1.004	14.42	0.9877
Native birch 06	708.8	1.089	24.32	0.9798

Then, the functions were differentiated to obtain the cohesive law according to equation 2. The resulting curves are displayed in Figure 5.17. They seem to be in good agreement with each other as the maximum stress is, for all curves, almost the same. However, the main object here was to see if the fracture behaviour of the material may fulfil the criteria of the cohesive law and from the data seems so. Further investigations are required to get a more complete set of information on the curve and the full characterization of the cohesive law along the TR system.

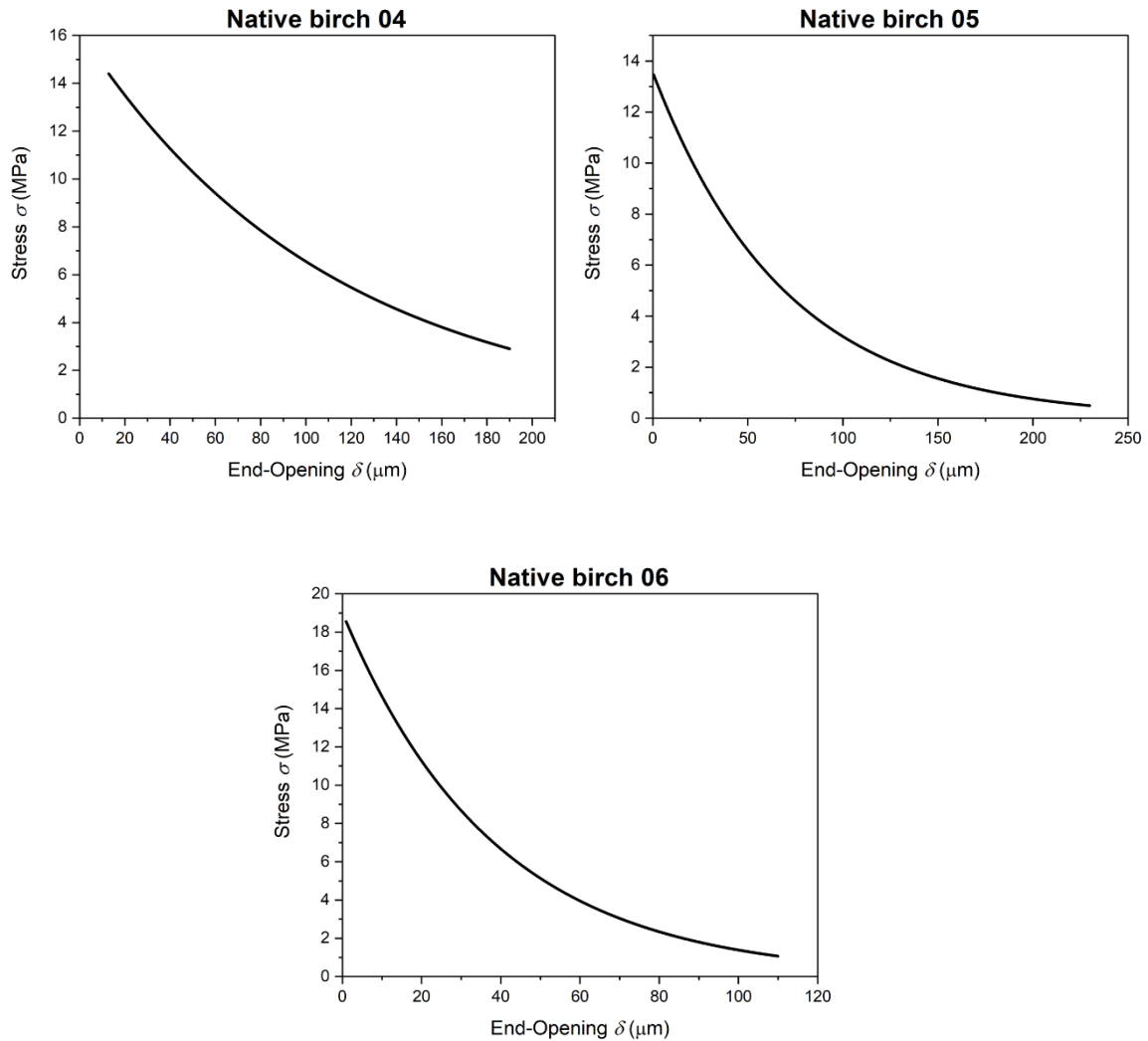


**Figure 5.17.** Cohesive law for native birch.

As done for native wood, also the J- $\delta$  data for transparent wood were fitted (see Figure 5.18). The fitting demonstrated that the same general equation (equation 12) used for native birch was also appropriate for transparent wood. The coefficients found for delignified birch/PMMA TW are displayed in Table 5.3.

**Table 5.3.** Fitting coefficients for transparent wood and relative R-Squared.

Sample	a	b	c	R <sup>2</sup>
TW 04	1790.5	1.004	65.12	0.9708
TW 05	479.3	0.9938	67.83	0.9851
TW 06	553	1.007	85.59	0.9818

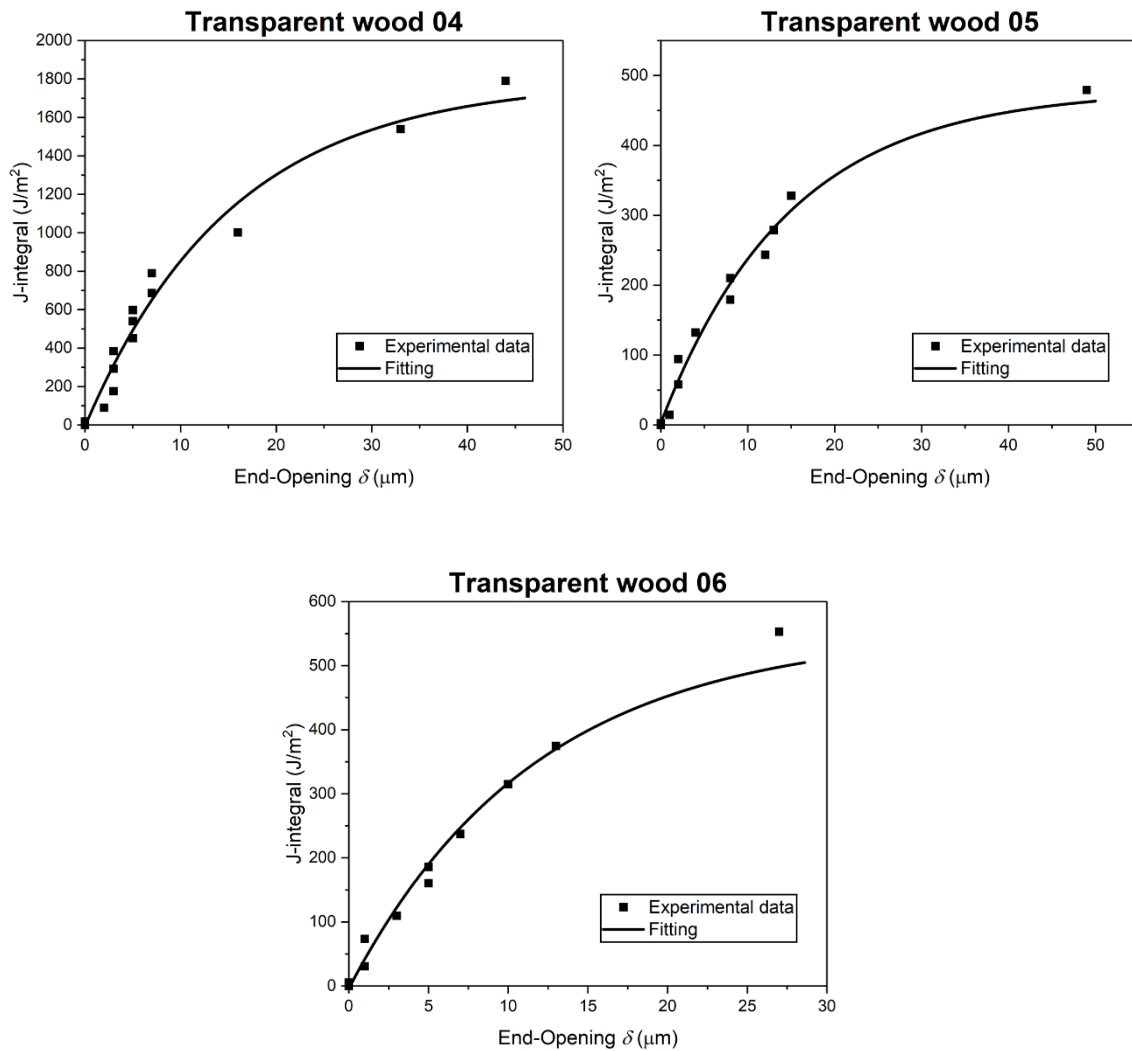


**Figure 5.18.** Curve Fitting of J- $\delta$  data for transparent wood.

Similar to native wood, the resulting J-integral vs  $\delta$  curves were derived to obtain the cohesive law.

Figure 5.19 displays the results of the derivation for transparent wood along the TR system. In this case, considerations cannot be done about the maximum stress as the first sample showed a  $\sigma_{\max}$  about three times larger compared to the other specimens. The reason for this can be different: since the complexity of the material and the small size of the samples, local defects can play an important role. However, similarly to what has been done on wood, this was a preliminary study, which aim was to understand if the application of the cohesive law was feasible for this material and along a specific fracture system (i.e., TR). From the curves obtained and from the results of the DIC, it is reasonable to assume that the cohesive law can be used in modelling the fracture behaviour of the material. As for native wood, additional analyses are needed for a full characterization of the cohesive law for this transparent wood biocomposite.

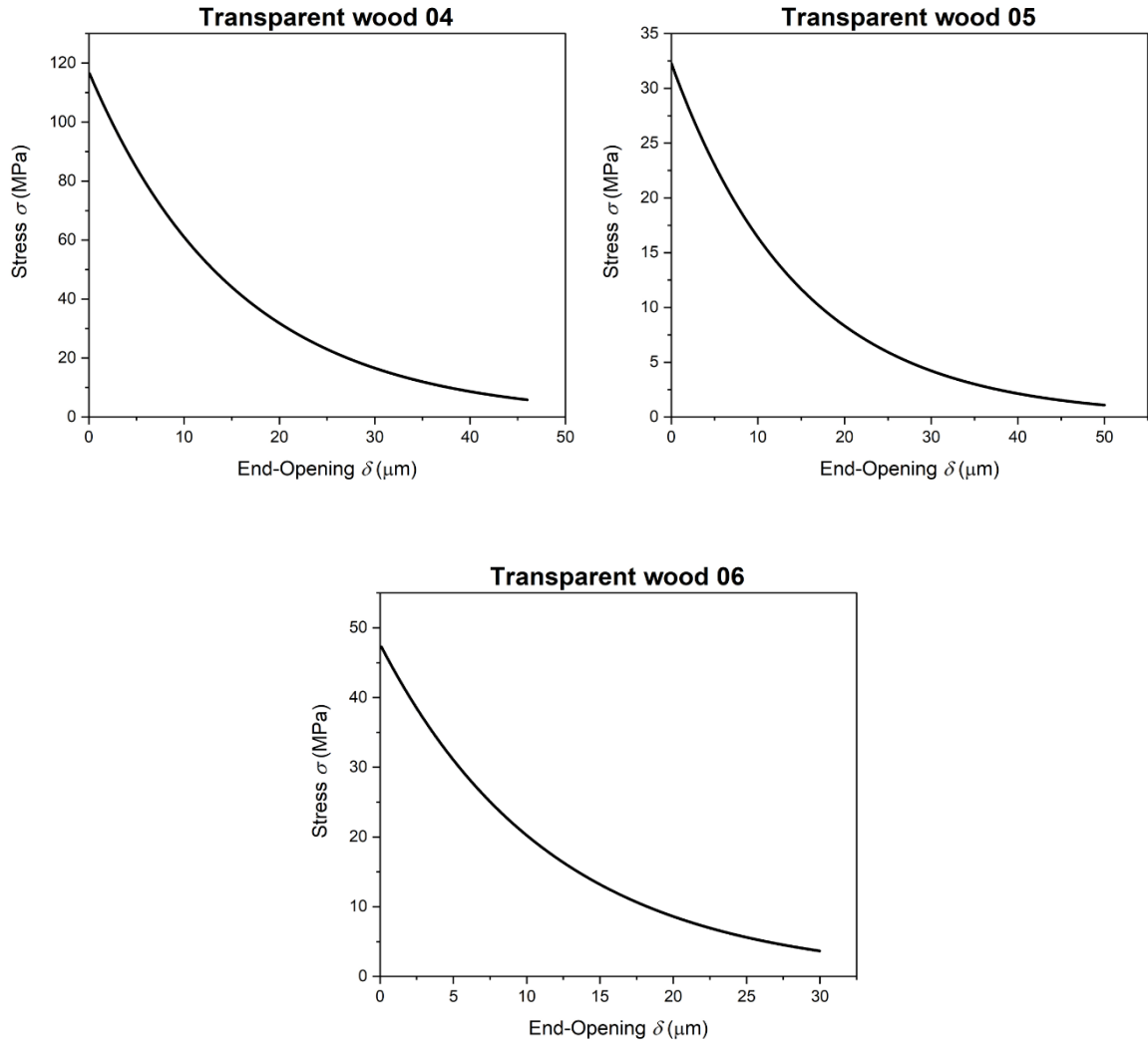
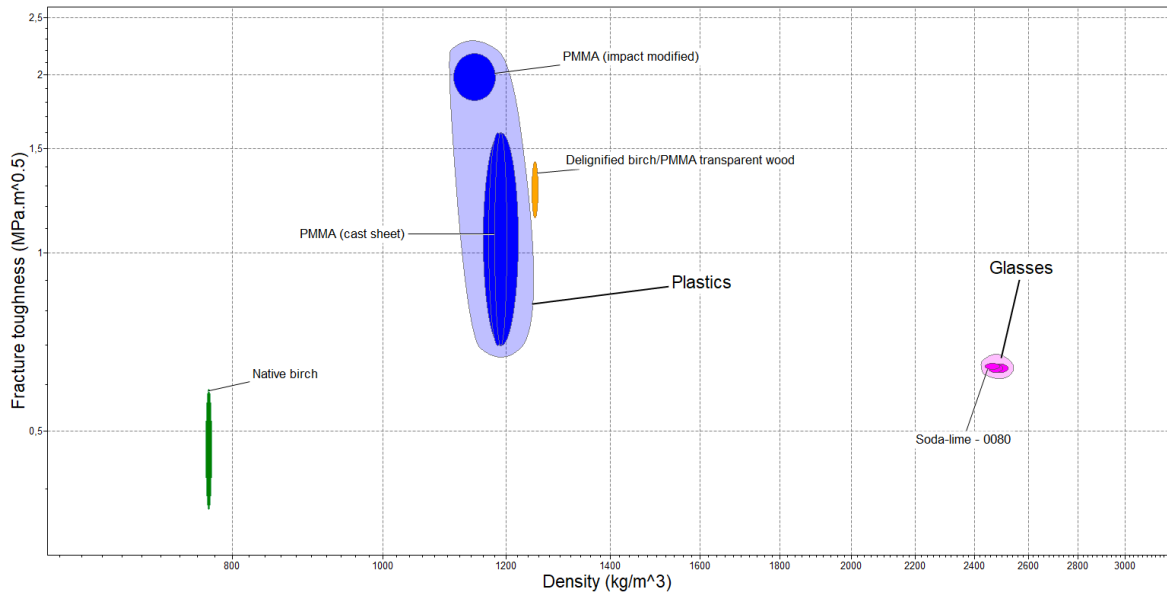


**Figure 5.19.** Cohesive law for native birch

### 5.5 Demonstration of use of the measured mechanical properties for material design

The mechanical characterization described in sections 5.1 and 5.2 provided enough data for a preliminary material selection based on Ashby's material property charts. Indeed, the abundance of materials that an engineer can use nowadays makes material selection a crucial aspect of the design of a product [74]. Based on this, three plots were elaborated.

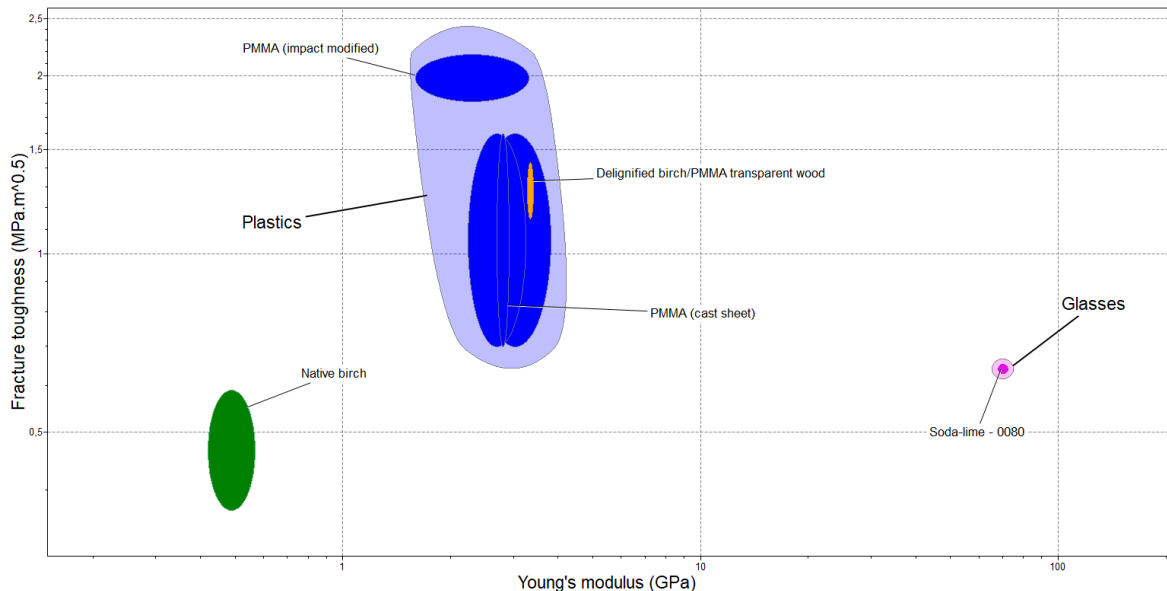
In the first material property chart, shown in Figure 5.20, the fracture toughness is plotted against the density. In this case, the best materials are located in the top left corner as they exhibit the desirable combination of properties: high  $K_{Ic}$  and low density.



**Figure 5.20.** Material property chart  $K_{Ic}$  vs  $\rho$ .

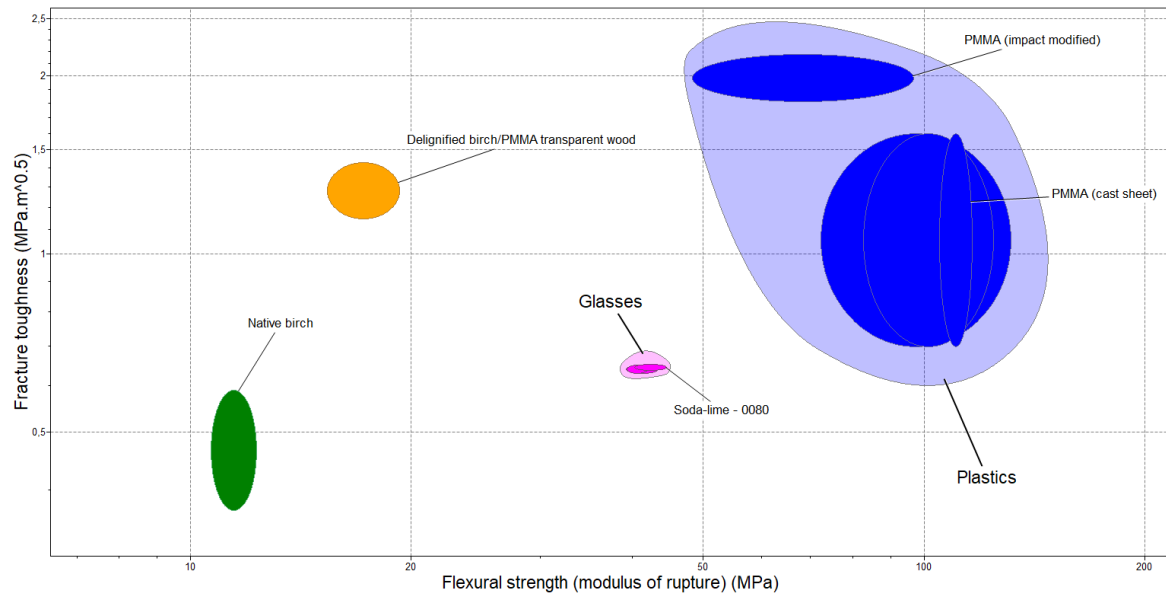
When these parameters are taken into account, transparent wood performs way better than the soda-lime glass family (which is one of its competitors in the building sector). The combination of  $K_{Ic}$  and  $\rho$  of TW is comparable to that of common PMMA while it is slightly worse than that of PMMA designed to have superior toughness respect to the common polymer. This seems to confirm the great potential of this transparent wood biocomposite, especially because the fracture toughness was measured along one of the weak systems.

Figure 5.21 displays the fracture toughness vs the Young's modulus. Again, the properties of TW are similar to those of PMMA. On the other hand, its elastic modulus is much lower than that of glass, but this was expected as  $E$  was measured normal to the fibers.



**Figure 5.21.** Material property chart  $K_{Ic}$  vs  $E$ .

Finally, the fracture toughness was plotted against the flexural strength (see Figure 5.22). In this case, TW performs worse than both PMMA and glass. Like for the elastic modulus, the flexural strength was measured along the transverse direction. Therefore, this outcome was expected.



**Figure 5.22.** Material property chart  $K_{Ic}$  vs  $\sigma$ .



## **6. Conclusion and future works**

### *6.1 Résumé*

The main object of this work of thesis was to broaden the current knowledge about the mechanical behaviour of transparent wood biocomposites. The experiments carried out gave fundamental insights into the mechanical properties and fracture mechanics of this promising biobased composite.

It was demonstrated that the delignified birch/PMMA transparent wood studied possessed a higher transverse elastic modulus of native birch and PMMA. Moreover, its transverse flexural strength increased compared to native wood, although less noticeably than the stiffness. The fracture toughness along the TR system was evaluated and the fracture mechanisms were studied and discussed. As result, the fracture toughness of transparent wood was twice that of glass. In addition, it was observed that the fracture in TW propagates along the ray cells, similarly to what happens in native wood, and it is based on cell wall breaking and cell wall peeling. The DIC analysis confirmed the presence of the fracture process zone ahead of the crack tip for both transparent wood and native birch in TR system and excluded that delamination had occurred in TW during the fracture. The previous observations led to an assessment of the feasibility of applying the cohesive law model to TW and NW. Not only has it been shown that it can be used but it has also been possible to obtain a general equation describing the cohesive law for both materials. Finally, it was demonstrated that, with the properties measured, a preliminary material selection for design purposes can be made.

In conclusion, the object of the thesis was achieved. As a further result, it was also possible to increase the knowledge about the mechanical properties and fracture mechanisms of native birch. Indeed, it was demonstrated the presence of fiber bridging in the fracture along the TR system, as well as the possibility of using the cohesive law to describe the TR fracture.

### *6.2 Future works*

This work of thesis has contributed to expanding the current understanding of the mechanical behaviour of transparent wood biocomposites. It provides results that can be used to build the first simulations on the mechanical response of transparent wood. However, much remains to be done before a complete mechanical characterization can be achieved. For instance, the remaining fracture systems still need to be studied. Furthermore, the effect that tailoring the functional properties has on mechanical performance is another important research field where little work has been done. In this thesis, the viscoelastic effects of transparent wood were not taken into account, however, they certainly affect the mechanical response and therefore need to be investigated. The results obtained by applying the cohesive zone model should be further studied by means of other experimental techniques or simulations. Finally, functional properties, optical properties, and production costs should be implemented for a proper material selection.

## Acknowledgements

While I am writing this section, I have finally realised that I am almost there, as only a few steps separate me from the end of this amazing journey. Then, as my sister likes reminding me, the “real challenges” will begin.

I would like to thank Prof. Lars Berglund, for giving me the opportunity to carry out my master’s thesis at the Biocomposite division on such a new and interesting topic as transparent wood biocomposites.

Moreover, I would like to express my gratitude to my supervisor at KTH, Dr. Marcus Vinícius Tavares da Costa, who guided me through the entire thesis, providing me inspiration and help. Your great knowledge of *in situ* observations and mechanical modelling helped me in achieving the objects of this thesis. Our discussions on material behaviour have always given me new food for thought.

A big thank you also goes to my supervisor at Politecnico di Torino, Prof. Federico Carosio, who helped me with his experience during the most difficult moments of this project.

Many thanks to all members of Biocomposite group who warmly welcomed me during my time in this division. Thanks Erik Jungstedt, Dr. Hui Chen, and Dr. Bin Chen for helping me.

Last but not least, I thank my family: my parents, Franca and Vito, my sisters Martina and Elena, and my brother-in-law Stefano. All of you have always and unconditionally supported me throughout my journey. Spero di avervi reso orgogliosi.

## References

1. Jungstedt E, Montanari C, Östlund S, et al. (2020) Mechanical properties of transparent high strength biocomposites from delignified wood veneer. *Composites Part A: Applied Science and Manufacturing* 133.
2. Krala G, Ubowska A, Kowalczyk K (2014) Mechanical and thermal analysis of injection molded poly(methyl methacrylate) modified with 9,10-dihydro-9-oxa-10-phosphaphhenanthrene-10-oxide (DOPO) fire retarder. *Polymer Engineering & Science* 54: 1030–1037.
3. Tukiainen P (2016) Mode I fracture behaviour of Norway spruce and silver birch in the radial-tangential and tangential-radial crack orientations.
4. Lorna JG, Ashby MF (1997) Wood, *Cellular Solids*, Cambridge University Press, 387–428.
5. Ashby MF (2021) Introduction, *Materials and the Environment*, Elsevier, 1–19.
6. Fu Q, Yan M, Jungstedt E, et al. (2018) Transparent plywood as a load-bearing and luminescent biocomposite. *Composites Science and Technology* 164.
7. Montanari C, Ogawa Y, Olsén P, et al. (2021) High performance, fully bio-based, and optically transparent wood ciocomposites. *Advanced Science* 8.
8. Zhu M, Song J, Li T, et al. (2016) Highly anisotropic, highly transparent wood composites. *Advanced Materials* 28.
9. Montanari C, Olsén P, Berglund LA (2021) Sustainable wood nanotechnologies for wood composites processed by in-situ polymerization. *Frontiers in Chemistry* 9.
10. Li Y, Fu Q, Yang X, et al. (2018) Transparent wood for functional and structural applications. *Philosophical Transactions of the Royal Society A: Mathematical, Physical and Engineering Sciences* 376: 20170182.
11. Koivurova M, Vasileva E, Li Y, et al. (2018) Complete spatial coherence characterization of quasi-random laser emission from dye doped transparent wood. *Optics Express* 26: 13474.
12. Li Y, Yu S, Veinot JGC, et al. (2017) Luminescent transparent wood. *Advanced Optical Materials* 5: 1600834.
13. Vasileva E, Li Y, Sychugov I, et al. (2017) Lasing from organic dye molecules embedded in transparent wood. *Advanced Optical Materials* 5: 1700057.
14. Gan W, Gao L, Xiao S, et al. (2017) Transparent magnetic wood composites based on immobilizing Fe<sub>3</sub>O<sub>4</sub> nanoparticles into a delignified wood template. *Journal of Materials Science* 52: 3321–3329.
15. Li Y, Cheng M, Jungstedt E, et al. (2019) Optically transparent wood substrate for perovskite solar cells. *ACS Sustainable Chemistry & Engineering* 7: 6061–6067.
16. Li Y, Fu Q, Rojas R, et al. (2017) Lignin-retaining transparent wood. *ChemSusChem* 10: 3445–3451.

17. Chen Q, Jiang Z, Pei X, et al. (2021) Bio-inspired, epoxy-based lamellar composites with superior fracture toughness by delignified wood scaffold. *Composites Science and Technology* 207: 108739.
18. Antolovich SD, Saxena A, Gerberich WW (2018) Fracture mechanics – An interpretive technical history. *Mechanics Research Communications* 91: 46–86.
19. Thelandersson S, Larsen HJ (2003) Timber Engineering, John Wiley & Sons.
20. Stanzl-Tschegg StefanieE, Tan D-M, Tschegg E (1995) New splitting method for wood fracture characterization. *Wood Science and Technology* 29.
21. Li Y, Fu Q, Yu S, et al. (2016) Optically transparent wood from a nanoporous cellulosic template: combining functional and structural performance. *Biomacromolecules* 17: 1358–1364.
22. Ashby MF, Easterling KE, Harrysson R, et al. (1985) Fracture and toughness of woods. *Proceedings of The Royal Society of London, Series A: Mathematical and Physical Sciences* 398: 261–280.
23. Li Y, Yang X, Fu Q, et al. (2018) Towards centimeter thick transparent wood through interface manipulation. *Journal of Materials Chemistry A* 6: 1094–1101.
24. Fratzl P (2004) Hierarchical structure and mechanical adaptation of biological materials.
25. Fratzl P, Weinkamer R (2007) Nature's hierarchical materials. *Progress in Materials Science* 52: 1263–1334.
26. Chen C, Kuang Y, Zhu S, et al. (2020) Structure–property–function relationships of natural and engineered wood. *Nature Reviews Materials* 5: 642–666.
27. Hofstetter K, Gamstedt EK (2009) Hierarchical modelling of microstructural effects on mechanical properties of wood. A review COST Action E35 2004–2008: Wood machining – micromechanics and fracture. *Holzforschung* 63.
28. Wågberg Lars (2021) 1. Hierarkiska strukturer.
29. Parham RA, Gray RL (1984) Formation and Structure of Wood.
30. The Ljungberg textbook. Wood chemistry and wood biotechnology, KF 2010, 2008 (2008) Stockholm, Fibre and Polymer Technology, KTH.
31. Dinwoodie JM (2000) Timber: its nature and behaviour, London, E. & F. N. Spon.
32. Forest Service U, Products Laboratory F (2010) Wood Handbook, Wood as an Engineering Material.
33. Pan S, Kudo M (2012) Recognition of wood porosity based on direction insensitive feature sets.
34. Tsoumis G. (1968) Wood as raw material, Elsevier.
35. S F de Moura MF, Dourado N Wood fracture characterisation.
36. Perala DA, Alm AA (1990) Reproductive ecology of birch: A review. *Forest Ecology and Management* 32: 1–38.
37. Lachowicz H, Bieniasz A, Wojtan R (2019) Variability in the basic density of silver birch wood in Poland. *Silva Fennica* 53.

38. Luostarinen K, Verkasalo E (2000) Silva Fennica Monographs 1 · 2000 Birch as sawn timber and in mechanical further processing in Finland. A literature study 2.
39. Frühmann K, Burgert I, Stanzl-Tschegg SE, et al. (2003) Mode I fracture behaviour on the growth ring scale and cellular level of spruce (*Picea abies* [L.] Karst.) and beech (*Fagus sylvatica* L.) loaded in the TR crack propagation system. *Holzforschung* 57: 653–660.
40. Cameron A (1996) Managing birch woodlands for the production of quality timber. *Forestry* 69: 357–371.
41. Anderson TL (2005) Fracture Mechanics: fundamentals and applications.
42. Sørensen BF. (2010) Cohesive laws for assessment of materials failure: Theory, experimental methods and application.
43. Cotterell B (2002) The past, present, and future of fracture mechanics. *Engineering Fracture Mechanics* 69: 533–553.
44. Thuvander F, Sjödahl M, Berglund LA (2000) Measurements of crack tip strain field in wood at the scale of growth rings. *Journal of Materials Science*.
45. Rice JR, Paris PC, Merkle JG (1973) Some further results of J-Integral analysis and estimates, *Progress in Flaw Growth and Fracture Toughness Testing*, 100 Barr Harbor Drive, PO Box C700, West Conshohocken, PA 19428-2959, ASTM International, 231–245.
46. Sørensen BF, Jacobsen TK (2003) Determination of cohesive laws by the J integral approach. *Engineering Fracture Mechanics* 70: 1841–1858.
47. Goutianos S, Sørensen BF (2016) The application of J integral to measure cohesive laws under large-scale yielding. *Engineering Fracture Mechanics* 155: 145–165.
48. Ostapska K, Malo KA (2021) Calibration of a combined XFEM and mode I cohesive zone model based on DIC measurements of cracks in structural scale wood composites. *Composites Science and Technology* 201: 108503.
49. Fink S (1992) Transparent wood-a new approach in the functional study of wood structure.
50. Karl'a V (2019) Update on research on transparent wood. *IOP Conference Series: Materials Science and Engineering* 566: 012015.
51. Xia Q, Chen C, Li T, et al. (2021) Solar-assisted fabrication of large-scale, patternable transparent wood. *Science Advances* 7.
52. Qin J, Li X, Shao Y, et al. (2018) Optimization of delignification process for efficient preparation of transparent wood with high strength and high transmittance. *Vacuum* 158: 158–165.
53. Wang X, Zhan T, Liu Y, et al. (2018) Large-size transparent wood for energy-saving building applications. *ChemSusChem* 11: 4086–4093.
54. Koltzenburg S, Maskos M, Nuyken O (2017) Polymer Chemistry, Berlin, Heidelberg, Springer Berlin Heidelberg.
55. Ali U, Karim KJBtA, Buang NA (2015) A review of the properties and applications of Poly (methyl methacrylate) (PMMA). *Polymer Reviews* 55.

56. Chanda M (2013) Introduction to Polymer Science and Chemistry A Problem-Solving Approach, CRC Press.
57. Odian GG (2004) Principles of polymerization.
58. Odian GG (2004) Principles of polymerization, Hoboken, N.J., Wiley-Interscience.
59. Vernon-Parry KD (2000) Scanning electron microscopy: an introduction. *III-Vs Review* 13: 40–44.
60. Goldstein JI, Newbury DE, Michael JR, et al. (2018) Scanning electron microscopy and x-ray microanalysis, New York, NY, Springer New York.
61. de Souza JA, Goutianos S, Skovgaard M, et al. (2011) Fracture resistance curves and toughening mechanisms in polymer based dental composites. *Journal of the Mechanical Behavior of Biomedical Materials* 4: 558–571.
62. SHI Q, Roux S, Latourte F, et al. (2018) On the use of SEM correlative tools for in situ mechanical tests. *Ultramicroscopy* 184: 71–87.
63. Hitachi high-technologies announces shipments of tabletop microscope TM-1000 surpass 1,000 units (2009).
64. Brancherieu L, Bailleres H, Guitard D (2002) Comparison between modulus of elasticity values calculated using 3 and 4 point bending tests on wooden samples. *Wood Science and Technology* 36: 367–383.
65. Timber structures-Glued laminated timber-Test methods for determination of physical and mechanical properties (2017).
66. Gere JM (2001) Mechanics of materials, Pacific Grove, Calif., Brooks/Cole.
67. Hein PRG, Brancherieu L (2018) Comparison between three-point and four-point flexural tests to determine wood strength of Eucalyptus specimens. *Maderas Ciencia y tecnología* 0–0.
68. Rudolf C, Boesl B, Agarwal A (2016) In situ mechanical testing techniques for real-time materials deformation characterization. *JOM* 68: 136–142.
69. Standard test method for determination of reference temperature,  $T_o$ , for ferritic steels in the transition range 1 (2019).
70. Badini C. (2013) Materiali compositi per l'ingegneria., Celid.
71. Pan B, Qian K, Xie H, et al. (2009) Two-dimensional digital image correlation for in-plane displacement and strain measurement: a review. *Measurement Science and Technology* 20: 062001.
72. Pan B (2018) Digital image correlation for surface deformation measurement: historical developments, recent advances and future goals. *Measurement Science and Technology* 29: 082001.
73. McCormick N, Lord J (2010) Digital Image Correlation. *Materials Today* 13: 52–54.
74. Ashby MF (2019) Materials: engineering, science, processing and design.
75. Fredriksson C, Vakhitova T (2020) Educational software for a sustainable future, *2020 IEEE Frontiers in Education Conference (FIE)*, IEEE, 1–3.

76. Davenport JCW, Smith DJ (1993) A study of superimposed fracture modes I, II and III on PMMA. *Fatigue & Fracture of Engineering Materials and Structures* 16: 1125–1133.
77. Romanowicz M (2022) Numerical assessment of the apparent fracture process zone length in wood under mode I condition using cohesive elements. *Theoretical and Applied Fracture Mechanics* 118: 103229.
78. Yu Y, Xin R, Zeng W, et al. (2021) Fracture resistance curves of wood in the longitudinal direction using digital image correlation technique. *Theoretical and Applied Fracture Mechanics* 114: 102997.
79. Coureau J-L, Morel S, Dourado N (2013) Cohesive zone model and quasibrittle failure of wood: A new light on the adapted specimen geometries for fracture tests. *Engineering Fracture Mechanics* 109: 328–340.
80. Yu Y, Xin R, Zeng W, et al. (2021) Fracture resistance curves of wood in the longitudinal direction using digital image correlation technique. *Theoretical and Applied Fracture Mechanics* 114: 102997.
81. Mirzaei B, Sinha A, Nairn JA (2016) Measuring and modeling fiber bridging: Application to wood and wood composites exposed to moisture cycling. *Composites Science and Technology* 128: 65–74.
82. Vasic S, Smith I (2002) Bridging crack model for fracture of spruce. *Engineering Fracture Mechanics* 69: 745–760.